TESIS DOCTORAL

2016

OPTIMIZATION OF STOCHASTIC GLOBAL VARIANCE REDUCTION TECHNIQUES FOR MONTE CARLO NEUTRON TRANSPORT WITH APPLICATIONS TO THE ITER GEOMETRY

LUCÍA PÉREZ FERNÁNDEZ

LICENCIADA EN CIENCIAS FÍSICAS

PROGRAMA DE DOCTORADO EN TECNOLOGÍAS INDUSTRIALES

Director: Dr. Patrick Sauvan

Co-director: Dr. Francisco Ogando Serrano

TESIS DOCTORAL

TÍTULO

Optimization of stochastic global variance reduction techniques for Monte Carlo neutron transport with applications to the ITER geometry

Autora

Lucía Pérez Fernández

Licenciada en Ciencias Físicas

Doctorado en Tecnologías Industriales

DEPARTAMENTO DE INGENIERÍA ENERGÉTICA

E.T.S. INGENIERIOS INDUSTRIALES

UNIVERSIDAD NACIONAL DE EDUCACIÓN A DISTANCIA

Director: Dr. Patrick Sauvan

Co-director: Dr. Francisco Ogando Serrano

2016

ACKNOWLEDGEMENTS

I would like to thank in the first place everyone at the TEC3FIR research group that has worked with me. A special shout out to my supervisors Patrick and Paco, and to Javier, our "spiritual leader" at TEC3FIR, for their support, patience, and understanding. I would also like to thank everyone at UNED, for making me feel at home during these four years.

If I were to name each and every person for which I am grateful, I would probably need several pages. So to my family and friends thank you for being a part of my life, you are what make life worth living.

Lastly, I would like to mention that this work has been performed mostly under support of Grant FPI UNED 2011. It has been also partially supported, as part of the TECF3IR contributions, by the Spanish MINECO (Ministerio de Economía y Competitividad) under Programa Estatal I+D+I-Retos, Proyecto ENE2015-70733-R; and the Programa de Actividades I+D de la Comunidad de Madrid under TECHNOFUSIÓN-CM (S2009/ENE-1679) and TECHNOFUSION(II)-CM, (S2013/MAE-2745) Projects for the development of the "Area of Computational Simulation".

TABLE OF CONTENTS

LIST OF TABLES

LIST OF FIGURES

ABBREVIATIONS AND ACRONYMS

AWIC	Analog With Implicit Capture
CADIS	Consistent Adjoint Driven Importance Sampling
CBRT_F	Cubic Root over Flux based weight map
CCFE	Culham Centre for Fusion Energy
D	Deuterium
DEMO	DEMOnstration reactor
D1S	Direct-One-Step
FOM	Figure of Merit
FW-CADIS	Forward Weighted CADIS
GVR	Global Variance Reduction
HD_F	Half Density reduction of the materials over Flux based weight maps
HD_Re	Half Density reduction of the materials over Relative error based weight maps
IC	Inertial Confinement
ITER	International Thermonuclear Experimental Reactor
JET	Joint European Torus
MCNP	Monte Carlo N-Particle
R2S	Rigorous-Two-Step
SDR	Shutdown Dose Rate
SQRT_F	Square Root over Flux based weight map
T	Tritium
TBM	Test Blanket Modules
TBS	Test Blanket System
vanWijk_F	Van Wijk's Flux based weight maps
vanWijk_Re	Van Wijk's Relative error based weight maps
WW	Weight Windows
WWG	Weight Windows Generator

RESUMEN

En el ámbito del diseño de reactores nucleares de fusión, los estudios de neutrónica tienen una destacada importancia. Los neutrones liberados por las reacciones de fusión que tienen lugar en este tipo de reactores son altamente energéticos, y dicha energía será posteriormente aprovechada para generar energía eléctrica en futuras centrales eléctricas de fusión. Sin embargo, los efectos perniciosos causados por estos neutrones, como la capacidad de activar los materiales o su peligrosidad como radiación ionizante, requiere una adecuada caracterización de la distribución de los neutrones dentro del reactor.

Para poder llevar a cabo una correcta evaluación de los flujos neutrónicos en en todo el reactor, es necesario transportar los neutrones por toda su geometría; considerando todas las interacciones de éstos con la materia a lo largo de su trayectoria. Los códigos de transporte basados en el método de Monte Carlo son ampliamente utilizados en la industria nuclear para este fin. No obstante, su aplicabilidad se ve limitada por las capacidades computacionales actuales.

Con el fin de optimizar el transporte neutrónico existen varias técnicas (implementadas en los propios códigos de Monte Carlo) que reducen la varianza en el muestreo de las partículas, reduciendo a su vez el esfuerzo computacional. A pesar de todo, a la hora de caracterizar un sistema en todos los puntos del espacio, estas técnicas resultan insuficientes debido a la naturaleza local de las mismas. Así, en geometrías de grandes dimensiones en las que es necesario caracterizar a lo largo de todo el espacio ciertas funciones respuesta (como por ejemplo la dosis o el calor residual), los códigos de transporte basados en Monte Carlo requieren un gran esfuerzo computacional. Este

problema se ve agravado cuando, además, existen materiales muy absorbentes y las partículas son en su mayoría absorbidas. En muchos de estos casos, realizar cálculos de transporte en un tiempo computacional asequible resulta imposible. Para solventar este problema, las técnicas de reducción de varianza global consideran todos los puntos de la geometría igualmente importantes, permitiendo un transporte homogéneo en términos del error relativo. Para generar los parámetros necesarios para la aplicación de reducción de varianza global, los métodos híbridos realizan cálculos previos del flujo neutrónico con códigos deterministas; estos parámetros son posteriormente empleados como entrada en una simulación de Monte Carlo (más precisa en geometrías complejas que los métodos deterministas). Actualmente existen varias técnicas que reducen la varianza de forma global, siendo el método híbrido FW-CADIS la técnica de referencia.

El objetivo principal de esta tesis es implementar un método de reducción de varianza global para cálculos de transporte neutrónico realizados con el código de transporte MCNP (basado en el método de Monte Carlo), sin la necesidad de un código determinista. Para ello, en la primera parte de esta tesis se presenta un repaso de las principales técnicas de reducción de varianza global que existen actualmente para el transporte de neutrones. Se describen los puntos fuertes y las limitaciones de cada método y se hace especial hincapié en la técnica de van Wijk. Ésta metodología, puramente estocástica, presenta ciertos problemas para geometrías complejas con materiales muy absorbentes. Estos inconvenientes son estudiados y se proponen dos soluciones en función de los resultados obtenidos.

La segunda parte de esta tesis consiste en aplicaciones de las técnicas propuestas así como del algoritmo original de van Wijk, usando dos geometrías diferentes. Para ello se

propone en primer lugar el *benchmark* de ITER, una geometría simplificada que se emplea para la verificación de herramientas. Sobre este modelo, un caso análogo (sin reducción de varianza), el algoritmo de van Wijk y las modificaciones propuestas, son comparados en términos de optimización del tiempo computacional y del muestreo sobre toda la geometría. Además, se realiza una verificación de la fiabilidad de los métodos, comparando para ello el flujo neutrónico calculado en una región del espacio con el caso análogo de MCNP.

La segunda geometría es más compleja y de mayores dimensiones; se emplea en este caso el modelo neutrónico del reactor fusión ITER. Se muestran sobre este modelo las mismas comparaciones de optimización realizadas en el *benchmark.* Además, los mapas provenientes de los dos métodos más optimizados son posteriormente empleados para realizar un cálculo de dosis en parada sobre el puerto ecuatorial del reactor.

En esta tesis se proponen dos optimizaciones de técnicas de reducción de varianza global para el transporte con el código MCNP, sin la necesidad de emplear un código determinista para los cálculos previos. Las aplicaciones mostradas demuestran la consistencia en los resultados obtenidos cuando se comparan con una simulación análoga, así como la mejora en el tiempo computacional del transporte.

ABSTRACT

In the field of nuclear fusion reactor design, the study of neutronics is of particular relevance. The neutrons released by the fusion reactions that take place in this type of reactors carry a large amount of energy, which will eventually be transformed to generate electricity in future fusion power plants. However, the adverse outcomes caused by these neutrons, such as the capability of activating materials or their harmful effects as ionizing radiation, requires a proper characterization of the neutron distribution within the reactor.

In order to achieve a proper assessment of the neutron fluxes within the reactor, the neutrons must be transported throughout its geometry; considering all the interactions they encounter with the materials along their trajectories. For this purpose, the transport codes based on the Monte Carlo sampling method are widely used in the nuclear industry. However, its applicability is limited by the current computing capabilities.

To optimize the neutron transport, there are several techniques (implemented in the Monte Carlo codes) that reduce the variance of the sampling, hence reducing the computational effort. Nevertheless, when characterizing a system within all the points in its phase-space, these techniques are not enough, due to them being locally oriented. Therefore, in large geometries where characterization of certain response functions (such as dose or decay heat, amongst others) is needed throughout the entire phase-space, the transport codes based on Monte Carlo sampling require a great amount of computational effort. This problem is enhanced when, in addition to the large region in need of sampling, highly absorbent materials are present, and most of the particles are absorbed. In most of these cases, transport calculations performed within an acceptable computational time

becomes an impossible task. To solve this problem, global variance reduction techniques consider all points throughout the geometry as equally important, allowing a uniform transport in terms of the relative error. Hybrid methods generate the necessary parameters for the implementation of the global variance reduction techniques by calculating the neutron flux using deterministic transport codes; these parameters are subsequently used as part of the Monte Carlo input for a final simulation (since the Monte Carlo simulations are more precise when dealing with complex geometries). Currently, there are several techniques that globally reduce the variance, being the hybrid FW-CADIS technique the reference method.

The main goal of this thesis is to implement a global variance reduction method for neutron transport calculations performed with the MCNP transport code (based on the Monte Carlo sampling method), without the need of a deterministic code. To achieve this, in the first part of this dissertation an overview of the existing global variance reduction techniques for neutron transport is presented. The strengths and limitations of each method are described and special emphasis is made on van Wijk's methodology. This purely stochastic technique presents several issues for complex geometries featuring highly absorbent materials. These problems are examined and based on the results two solutions are proposed to overcome them.

The second part of this thesis consists of the application of the proposed techniques, as well as van Wijk's original algorithm, using two different geometries. In the first place, ITER's computational benchmark is used; this model consists of a simplified geometry used for verification purposes. Over this model, an analog run (without variance reduction), van Wijk's algorithm, and the proposed modifications are compared in terms of computing

time optimization and sampling throughout the geometry. Additionally, a verification of the reliability of the methods is performed by comparing the calculated neutron flux in a defined region with the MCNP analog run.

The second geometry used, the ITER neutronics model, is significantly larger and more complex; and the same comparisons as the ones performed over the benchmark are made. In addition, the maps for the two most optimized methods are used to calculate the shutdown dose rate over the equatorial port of the reactor.

In this thesis two optimizations of global variance reduction techniques are proposed for the MCNP transport code, without the need of using a deterministic code for the previous calculations. The applications presented show consistency in the results when compared to an analog simulation, as well as a significant improvement of the computational time.

1. Introduction

1.1. Energy demand and trends

The currently increasing energy demand calls for a sustainable path in energy production to mitigate the environmental impact. Taking action towards global warming, 196 Parties at the United Nations Climate Change Conference under the Cancun Agreement in 2010 settled a long term objective of restraining the global average temperature increase below 2ºC. However, the energy demand is expected to grow by almost one third in the 2013-2040 year gap [1]. These projections come hand in hand with an increase of carbon dioxide (CO_2) emissions, which is the primary greenhouse gas released as a consequence of human activities. At the same time, the cumulative effect of these types of gases, due to their long lifetimes, must be taken into account. Therefore, to comply with the settled 2ºC mark, it's been estimated that a maximum CO_2 emission of 3000 Gt can be sustained, of which about 65% of these estimations had already been emitted before 2014 [2].

The energy sector is actually the largest source of CO_2, thus plans to reduce emissions must be aimed in this direction. At the moment, two thirds of greenhouse gas emissions come from the energy sector, where 80% of the total primary demand is met from fossil fuels (coal, gas, and oil). Moreover, 90% of CO_2 emissions in the energy sector come from fossil fuel combustion [2]. Global CO_2 emissions have increased over 50% in the past 25 years, where in the 2000-2014 year gap the average rate has increased by 2.3% per year (Figure 1-1). Additionally, projections regarding energy demand and greenhouse gas emissions also show a growing tendency.

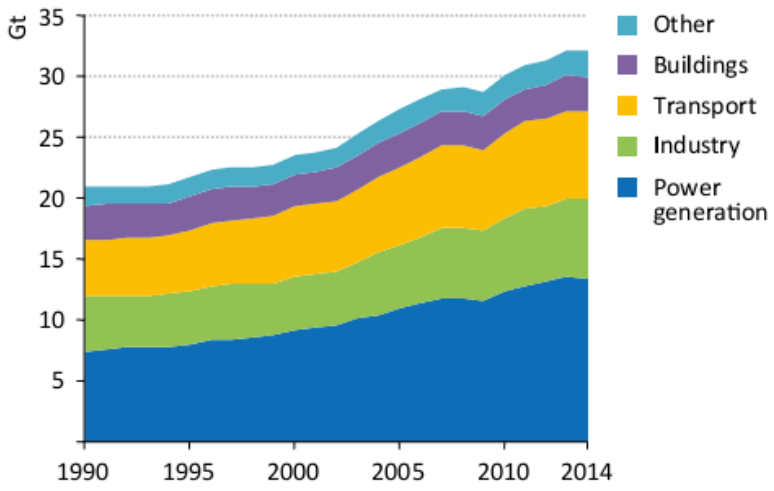

Figure 1-1 Energy-related CO2 emissions by sector [2]

According to the International Energy Agency, energy demand is estimated to grow about 1% per year through 2040. However, CO_2 emissions are projected to increase at a 0.6% rate per year in the next five years and 0.5% in the subsequent two decades [1]. The lower rate regarding previous CO_2 emissions is due to the improved energy efficiency and to the growth of renewable energy generation, which is currently the second energy source behind coal. Nonetheless, it's estimated that energy related CO_2 emissions in 2040 will be 16% higher than in 2013 [1].

Aside from the existing sources, this growing energy demand has also led to the search of new production technologies in order to keep up with this global request. Within energy production methods, advances in technology for the development of nuclear fusion power plants are currently at its peak; due to the great potential it entails to satisfy this demand and the support given by different governments around the globe. Fusion power plants will be CO_2 emission free once they start operating; yet, this technology is actually

under development in order to reach its full potential as a reliable electricity production method.

1.2. Nuclear fusion

Taking advantage of the energy released when two light atomic nuclei merge, is the starting point behind the idea of fusion power reactors. One of the first challenges to arise is which nuclei are more suitable for a fusion power plant. To answer this question, a look must be taken at the *binding energy* of the nucleons (i.e., protons and neutrons) forming atomic nuclei. The mass of a nucleus is not the sum of the masses of its constituent nucleons, instead it is found to be smaller. This is due to the binding energy of the nucleons, where the difference between the sum of their masses and the real mass of the nucleus is called *mass defect*. In fact, fusion power plants are designed to take advantage of the energy released from the mass defect after nuclei have fused.

The Semi-Empirical Mass Formula, based on the liquid drop model, can be used to calculate the binding energy of nuclei and is built taking empirical data from the mass defect. Its general form can be written as:

$$B(A,Z) = a_v A - a_s A^{\frac{2}{3}} - a_c \frac{Z(Z-1)}{A^{\frac{1}{3}}} - a_{as} \frac{(A-2Z)^2}{A} + \delta(A,Z)$$

Eq. 1-1

where A is the mass number, Z is the atomic number, and a_v, a_s, a_c, a_{as} are constants. At the right hand side of the equation are the: volume, surface, Coulomb, asymmetry, and pairing terms, respectively.

The volume term comes from the strong force binding the nucleons together, in which each nucleon interacts with *A-1* other nucleons (hence, the total interaction should be: $A(A-1)\bar{V} \approx A^2\bar{V}$, where $\bar{V}$ is the average volume). However, this would be a long distance force, and at smaller distances of ~0.5 fm ($5 \cdot 10^{-16}$ m) the strong force becomes repulsive; thus 0.5 fm is the minimum radius taken for the nucleons (r_0). At a short range, in which each nucleon is considered a sphere with ~0.5 fm radius, each nucleon will only interact with its closer neighbors. This interaction can be then taken as: $AN_n\bar{V}$, where N_n is the number of the closest neighbors (note that this is a constant number), therefore the volume term is given as proportional to A.

The surface term is a correction to the volume term, and the same reasoning can be applied. This term considers nucleons on the outer part of the nucleus, which will have fewer close neighbors than those located in the inner shells. In this case a nucleon has about $N_n/2$ close neighbors and the extra energy in the volume term has to be subtracted. For the surface term, interaction is proportional to the nucleus surface ($\propto R^2$), hence: $\propto R^2 = (r_0 A^{1/3})^2 \propto A^{2/3}$.

Repulsion between protons in the nucleus yields the Coulomb term. This term can be directly seen when the nucleus is approximated as a sphere, and its electrostatic energy is given by:

$$E_0 = \frac{3}{5}\frac{1}{4\pi\epsilon_0}\frac{Q^2}{R} = \left\{ \begin{matrix} taking: R = r_0 A^{1/3} \\ and\ \ Q^2 = e^2 Z(Z-1) \end{matrix} \right\} = \frac{3}{5}\frac{1}{4\pi\epsilon_0}\frac{e^2 Z(Z-1)}{r_0 A^{1/3}} = cte \cdot \frac{Z(Z-1)}{A^{1/3}}$$

Eq. 1-2

Note that this is a long range force affecting all the protons in the nucleus and no corrections are needed.

Nonetheless, the previous terms do not consider quantum effects within nucleons, so the asymmetry and pairing terms must be introduced. The asymmetry term takes into account Pauli's exclusion principle, which states that no two orbitals can have the same quantum numbers. This term explains why more stable nuclei are not solely, or mostly, made up by neutrons (where the previous terms seem to lead); and instead are formed by, approximately, the same number of protons and neutrons ($Z=N$). To understand this, let's consider a nucleus made up only of neutrons. Once the lower energy levels of the nucleus are filled with neutrons, higher energy neutrons must be added into it, making the total binding energy also lower. Thus, making the high mass nuclei less stable, which is simply not true since there are stable nuclei with large mass numbers. On the other hand, by adding protons (in their own proton levels) Coulomb repulsion between them also enters the energy balance. However, the repulsion is compensated by adding neutrons in the low energy levels. It is observed that binding energy is reduced symmetrically for either $Z>N$ or $N>Z$. In fact, this reduction takes quadratic form for $Z \neq N$. Therefore, ideally, stable nuclei should have $Z=N$ (i.e., $A=2Z$) and the asymmetry term can be written as: $\propto \frac{(A-2Z)^2}{A}$. Note that for $A=2Z$ the term tends to zero.

Lastly, the pairing term considers the binding energy of paired nucleons. In this case, wavefunctions of two nucleons in the same level (with opposite spins) are going to overlap, bringing them closer together and providing stronger binding energy for this pair. On the contrary, unpaired nucleons will have a weaker bond. Taking into account protons and neutrons in the nuclei, the pairing term is written:

$$\delta(A,Z) = \begin{cases} a_p A^{-3/4} & with: \ Z\ even\ and\ N\ even \\ 0 & with: \ A\ odd \\ -a_p A^{-\frac{3}{4}} & with: \ Z\ odd\ and\ N\ odd \end{cases}$$

In the Semi-Empirical Mass Formula the constants of proportionality are fitted using experimental data, and their values are: a_v~ *15.6 MeV*, a_s~ *17.8 MeV*, a_c~ *0.7 MeV*, a_{as}~ *23 MeV*, and a_p~ *34MeV.*

To finally obtain binding energy per nucleon, the Semi-Empirical Mass Formula is divided by the number of nucleons in a nucleus $\left(\frac{B(A,Z)}{A}\right)$. Large binding energy in a nucleus means that higher energy per nucleon is needed to tear the nucleus apart. Plotting *B(A,Z)* vs *A* provides further insight to how nuclear reactions can release energy (Figure 1-2). In Figure 1-2 a peak can be seen around *A=56*, making iron the most stable nuclei, afterwards the binding energy slightly decreases with *A*. The maximum also separates nuclei into two groups, in which ones are more suitable for fission and others for fusion. To the left (the lighter nuclei) the binding energy increases per nucleon with the mass number. This means that fusing two light nuclei will result in a heavier nucleus with larger average binding energy per nucleon. The increase in the binding energy will be emitted, making them favorable for fusion reactors. On the right hand side of the graph the opposite happens, and fission of heavy nuclei will result in two (or more) lighter nuclei that emit the extra binding energy from the original nucleus.

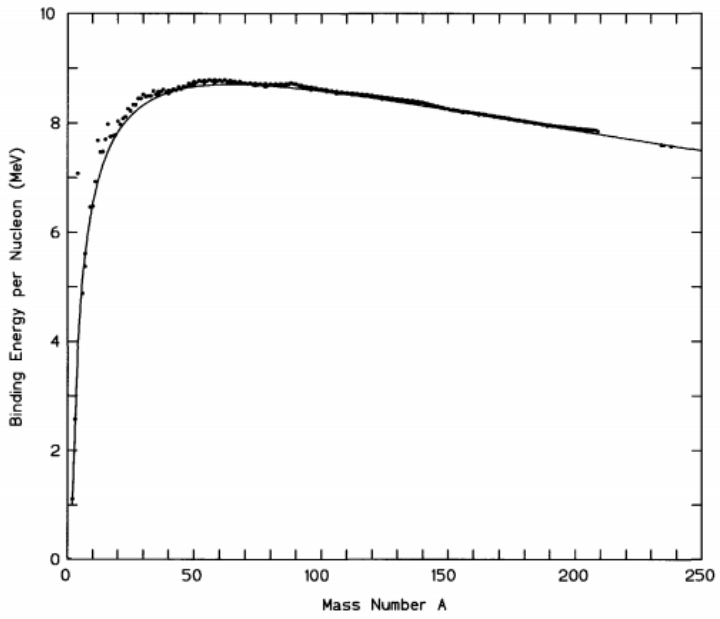

Figure 1-2 Average binding energy of nucleons vs atomic mass number [3]

However, the question to which nuclei are more viable for a fusion reactor remains to be answered. Based on the aforementioned premises, the simplest case would be hydrogen isotopes. For hydrogen isotopes the cross sections (i.e., probability that fusion will take place) have been measured experimentally in reactions involving deuterium (D) and tritium (T). To do this, deuterons were accelerated towards a solid target including deuterium, tritium, or He^3. Figure 1-3 shows the results for the D-D, D-T, and D-He^3 reactions [4]. The highest cross section obtained with the lowest energy deuteron belongs to the D-T reaction; making it, at a first sight, the best candidate for a fusion reactor.

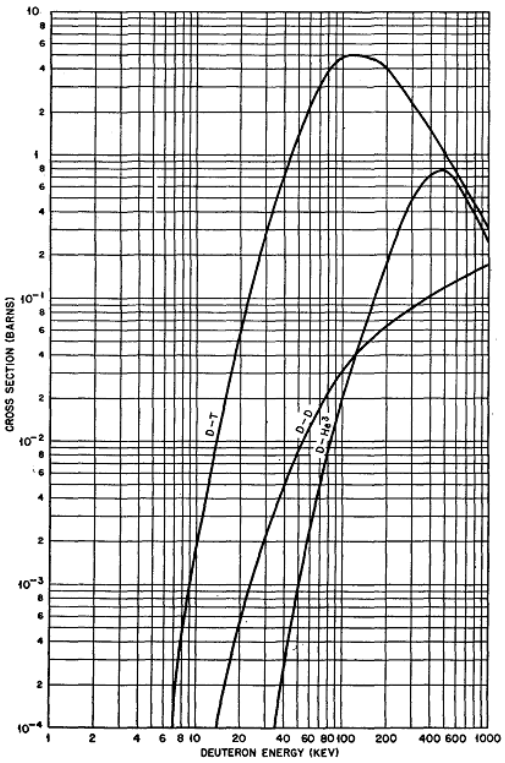

Figure 1-3 Experimental cross sections of D-D, D-T, and D-He^3 fusion reaction [4]

These reactions, as well as the released energy associated with each particle, are:

$$D + D \rightarrow He^3\ (0.82\ MeV) + n\ (2.45\ MeV)$$

Eq. 1-3

$$D + D \rightarrow T\ (1.01\ MeV) + p\ (3.02\ MeV)$$

Eq. 1-4

$$D + T \rightarrow He^4\ (3.5\ MeV) + n\ (14.1\ MeV)$$

Eq. 1-5

$$D + He^3 \rightarrow He^4\ (3.6\ MeV) + p\ (14.7\ MeV)$$

Eq. 1-6

where the reactions in Eq. 1-3 and Eq. 1-4 occur at approximately the same rate [5]. It is shown that, aside from the highest cross section, the D-T reaction also releases fast neutrons, making it an appropriate fuel but with important issues that will need to be addressed (see section 1.4).

The last question to be answered is how the fusion reactions will take place. In another experiment, where deuterium was also accelerated into deuterium, tritium, and He^3 targets, it was shown that the produced energy happened to be lower than the energy needed to accelerate the nuclei [4]. Since accelerating deuterium doesn't seem to be the optimal solution, in terms of providing energy; another approach, high temperature and pressure conditions (to increase the energy of the nuclei in the fuel), seems to be the answer.

Under extremely high temperatures most of the electrons will be stripped from the atoms, forming an ionized gas system known as *plasma*. Once the exothermic reactions begin to take place, part of the released energy can also be used to maintain the plasma state. However, to maintain the high temperature and to avoid damage in the structural materials plasma needs to be confined.

To further understand confinement in fusion reactors, consider the efficiency of a reactor: $Q = P_{Fusion}/P_{Heating}$, where P_{Fusion} is the power generated by the fusion reactions and $P_{Heating}$ is the power needed to heat fuel (D-T). For the fusion reactions to be at least self-sufficient certain conditions must be met. First, the *breakeven* point must be achieved, in which the energy released by the plasma is in equilibrium with the energy needed to produce it ($Q = 1$). Once all external heat sources can be turned off, *ignition* is reached and

the energy released by the plasma exceeds the energy required for its confinement and production (ideally $Q \rightarrow \infty$). To accomplish these steps, the relation between ion density, minimum time of confinement (to compensate energy losses that may occur), and temperature of the plasma, is defined by the Lawson criterion [6]. Related to this criterion the *triple product* is used as a figure of merit, establishing a certain value above which the breakeven point or ignition occur [7]. In a D-T plasma the triple product for breakeven point and ignition is defined respectively by [8]:

$$n\,T\,\tau_E \geq 0.5 \cdot 10^{21}\ keV\ s/m^3$$

$$n\,T\,\tau_E \geq 3 \cdot 10^{21}\ keV\ s/m^3$$

where *n* is the ion density, *T* is the temperature, and τ_E is the time of confinement. As an example, keeping in mind that for the D-T reaction to be optimal temperature must be at least *10 keV* (*~116 MK*) and taking an ion density of $n=10^{20}\ m^{-3}$, the time of confinement must not be less than *3 s* for ignition.

According to the previous requirements, two approaches can be taken in order to reach ignition: a short time span for confinement with large ion densities or longer time periods with a moderate ion density. For the first case, inertial confinement is proposed; whereas for the second a magnetic confinement is pursued.

1.2.1. Inertial confinement

The idea behind inertial confinement (IC) is to obtain the fusion reactions as fast as possible so the clustered nuclei don't have enough time to separate. This can be achieved through small fuel pellets that are simultaneously heated and compressed with laser or ion-

beam pulses until the plasma state is reached, producing the fusion reactions. The biggest challenge that IC faces is to obtain enough amplification of the laser beam in order to gain energy through the fusion process. As a result, a different approach known as fast ignition was proposed. In this approach the compression of the fuel pellets is done separately from the heating process. First, the pellets are compressed through a laser system and when maximum density is achieved a second short pulse laser is responsible for heating them. By separating these steps energy gain is estimated to improve, since the energy input is also reduced [9].

The National Ignition Facility (NIF), at the Lawrence Livermore Laboratory, was built in 2009 with the goal of achieving ignition through IC. It's the most important IC facility and has the world's largest laser. Their ignition experiments are done using "indirect-drive", in which the fuel pellets are not targeted directly by the laser beams. Instead, a gold cylinder is holding the pellet and laser beams penetrate its interior through holes in the top and bottom parts of the can. The laser hitting the inner walls of the cylinder produce x-rays which heat up its interior causing the fuel capsule to implode [9]. In 2014 NIF reported that, for the first time, released energy surpassed the energy absorbed by the fuel (though not the energy provided to the lasers) [10]. However, up to date the NIF has not reached ignition.

1.2.2. Magnetic confinement

Magnetic confinement encloses the plasma using magnetic fields, allowing longer time periods with a smaller nuclei density. In this approach the plasma is moving, due to its charged particles, through the magnetic field lines, allowing a larger number of fusion

reactions. The magnetic fields are able to enclose and isolate the plasma to avoid its cooling by touching the walls. Applications in this dissertation are made using a magnetic confinement reactor model hence a more detailed insight of this technology is given in the next section.

1.3. Technological roadmap towards magnetic confinement reactors

1.3.1. Magnetic confinement fusion reactors

Taking advantage of the charged nature of plasma, magnetic fields can be used to control and isolate the fuel of a fusion reactor. In terms of reducing plasma loss the most effective magnetic configuration is a closed loop contrarily to a linear arrangement. In linear configurations stronger magnetic fields are placed at the ends, thus slowing particles down and reflecting most of them; although some high speed particles are not stopped by these “mirrors”, leaking out of the system. However, these design challenges are beyond the scope of this work.

On the other hand, when selecting a closed trajectory arrangement, ions and electrons are forced to travel through the magnetic field lines following circular orbits and forming helical paths around these lines. Nonetheless, the field lines must also be curled in order to maintain the intensity of the magnetic field throughout the entire orbit; thus avoiding loss of density and temperature of the particles in the weaker outer layers of the field. Accordingly, the optimal configuration for a magnetic confinement seems to be a helical magnetic field (see Figure 1-4).

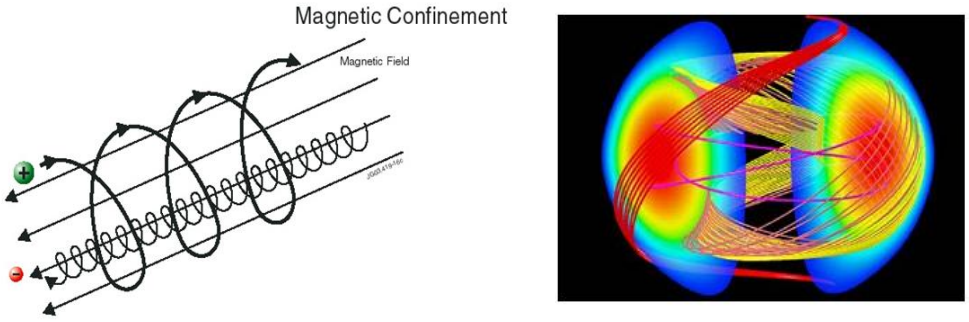

Figure 1-4 Charged particle trajectories along the field lines (left) and helical field (right) for the magnetic confinement of plasma [11]

There are two main reactor configurations that fulfill these requirements; namely the t*okamak* and the s*tellarator*. The tokamak confines the plasma in a toroidal shape by two main magnetic fields. A toroidal field is induced by external toroidal field coils; whereas an electric current within the plasma generates the poloidal field. In order to achieve a proper confinement, the toroidal field is usually ten times larger than the poloidal field. Eventually, to correct the position of the plasma an additional third poloidal field must be introduced (Figure 1-5). One main disadvantage of the tokamak concept is the operation in pulse mode. This is due to the current in the plasma, induced by a transformer, increasing continuously until it reaches a maximum value; afterwards, the pulse will stop for the transformer to discharge and current must again be induced from the start.

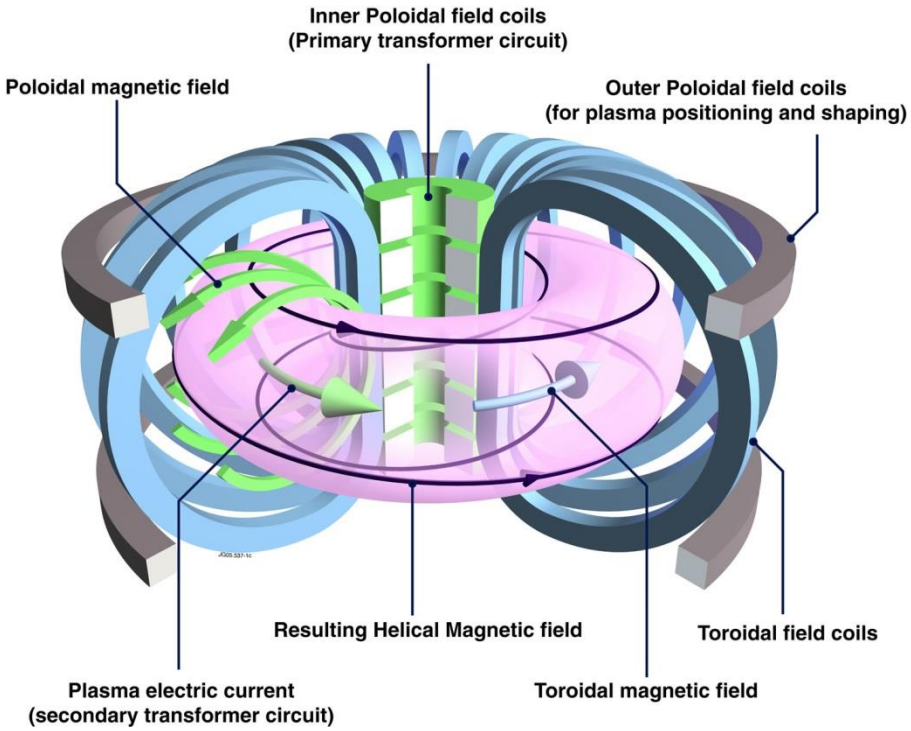

Figure 1-5 Arrangement of the magnetic circuits and fields in a tokamak reactor [7]

Correspondingly, a stellarator operates in a similar arrangement but with the poloidal field induced by helicoidal coils and in this case there is no current induced in the plasma (Figure 1-6). Thus, allowing a continuous operation and making them an optimal candidate for future commercial reactors. On the downside, their design is significantly more complex. The applications of the developments presented in this dissertation are focused on the future International Thermonuclear Experimental Reactor (ITER), a tokamak configuration (see 1.3.3); therefore further discussion will be centered on these reactors.

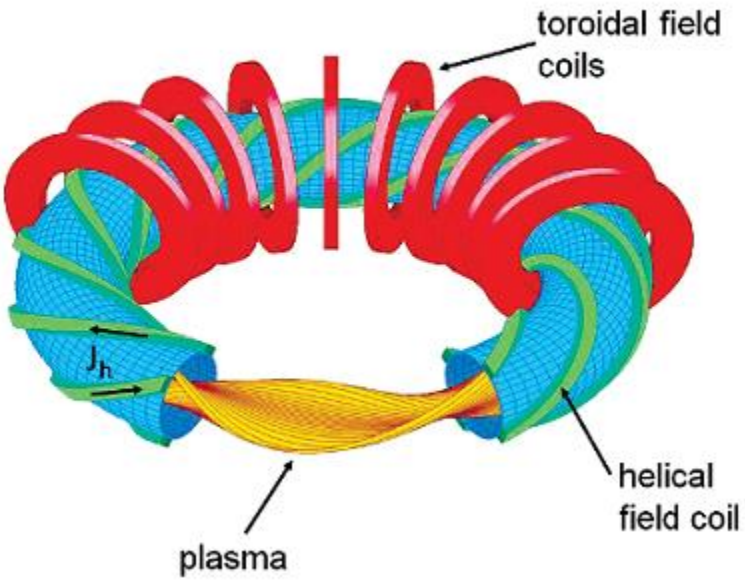

Figure 1-6 Configuration of the magnetic coils in a stellarator [12]

1.3.2. Technological challenges

Operating under unexplored circumstances different challenges are faced towards research advances in future tokamak reactors. Some of the major challenges in the design will be overviewed in this section, whereas a deeper insight of dealing with high energy neutrons is presented in section 1.4.

The first question that must be answered in a tokamak is how to obtain the plasma state in the fuel. Temperatures inside ITER will reach $1.5 \cdot 10^8$ ºC (ten times the temperature in the Sun's core) with three external heat sources that must provide 50 MW of heating power. The Neutral Beam Injection (NBI) system will shoot uncharged high-energy particles that will transfer their energy to the plasma by collision. At ITER, these particles come from accelerated to 1 MeV deuterium atoms; where two NBI systems each delivering

a 16.5 MW beam (with particle energies of 1 MeV) are anticipated. In neutral beam injection systems, positively charged ions are accelerated by an electric field and recover their missing electron by passing through a cell containing gas before being injected into the system. However, at ITER negatively charged ions will be used; due to ITER requiring the particles to be accelerated three to four times faster than previous systems, and at these rates positively charged ions are harder to neutralize. For the NBI system at ITER, the additional electron of the accelerated negative ion is loosely bound and will be easily lost before entering the plasma [13]. The other two heating systems are sources of high-frequency electromagnetic waves. Ion Cyclotron Resonance Heating (ICRH) will transfer energy to the ions in the plasma by a high-intensity beam of electromagnetic radiation with a 40-55 MHz frequency. Lastly, the Electron Cyclotron Resonance Heating (ECRH) will heat electrons in the plasma using a high-intensity beam of electromagnetic radiation at the resonant frequency of electrons, 170 GHz [13].

The materials used to maintain structural integrity of a nuclear facility is a whole field in itself. Significant effects are caused in the materials due to the high temperatures, intense neutron fluxes, and (for magnetic confinement reactors) the magnetic stress; hence properties of the materials are also affected. In order to deal with selecting the proper materials, components have to be classified according to their position and purpose, and loading conditions have to be determined so a thorough analysis on the materials can be performed.

Attention at the huge magnetic fields needed to confine the plasma must be given. In order to obtain the required force in the fields, large size coils should be used. However, space is limited and the efficiency of large magnets must be kept as high as possible to

improve energy gain in the reactor. Consequently, superconducting coils will be used to operate tokamaks. The two main advantages of using these types of magnets are their reduced size (compared to cooper coils) and the low resistivity they present, which results in high efficiency. The materials that will be used for these magnets are niobium-tin (Nb3Sn) or niobium-titanium (Nb-Ti), due to their superconducting properties when cooled (with supercritical helium) in the 4 Kelvin range [13].

As stated previously, an efficient fuel to use in fusion reactors is D-T. Following Eq. 1-5 this nuclear reaction releases He^4 and fast neutrons. Contrarily to neutrons, helium nuclei are charged allowing them to be retained in the magnetic field within the plasma. In order to reach ignition this is an advantage, since their energy (~3.5MeV) can be retained to aid in maintaining the high temperatures. However, once the energy is transferred to the fuel these ions become an impurity that cool and dilute the plasma. To remove these (and other impurities that may appear from neutrons interacting with the walls) as well as protecting walls from thermal and neutronic loads, a *divertor* will be placed at the bottom of the chamber housing the reactions (i.e., the *vacuum vessel*). The plasma facing components of the divertor are targets positioned where particle bombardment is especially harsh. Accordingly, when particles hit the targets their energy is transformed into heat that will subsequently be removed by a cooling system. Alignment of the divertor must be precise and materials that can resist the conditions have to be used. Having to endure heavy loads and high temperatures, tungsten will be used as the armor material due to having the highest melting point, of which qualification activities have been ongoing for years [13]. The *blanket* is another component directly facing the plasma, but it will be further discussed in sections 1.4.1 and 1.4.2.

1.3.3. Facilities timeline

A timeline of the relevant facilities on the path towards a fusion power plant based on the tokamak model are presented next. The first tokamak, the T-3, was built at the Kurchatov Institute (Moscow). In 1968 it was reported that the T-3 had produced plasmas with a temperature over 10 keV (over 10 million degrees) [7]. This breakthrough set ground for international funding of nuclear fusion reactors based on the tokamak model. Several small tokamaks have been built since, providing further insight into fusion research. Nonetheless, the most notable achievements have been accomplished by the largest tokamaks up to date. These are: the Tokamak Fusion Test Reactor (TFTR) that operated from 1982 to 1997 in the USA, the Joint European Torus (JET) built in 1983 in the UK, and the Japan Torus (JT-60) built in Japan in 1985, which is currently being upgraded.

The TFTR, built at the Princeton Plasma Physics Laboratory was the first tokamak to thoroughly research D-T fuels. In 1993 it accomplished a world record burst of over 3 MW of fusion power using equal parts of D-T, settling the convenience of a 50%/50% fuel mixture. This mark was passed the following day, in which a second shot surpassed 6 MW of fusion power, and the consecutive year, in which the TFTR achieved over 10 MW [14]. However, this last record was later surpassed by the JET reactor, located at the Culham Centre for Fusion Energy (CCFE), which in 1997 obtained 16 MW of fusion power (the actual record). This experiment produced an input/output ratio of Q=0.65, and breakeven point (Q=1) is yet to be achieved. The JET facility is the largest tokamak in operation today and the focal point of European fusion research.

The JT-60 located at the Naka Fusion Institute began operating in 1985 using hydrogen plasmas. An upgrade in 1991, JT-60U, allowed the rector to use deuterium plasmas; and later, in 2008, operations ended for a larger upgrade, the JT-60SA. This modification will reuse some of the JT-60U facilities to build a superconducting tokamak that is expected to achieve its first plasma in 2019. The JT-60SA facility will model proposals to optimize plasma operation and investigate advanced plasma modes to be used in future fusion reactors [13].

The Tore Supra tokamak, located at the Institute for Magnetic Fusion Research (in Cadache, France) has been in operation since 1988. It was the first tokamak to satisfactorily implement superconducting magnets and actively-cooled plasma facing components [13]. Currently, it holds the record for the longest plasma pulse (6.5 minutes), achieved in 2003. It is now being reconfigured as a testing facility (WEST) for the tungsten plasma facing components in the future ITER facility.

ITER will be an experimental tokamak destined to prove viability of fusion as an energy source. Research of plasma physics and testing of different technologies for future fusion power plants will take place during its operational phase; making it one of the most complex and challenging engineering projects in the world.

In 2006 a seven Party international collaboration was agreed to build the future ITER experimental reactor. The ITER platform at Cadarache, France, was ready in 2009 to receive scientific buildings and facilities of the project from its constituent Parties: China, the EU, India, Japan, South Korea, Russia, and the USA. It is planned to achieve operation with $Q \geq 10$ producing 500 MW of fusion power. In addition, it pursues several

technological goals, amongst these are: the confinement of D-T plasma with dominating heating from alpha-particles, testing tritium breeding in situ, demonstration of safety features, and component testing required for a fusion power plant. Even though it is currently under construction, the design of certain component specifications is still under development.

The ITER tokamak will be the largest experimental fusion facility built up to date. Such a big project relies on the research of other facilities like the aforementioned WEST. Other major contributions are the International Fusion Materials Irradiation Facility (IFMIF) and the Korean Superconducting Tokamak Reactor (KSTAR). IFMIF is an accelerator based neutron source that is expected to generate a neutron fluence equivalent to the anticipated for ITER. It will allow the characterization and validation of suitable materials to aid in the design of components tolerant to radiation. IFMIF is expected to present results parallel to ITER operation, in order to design future plants. Its accelerator will be validated by the Linear IFMIF Accelerator Prototype (LIPAc), currently under construction in Rokkasho, Japan; that will accelerate a current of 125 mA deuterons at 9 MeV [13].

Located at the National Fusion Research Institute (NFRI) in South Korea, KSTAR's first plasma was achieved in 2008. Its superconducting magnets and cooling systems will aid in the design and operation of ITER; since it's the first tokamak to use Nb3Sn superconducting magnets (the same material projected for ITER coils). Aside from being a satellite facility for ITER, it will also contribute to research for future demonstration fusion power reactors (DEMO).

The last step towards a commercial fusion power plant is the construction of a DEMO machine. At the moment different conceptual DEMO projects are under consideration, based on the technologies developed for ITER. Moreover, the main goal of a DEMO plant is to demonstrate the feasibility of electricity production, operating and generating energy under reliable conditions. It is expected to produce 2000-4000 MW of power output and achieve a $Q \geq 25$. A comparison between the JET, ITER, and DEMO devices is shown in Figure 1-7.

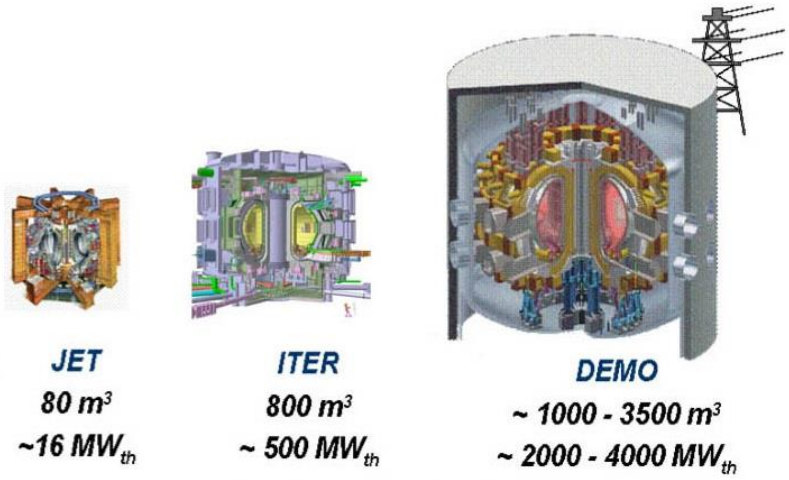

Figure 1-7 Comparison between the JET, ITER, and DEMO reactors

1.4. Nuclear radiation in fusion reactors

The next sections are dedicated to the advantages and challenges caused by the fast neutrons released during the D-T reactions. First, an overview of dealing with neutrons in the vacuum vessel is presented followed by an outline of the tritium production expected in

fusion reactors. In the last two sections some definitions regarding nuclear interactions and dosimetry are reviewed, which lead towards how to address shielding neutral particles.

1.4.1. Nuclear energy deposition

As a result of the D-T reaction (Eq. 1-5) the energy of the neutrons released will be turned into fusion power. Nonetheless, their high energy presents a concern regarding the facility structure and the superconducting magnets. To deal with this problem and also obtain the neutrons energy, the inner walls of the vacuum vessel will be covered with *blanket* modules. Each blanket module consists of two components: a first wall panel (facing the plasma) and a shielding block.

The blanket system is designed to absorb radiation and heat flux derived from the plasma, and to provide shielding that will reduce heat and neutron loads. In future fusion reactors, tritium breeding (see 1.4.2) and power generation will also take place in the blanket. To obtain energy that will subsequently be turned into electrical power, neutrons are slowed in the blanket and their kinetic energy is transformed into heat energy. This heat will then be collected by the water coolant system.

Even though no power generation will take place in ITER, it will include a water cooling system designed to remove heat from the vacuum vessel and auxiliary systems. This system will be hosted at the blanket modules and is planned to remove over 700 MW of thermal power [13].

Regarding materials, the blanket first wall is one of the components directly facing the plasma and, as such, low plasma contamination materials are needed. For ITER, the

first wall is covered with beryllium whilst the rest of the blanket will be made of high-strength copper and stainless steel. In addition, some regions inside the vacuum vessel are subject to a higher heat flux. The beryllium panels in these areas are designed to endure the largest fluxes, and during ITER's lifetime they are expected to be replaced at least once [13]. Behind the beryllium panels, shielding blocks made of stainless steel will protect the vacuum vessel and coil systems.

1.4.2. Tritium production

Obtaining the fuel for a fusion reactor operating with D-T has the disadvantage of access to tritium. Deuterium is abundant in seawater (with a concentration of *33mg/l*) and can be extracted through a well-known process. However, the half-life of about *12.5* years for tritium isotopes results in limited availability. To solve this problem, breeding tritium in the reactor is projected through lithium embedded in the blanket. Acting as a breeding blanket surrounding the plasma, it will feed the reactor during operation. These blanket modules are planned to multiply and absorb part of the generated neutrons in order to produce the tritium according to the reactions:

$$Li^6 + n \rightarrow He^4 + T + 4.8\,MeV$$

$$Li^7 + n \rightarrow He^4 + T + n - 2.5\,MeV$$

Note that the reaction with Li^7 is endothermic, but it must be kept in mind that the highest cross section appears for fast neutrons; and that its resulting neutron is likely to interact with the Li^6.

Six different tritium breeding concepts, the Test Blanket Modules (TBM), are to be researched during ITER's operation phase to assess their technical potential. In order to do so, three of the equatorial ports (i.e., openings) in the vacuum vessel will be dedicated to hosting the Test Blanket Systems (TBS), which comprise TBMs and additional systems (cooling, tritium extraction…). The European contributions to the TBM program are the Helium Cooled Pebble Bed Blanket (HCPB) and the Helium Cooled Lithium Lead Blanket (HCLL) blanket prototypes. Overall, the difference between them lies in the type of materials used for the tritium breeder: the HCPB uses lithium in the form of ceramic pebbles and the HCLL uses liquid lithium-lead metal to breed tritium, whilst both use helium as a coolant. Currently, the breeding system concepts are in the design phase.

1.4.3. Radioprotection

Future fusion power plants are going to use part of the energy of the released neutrons to subsequently transform it into electricity. Nonetheless, these primary neutrons bring up some concern, since they will also interact with nuclei present in the reactor structure materials. In this section some definitions are given in order to fully understand the importance of radiation shielding in nuclear reactors.

Prompt radiation is the radiation produced by the plasma (neutrons) and immediate secondary radiation produced by neutron interactions with matter; an overview of these interactions is given next. The principal reactions produced from interactions of neutrons (with energy under *20 MeV*) with matter are: elastic scattering *(n, n)*, inelastic scattering *(n, n')*, absorption with charged particle emission (e.g., *(n, p)*), radiative capture *(n, γ)*, and *(n, 2n)* and similar reactions (fission *(n, F)* reactions are not relevant in fusion facilities;

therefore they will not be discussed here). In *elastic scattering* reactions, part of the energy of the neutron is transferred to the recoiled target particle, thus total kinetic energy is conserved. Elastic scattering is the most important reaction used to slow down fast neutrons. On the other hand, for reactions that result in *inelastic scattering*, the neutron is absorbed by the target nucleus, which is then reemitted. In the process, energy is absorbed by the nucleus leaving it in an excited state, which will lead to the emission of a gamma during de-excitation. *Absorption with charged particle emission* differs from inelastic scattering in that the emitted secondary particle is a charged particle. As with inelastic scattering, the excited nucleus will subsequently emit a secondary particle. *Radiative capture* is predominant in thermal neutrons (i.e., low energy neutrons) interacting with heavy nuclides. It results in the neutron being absorbed by the target that will release its exceeding energy through gamma emissions. Lastly, reactions where more than one neutron is emitted (e.g., *(n, 2n)* or *(n, 3n)*) occur at high energies. In these cases the excited target nucleus emits more than one neutron (note that these are always low energy neutrons) instead of other secondary particles [15].

For the inelastic scattering, absorption with charged particle emission, and radiative capture reactions, after the incident neutron reaches the target nucleus part of its kinetic energy is absorbed by the nucleus, and a single excited *compound nucleus* is formed. This compound nucleus will reach equilibrium by emitting prompt secondary particles (gammas, neutrons, or light charged particles). However, the *residual nucleus* may in turn be unstable and further emit *delayed radiation*. A material is said to be *activated* if it contains unstable residual nuclei.

The rate (i.e., number of atoms that decay per unit time) at which the nuclear disintegration occurs in the activated materials is called *activity*. Its units are the Becquerel

(Bq), which give disintegrations per unit time (1 Bq. = 1 decay per second). Activity of radioactive nuclides decreases exponentially with time and it's given by the equation:

$$A(t) = -\frac{dN}{dt} = \lambda N$$

Where *N* is the total number of nuclei of the radionuclide and *t* is time. The decay constant, λ, is the probability that a nucleus will decay in unit time (s^{-1}) and is unique to each radioactive nuclide.

To quantify the effects of radiation on an object, the a*bsorbed dose* is defined as the energy deposited per mass unit:

$$D = \frac{1}{m}\int EdV$$

where the units are: 1 Gray (Gy) =1 J/kg. However, depending on the radiation type and the energy range, effects may vary and a weighting factor (w_R) is introduced for the *equivalent dose* to a specific biological tissue:

$$H_T = \sum_R w_R D_{T,R}$$

where *T* refers to the tissue and *R* to the type of radiation. The units now are: 1 Sievert (Sv) = 1 J/kg. The sum of all equivalent doses weighted by a specific tissue weight factor (w_T) is the *effective dose*:

$$E = \sum_T w_T H_T$$

Specifically, in nuclear reactors, *shutdown dose rate* (SDR) is defined as the dose rate from gamma radiation (produced by neutron activation of the components materials), after a certain period of time once the reactor has been turned off. The SDR can be measured as absorbed dose (*Gy/h*) or as biological dose equivalent (*Sv/h*).

Additionally, the heat produced by the induced activity of the materials after the reactor is shut down is called *decay heat*, which is measured in MW. .

1.4.4. Shielding design

Despite not having any charge, attenuation and shielding of gamma and x-rays is relatively easy if a minimum thickness of a high density material is used. However, fast neutrons, aside from their deep penetration capacity, are usually accompanied by gamma rays from activated materials. These shielding issues are discussed next.

In order to protect the workers as well as the reactor components from the radiation, shield design, whilst complying with the commission guidelines, is an important feature of the design in a nuclear facility.

The first phase of a shield design is the definition of the problem. This includes: definition of the source (angular and spatial distributions, energy spectrum, and intensity), specifications of the geometry (material compositions and densities in the geometry of the system), and definition of the desired response functions. In a fusion reactor the source definition and geometry of the reactor, including the spaces retained for the shields is always given. The most relevant part of the design is the geometry and materials specification of the shield. In a fusion reactor, the main goal of a shield design is to

attenuate the neutron flux several orders of magnitude, to decrease as much as possible prompt particles and materials activation. This can be accomplished by using absorbent materials that ideally have as low activation as possible. However, one of the biggest challenges of shielding neutral particles is their deep penetration capacity. Attenuating them is dependent on the energy of the incident particles, atomic number and density of the shielding material elements, and thickness of the shield. In other words, to properly shield neutrons and gamma rays, materials with a high macroscopic cross section (dependent on the elements of the shielding materials and energy of incident particle) must be used, while thickness of the shield provides attenuation for a sufficient distance; this can expressed by the formula [3]:

$$I = I_0 e^{-\Sigma_t \cdot x}$$

where I is the intensity after shielding, I_0 is the incident intensity, Σ_t is the macroscopic total cross section and x is the thickness of the shield. Thermal neutrons (i.e., with an energy of 0.025 eV) are easily absorbed with certain elements like cadmium or boron. For fast neutrons (i.e., with energy range of 1-20 MeV) materials with a high content of hydrogen, such as concrete or water, are used to moderate them (i.e., slow down) before absorption.

The second step is radiation transport in order to characterize the system. In this step radiation data is specified and, depending on the desired accuracy and complexity of the problem, a calculation method is chosen to transport the radiation from the source to the specified detectors and obtain the response function. As part of the design requirements, radiation data to be used (i.e., specific libraries) are also specified. Using a simulation transport code is necessary for neutron transport. Namely, neutron interactions are usually

followed by gamma emissions that must also be shielded with additional materials. Aside from the gamma production, scattered neutrons will also change their direction of travel and energy. Accordingly, in order to characterize a system and build an efficient shield, holding record of all the particle tracks can be a complicated task after several scatters; since cross sections are dependent on the atoms in the material and the energy of the particle. For this purpose *transport theory* is required. The next chapter is entirely dedicated to this subject.

As a last step, verification and analysis of the behavior of the shield has to be done. If the obtained response function does not meet the specifications criteria (e.g., maximum dose permitted by regulations) design of the shield must be modified. Naturally, any additional modifications have to comply with the specified constraints.

The main purpose of this work is the optimization of computer simulations for neutron transport. Therefore, a wider scope regarding transport theory and computational methods is given in the next chapter.

1.5. Dissertation organization

In addition to their importance as an energetic source for fusion reactors, the harmful effects, caused by the released neutrons, require proper characterization of the neutron distribution inside a system. Knowing the neutron flux at a given point inside the reactor is essential in order to evaluate response functions such as the activation of the materials or the produced dose, amongst others. To evaluate neutron fluxes, neutrons must be transported through the system, taking into account the different interactions of the

neutrons with the materials they encounter. In order to achieve this, and characterize a system, computer simulation codes must be used to solve the equations that rule neutron transport.

In Chapter 2 of this dissertation the Boltzmann equation for radiation transport is introduced. Two numerical approximation methods used to solve the equation are also presented: the Discrete Ordinates method and the Monte Carlo method. A more detailed insight is given for the Monte Carlo method, since the main goal of this work is to optimize calculations using the MCNP particle transport code, based on this technique.

Chapter 3 is dedicated to global variance reduction techniques. The main motivation of this work is discussed, followed by an overview of the state of the art regarding global variance reduction methods. Problems derived from the application of one the techniques (i.e., van Wijk's methodology) are analyzed, and two modifications proposed to overcome the issues that were found are then described.

The next two chapters are dedicated to applications of the proposed methodologies. In Chapter 4, the ITER computational benchmark (designed to test and validate methodologies) is used to compare optimization results of the modified global variance reduction techniques with the original algorithms and analog (with implicit capture) Monte Carlo simulations. The reliability of each technique is also validated with the analog Monte Carlo run.

Chapter 5 is comprised of two applications over the entire ITER neutronics reference model. First, the same comparisons that were performed over the benchmark model are carried out, but this time using the larger and more complex geometry of the

ITER reactor. The second application makes use of the most optimized global weight maps, resulting from the previous calculations, to calculate the SDR over a large region of the reactor (i.e., the equatorial port).

Lastly, a brief summary of this dissertation, conclusions, and recommendations for future work are given in Chapter 6.

2. Resolution of the transport equation

One of the main challenges in the process of a nuclear reactor design is to predict the neutron distribution inside the system in terms of space, energy, and time. This can be done via the transport equation; however, its analytical resolution is not possible and numerical approximation methods have to be used to solve the equation. In this chapter, the transport equation is presented and the numerical methods used to solve the equation are briefly described. The Monte Carlo method, used in this dissertation, will be explained in more detail.

2.1. Transport equation

The transport equation (based on the linear form of the Boltzmann equation that describes the statistical distribution of particles in a fluid) establishes a balance of the events that cause particles to be gained or lost from a phase-space.

In neutron and gamma transport problems for a non-multiplying medium (i.e., without fission sources), the transport equation is given in its steady-state form for a fixed source problem. This type of problem describes a time-independent neutron flux distribution; due to a time-independent source providing neutrons that will eventually reach

equilibrium with the absorbed or leaked neutrons from the system. Hence, the steady state transport equation can be expressed as [16]:

$$\widehat{\Omega}\nabla\Phi\left(\bar{r},\widehat{\Omega},\mathrm{E}\right)+\ \Sigma_{Total}(\bar{r},\mathrm{E})\Phi\left(\bar{r},\widehat{\Omega},\mathrm{E}\right)=\int_{0}^{\infty}\int_{4\pi}\Sigma_{s}\left(\bar{r},\widehat{\Omega}'\rightarrow\widehat{\Omega},\mathrm{E}'\rightarrow\mathrm{E}\right)\Phi\left(\bar{r},\widehat{\Omega}',\mathrm{E}'\right)d\widehat{\Omega}'\mathrm{dE}'+q\left(\bar{r},\widehat{\Omega},\mathrm{E}\right)$$

Eq. 2-1

where the terms on the left side represent the particle loss events and the terms on the right are the particle production events. $\widehat{\Omega}$ is a unit vector in the direction of motion, $\Phi\left(\bar{r},\widehat{\Omega},\mathrm{E}\right)$ is the angular flux (expected number of particles at position $\bar{r}$ with direction $\widehat{\Omega}$ and energy E per unit volume per unit solid angle per unit energy, multiplied by the velocity), $\Sigma_{Total}(\bar{r},\mathrm{E})$ is the total macroscopic cross section (the total interaction cross section of a particle at $\bar{r}$ having energy E), $\Sigma_{s}(\bar{r},\widehat{\Omega}'\rightarrow\widehat{\Omega},\mathrm{E}'\rightarrow\mathrm{E})$ is the macroscopic scattering cross section (scattering probability from *E'* to *E* through the angle $\widehat{\Omega}'\rightarrow\widehat{\Omega}$), finally the last term $q\left(\bar{r},\widehat{\Omega},\mathrm{E}\right)$ refers to the particle production from external sources, independent of the flux distribution Φ.

The complex three dimensional geometries of fusion reactors and the dependency of the cross sections with the position and energy of the neutrons make it impossible to solve analytically the transport equation [16]. For this purpose, numerical methods have to be used. Before presenting them, the assumptions regarding computational transport of neutral particles (neutrons and gammas) are introduced. First, all particles are considered as points; therefore only particles with a wavelength smaller than the atomic diameter are considered. As a result of particles not having any charge, trajectories will not be altered by

electromagnetic fields, and are considered to travel in straight lines between point collisions. Additionally, neutron collisions are only considered with nuclei, and gamma collisions are considered with nuclei as well as with orbital electrons. Collisions may be considered instantaneous, with the only exception being the delayed neutrons from fission products. The low particle density, compared to atomic densities, make it appropriate to neglect particle-particle interactions. Material properties are assumed isotropic; and properties of nuclei and composition of materials are considered time-independent. Lastly, only the mean value of the particle density distribution is contemplated [17].

The Discrete Ordinates method is a technique that solves the transport equation by discretizing the independent variables. On the other hand, the use of the Monte Carlo stochastic method is a well-known alternative for neutral particle transport. Both techniques are discussed in the following sections.

2.2. Numerical method

2.2.1. Discrete Ordinates

The Discrete Ordinates method is a deterministic technique used to solve the transport equation after discretizing the independent variables (i.e., energy, direction, and spatial coordinates). This discretization converts the transport equation into a large system of linear equations that can be solved; where the solutions yield information about particle population in locations of the discrete representation of the problem. To discretize the energy variable, integration is done over several energy groups (i.e., multi-group) in which cross sections are averaged for each of the ranges. The angular domain is discretized by

taking a set of discrete directions. Lastly, the spatial domain is discretized into spatial meshes. The Discrete Ordinates method is a fast and optimal technique; however, discretization comes at a price, and uncertainties related to the truncation errors are gathered throughout the calculations.

In addition, the *ray-effect* may appear using the Discrete Ordinates method in two or more dimensional calculations. The ray-effect happens as a result of the angular discretization. It causes radiative heat or flux oscillations as the distance between the localized source and region of interest increases in low scattering mediums; in which particles tend to concentrate along the angular discrete levels. Independently, errors in reaction rates are also introduced due to multi-group approximations. To solve these problems the number of discretized angles or energy groups, respectively, have to be increased. However, a more thorough discretization requires more computation storage and time.

Is summary, when applying the Discrete Ordinates method, the accuracy of the calculations is dependent on the discretization; and improving results by increasing the energy groups, angles, or meshes in large and complex geometries, is restricted by the computational resources.

2.2.2. Monte Carlo

Aside from deterministic techniques, which solve the transport equation for the average particle behavior, stochastic methods may also be used to solve the transport equation. The Monte Carlo method will not solve the explicit transport equation; instead it will simulate a finite number of particles to obtain an estimate of the particles average

behavior. Namely, Monte Carlo will simulate the physical events that occur as particles are transported through the system. In order to do so, the variables that characterize a particle's life (i.e., initial location, direction, and energy, distance to a collision site, type of collision, and new direction of flight and energy) are sampled from their probability distributions making use of a random number generator. This way, each particle is transported through the system according to their probability distributions. During the transport process, contributions to the desired response function are collected (i.e., *scored*), and Monte Carlo's estimate of the physical quantity of interest is the average of a sufficient large number of scores from independent source particles.

Monte Carlo methods present more accuracy than deterministic calculations. However, due to the statistical nature of Monte Carlo, results are given with their associated relative errors, and minimizing these errors requires increasing the source histories, which translates into larger computing times.

A more detailed insight of the Monte Carlo method is given in the next section, emphasizing its application in particle transport problems.

2.3. The Monte Carlo method

2.3.1. Overview of the Monte Carlo method

In many cases, the high number of possible outcomes of a physical response in a system makes it impossible to obtain the average result by simply calculating the mean over

the sum of all the possible events. Under these circumstances, results can be estimated over a sample of the events; where the samples are taken from the probability distributions of each variable. The Monte Carlo method is a stochastic technique that determines the behavior of these types of systems by using repeated sampling. Specifically, it is a numerical analysis technique based on the use of sequences of random numbers to sample the variables of the probability functions governing a system.

Monte Carlo uses the characteristic probability functions of a system, as well as sequences of generated random numbers, to obtain an approximation of a desired response function. In order to predict a behavior, Monte Carlo will simulate the entire system a large number of times by selecting a single random value from the specific distribution describing each parameter of interest. This way, a large number of independent results giving possible outcomes are collected, and these independent events will be gathered into probability distributions of possible outcomes. Hence, Monte Carlo estimates the expected value of a physical quantity by averaging random independent samples. Consequently, the results are presented as distributions (not as single values) each having their own variances.

The Monte Carlo method is a thoroughly spread algorithm that can be applied to many fields such as mathematics, physics, biology, and finance, amongst others. A more detailed insight of the Monte Carlo technique and its application to neutral particles transport is given next.

2.3.2. Theory

In this section an overview of the basic concepts used in the Monte Carlo sampling algorithm is presented. The true mean, *E(x)*, of an expected value, *x*, for a continuous distribution is given by:

$$E(x) = \int x\, f(x) dx$$

Eq. 2-2

where *f(x)* is the particle score probability density function that selects a random walk which scores *x* to the desired response being estimated [18]. In a discrete distribution of *N* samples the previous equation becomes:

$$E(x) = \sum_{i=1}^{N} f(x_i) x_i$$

Eq. 2-3

The Monte Carlo estimate of the mean, $\bar{x}$, is calculated averaging the scores assigned to the random walks, x_i, for all of the sampled events, *N*, in the problem:

$$\bar{x} = \frac{1}{N} \sum_{i=1}^{N} x_i$$

Eq. 2-4

The Law of large Numbers specifies that as *N* approaches infinity $\bar{x}$ tends to *E(x)* if *E(x)* is finite [18], making Monte Carlo a proper approximation method if enough particles are sampled. In order to quantify the amount of variation expected from the samples, the variance is given by:

$$\sigma^2 = E(x^2) - \big(E(x)\big)^2 = \int \big(x - E(x)\big)^2 f(x) dx$$

Eq. 2-5

The square root of the variance, σ, is called the standard deviation and can be estimated by Monte Carlo, for large *N*, as *S* (estimated standard deviation of *x* based on the values of x_i sampled) by [18]:

$$S^2 = \frac{\sum_{i=1}^{N}(x_i - \bar{x})^2}{N-1} \approx \overline{x^2} - \bar{x}^2$$

Eq. 2-6

with:

$$\overline{x^2} = \frac{1}{N}\sum_{i=1}^{N} x_i^2$$

Eq. 2-7

As for $\bar{x}$, its estimated variance for a population *N* is given by [18]:

$$S_{\bar{x}}{}^2 = \frac{S^2}{N}$$

Eq. 2-8

A distinction must be made between *precision* and *accuracy*. The accuracy states how close the expected value of $\bar{x}$ is to the true physical response being estimated, where the difference between the true value and *E(x)* is called the *systematic error*. It depends on the physical data, modeling of the geometry, sampling techniques, approximations, etc. Precision refers to the uncertainty caused by the statistical fluctuations of the x_i being sampled in *x*. Statistical precision of each tally calculated via Monte Carlo is given by the relative error:

$$R = \frac{S_{\bar{x}}}{\bar{x}}$$

Eq. 2-9

A precision confidence interval of the results must be established, for which The Central Limit Theorem is used. This states that for a sufficient large sample *N* and with identically distributed random variables x_i with finite means and variances, the distribution of $\bar{x}$ approaches a normal distribution:

$$\lim_{N\to\infty} Pr\left[E(x) + \alpha\frac{\sigma}{\sqrt{N}} < \bar{x} < E(x) + \beta\frac{\sigma}{\sqrt{N}}\right] = \frac{1}{\sqrt{2\pi}}\int_{\alpha}^{\beta} e^{-t^2/2}\,dt$$

Eq. 2-10

Given a large sample *N*, and in terms of the standard deviation, $S_{\bar{x}}$, this can be rewritten as:

$$Pr\left(\left[\alpha\, S_{\bar{X}} < \frac{\bar{x}-E(x)}{\sigma/\sqrt{N}} < \beta S_{\bar{X}}\right] \approx \frac{1}{\sqrt{2\pi}}\int_{\alpha}^{\beta} e^{-t^2/2}\,dt\right)$$

Eq. 2-11

where α and β are arbitrary values and *Pr[Z]* is the probability of *Z*. Accordingly, for a distribution of tallies, the distribution of scoring $\bar{x}$ will be approximately normally distributed with a mean of *E(x)*, see Figure 2-1 [18]. Using standard tables for the normal distribution function, for a statistically significant sampling of a tally then *S* is approximately equal to σ, and there is a 68% chance that the true result is in the range $\bar{x}(1 \pm R)$ and a 95% chance that it is in the range $\overline{x}(1 \pm 2R)$. It stands to reason that, in order to obtain reliable results, all the physical phase-space has to be sampled properly, including "hard to reach" regions or less frequent events.

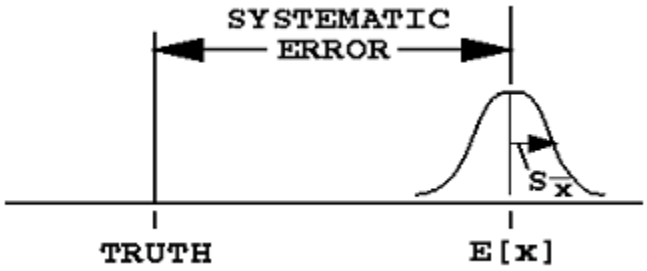

Figure 2-1 Accuracy and precision of a normal distribution [18]

Taking a closer look at the relative error (**Eq. 2-9**) and the estimated variance (**Eq. 2-8**), the next relationship can be drawn:

$$R \propto \frac{1}{\sqrt{N}}$$

Eq. 2-12

It shows that in order to halve the relative error the total number of initial histories, *N*, in the simulation must be quadrupled.

2.3.3. Particle transport

In particle transport, an analog Monte Carlo game is the direct simulation process of particle's life events [19]. An analog Monte Carlo simulation follows each particle individually in a system according to their probability distributions until all source histories are terminated. When describing a particle transport problem a source has to be specified; the initial position, energy, and direction of flight coordinates are determined for each history following their probability density function. Then, sampling the probability density function of the path length (dependent on the cross section of the medium) determines distance to the next collision. Once the particle reaches the collision site, several events

(scattering, multiplicative, or absorption) can take place depending on the target nuclei. If no absorption occurs and the particle is scattered, it is assigned a new set of energy and flight direction coordinates according to their distribution function. Alternatively, for a multiplicative event (e.g., (n, 2n) reactions) or if additional source terms are created (e.g., (n, γ) reactions), parameters of the new particles are selected and stored to be followed after the primary particle is terminated. This process is repeated until an absorption takes place, the particle leaves the system (with no possibility of scattering back), or its energy falls below the range of interest. During the course of a simulation, if a response is desired at a specific location, the sum of the contributions (for each source history) is tallied (i.e., collected) at the location. Finally, in order to estimate the physical quantity of interest, the average of a sufficient large number of these scores is then calculated.

The Monte Carlo method has two major advantages over the Discrete Ordinates approach. One of them is the possibility of detailed modeling for complex geometries (unlike the mesh structure required for Discrete Ordinates). The other one is the continuous energy treatment in particle interaction cross sections that leads to more accurate results. However, since Monte Carlo results are given as approximations with their associated statistical errors, a large number of simulated particles are necessary to minimize these errors. Increasing the number of sampled particles comes hand in hand with long computer running times (as seen in the previous section); which especially become prohibitive in deep penetration shielding problems (i.e., with a strong flux attenuation) or large geometries.

2.3.4. Variance reduction

For an analog Monte Carlo game in particle transport, as stated previously, events are sampled following the natural probability functions of the physical process. However, in these real experiments, millions of source particles are emitted and only a small fraction are likely to reach the detector; thus, making it not very effective in most of the geometries. Reducing the computer time by decreasing source particles results in worst statistics and less reliable results; nonetheless, one of the advantages of following particles individually is the feasibility to easily run simulations using parallel processing. In these computer runs, tasks are distributed in separate groups of independent trajectories between different computer nodes, hence decreasing the total computational time considerably. Although in some circumstances parallel processing may not be enough, and computational effort needs to be further reduced.

Non-analog Monte Carlo runs reduce the calculation time substantially. These simulations modify sampling without altering the particle density; the contribution to the score of the event (i.e., *weight*) must be adjusted in order to do so. In particle transport, weight can be interpreted as the number of physical particles represented by each simulated track. Note that the expected mean value of a response function must be the same in both analog and non-analog games. Additionally, it must be kept in mind that the variance reduction techniques in Monte Carlo non-analog games will reduce computer time to accomplish sufficient precision of the calculations (not accuracy).

The main goal of variance reduction methods is to reduce the relative error of a calculation. To achieve this, they direct the computational effort to focus on particles

relevant to the response function by modifying the natural probability distributions. Nonetheless, to maintain an unbiased score the statistical weight must be adjusted following the equality [20]:

$$w_{biased}\, f(x)_{biased} = w_{unbiased} f(x)_{unbiased}$$

Eq. 2-13

Where *f(x)* is again the probability distribution used in the sampling and *w* is the particle weight. The main challenge of applying variance reduction techniques is choosing the problem dependent parameters in the biased terms (i.e., $f(x)_{biased}$).

When applying variance reduction techniques, the user must keep in mind that some of them can interfere with each other and that, depending on the problem, some methods are more appropriate than others. The variance reduction techniques in non-analog Monte Carlo games can be separated into four classes [18]:

- ***Truncation methods*** cutoff parts not significant to the tally in the phase-space, by not modeling them. These include *geometry truncation* and *time* and *energy cut-off*.
- ***Population control methods*** adjust sampling according to importance in the phase-space. *Weight cut-off*, or *Splitting*/*rouletting* is done accordingly.
- ***Modified sampling methods*** make use of distributions, other than the natural probability density function, in order to "send" histories to the desired regions in the phase-space.
- ***Partially-deterministic methods*** avoid normal random walks using deterministic-like techniques.

In this work population control techniques are used, therefore a more extended review of two of them (*geometry splitting with Russian roulette* and *weight windows*) is presented next. One modified sampling method (*implicit capture*) will also be discussed, since in the Monte Carlo code used for the calculations (MCNP) is set at default.

2.3.4.1. Geometry splitting with Russian roulette

Individual sampling of histories in a neutron transport problem is the main advantage of the Monte Carlo method; however, computer time can be wasted following particles that do not contribute to the desired tally. The concept of importance in the splitting/roulette technique must be clarified before explaining the method. Importance can be defined as proportional to the estimated value that particles in a cell have to the specified response function. It is assigned by the user, based on their judgment, throughout the geometry. Namely, if a region is considered to contribute poorly to the desired tally, a low importance can be designated in order to follow few histories with a higher weight instead of multiple particles having a fraction of that weight. Conversely, a higher importance can be assigned in areas expected to have a higher contribution to the tally or on highly absorbent materials (that will likely terminate most of the histories but nonetheless want to be sampled), so that more track lengths can be sampled towards the scoring region; in this case more particles are followed with less statistical weight. This can be used to increase computer efficiency by controlling the population according to its importance. However, the user may not know in advance which areas of the geometry will be likely to contribute more to the tally, and only after the problem is solved can these be properly defined. The user expertise is crucial when determining importance regions efficiently; since if they are

not correctly defined the outcome will turn out to be the opposite as desired, and computer time may be increased unnecessarily or important paths will be neglected in the sampling. Usually, knowledge of similar problems or information from analog runs is a good starting point when dealing with importance regions.

The *geometry splitting/Russian roulette* game increases the particle population in important regions and truncates histories in locations of low importance. In order to do so, the space region is divided into cells with an assigned importance according to the score contribution. A particle entering a region with a designated lower importance (than where it came from) will be rouletted, whereas if the importance is larger it will be split. Weight has to be conserved throughout the process, so a particle with an initial weight w_0 in a region of importance I_0 that enters a cell with lower importance I_1 ($I_0 > I_1$) is rouletted, and it will either be followed with a probability I_1/I_0 and a new survival weight of $w_1 = w_0 \cdot I_0/I_1$ or terminated with a probability $1 - I_1/I_0$. If the history enters a high importance region, with I_2 being $I_0<I_2$, the particle will be split into $v=I_2/I_0$ histories each having a new weight of $w_2 = w_0/v$. Given the case that v is not an integer, the most common outcome is the expected value splitting [20]. In this approach, where $n < v = I_2/I_0 < n+1$, particles will be split with a resulting weight of $w_2=w_0/v$, and the number of produced histories will be n with probability $q(n)=n+1-v$ or $n+1$ particles with probability $q(n+1)=v+n$.

Splitting in high importance regions increases the information collected per history by creating more than one possible event. This reduces the variance but will also increase the computer time; accordingly, a balance must be found so that enough information is collected and the extra computer time becomes advantageous. Rouletting, on the other hand, terminates particles not collecting enough information, increasing thus the variance

but saving computer time in favor of sampling more important regions. Nonetheless, killing histories can be counterproductive if information is lost and important paths are not adequately sampled. Russian roulette and splitting procedures can also be applied in the same manner to energy importance ranges.

2.3.4.2. Weight windows

In complex geometries a region-wise splitting/rouletting technique may facilitate transport calculations. Being able to split or roulette the particles depending on the region, by dividing the system into cells and assigning specific importances, can lead to a smooth weight distribution throughout the geometry as long as the region importances have been designated properly. Computer-wise, splitting or rouletting every history moving from one cell to another is costly and the improvement in the score may not be enhanced significantly. With the weight windows technique not all particles are altered, as those with a weight close to the optimum value are not modified; this is done by defining intervals in which the history entering a region may be split, rouletted, or left unchanged.

The first step when applying weight windows is to divide the geometry into different regions. Once these regions are defined, each phase-space cell is delimited according to their importance. Three parameters must be given: a lower and an upper weight window threshold (w_L and w_U respectively), and a survival weight (w_S) within the window for the surviving rouletted histories. Note that in the computer codes only a lower bound must be assigned and the upper and survival weights will be defined as multiples of this minimum weight. A particle entering a cell with a weight below the lower bound will be rouletted, and it will either be terminated or followed, with survival probability $w/w_{S,}$

and a survival weight, w_S, within the window. Alternatively, if the weight of the history is above the upper bound, it will be split by the minimum integer k such that $w_L \leq \frac{w}{k} \leq w_U$, so all the resulting particles are also within the windows thresholds [21]. This technique is summarized in Figure 2-2.

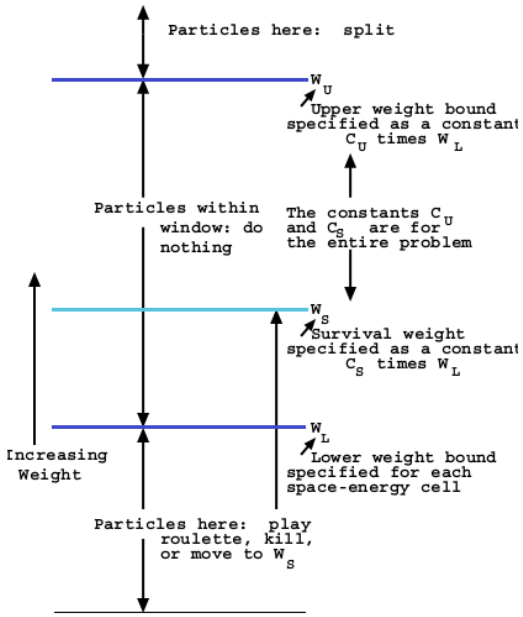

Figure 2-2 Weight windows technique in a Monte Carlo simulation [18]

The geometry splitting/Russian roulette techniques presented in the previous section and weight windows have several differences that must be acknowledged [18]:

- The weight window can be space-energy or space-time dependent, whereas geometry splitting/roulette is only space dependent.
- Weight windows evaluate the particle weight before taking any action, while geometry splitting/roulette is performed regardless of weight.

- Weight windows take into account absolute weight bounds and geometry splitting/roulette is done on the ratios of importances.
- The actions taken by weight windows can be applied at surfaces, collision sites, or both. Geometry splitting/roulette is only performed at surfaces.
- Weight windows require histories weights to be within the defined bounds, thus controlling weight fluctuations that may be introduced by other biasing techniques.
- The weight windows can be turned off in selected regions of the phase-space.

Some Monte Carlo codes have implemented, aside from the weight windows technique, a tool to assist in the window boundaries allocation. This will be discussed in section 2.4.2 for the Monte Carlo code used in this work.

2.3.4.3. Implicit capture

Analog Monte Carlo runs are terminated when all particles are absorbed, have abandoned the system with no possibility of returning, or their energy decreases below a region of interest. Absorption and leakage from the system can be prevented by statistical weight reduction; although most computer codes will only prevent absorption due to the increase of computer time the use of both would entail, lowering the efficiency of the calculations. For this reason, only absorption by weight reduction (or *implicit capture*) will be presented here. In this technique a particle that following the *i-th* interaction should be

absorbed, will instead be followed with a survival weight that has properly been reduced following the relation [19]:

$$w_i = w'_i \frac{\sigma_{total} - \sigma_a}{\sigma_{total}}$$

Eq. 2-14

where w'_i is the weight before the *i-th* interaction, σ_{total} is the total microscopic cross section for the collision nuclide, and σ_a is the nuclide microscopic absorption cross section. The main advantage of this game is to prevent a history from being absorbed right after reaching the tally region, before having scored. Note that, as in the splitting technique, this method reduces the variance but will also increase computer time per history.

2.4. Monte Carlo N-Particle Transport Code- MCNP

The Monte Carlo N-Particle (MCNP) Transport Code [18] is one of the most widely used software packages in radiation transport. It includes many helpful features like a flexible tally structure (some of them are: surface current or flux, volume flux, or particle heating), several variance reduction techniques, or an extensive collection of cross-section data. Accordingly, the MCNP code has a wide variety of applications such as dosimetry and radiation studies, radiation shielding, fission and fusion reactor design, medical physics, or detector design and analysis, amongst others. Even though MCNP is a powerful transport code, its full potential is limited by the available computational resources.

However, as computer power increases, the use of Monte Carlo based codes such as MCNP turns more accessible as its efficiency expands.

The input of a transport calculation using the MCNP code must include the geometry description, materials description with cross-section data library specifier ID, source description, and the type of desired tallies. Other features may be incorporated as well, such as variance reduction techniques. For the geometry description, one of Monte Carlo's biggest assets is having the possibility to use detailed systems; for this purpose complex systems may be modelled using a CAD program that can subsequently be converted to the appropriate MCNP format with existing tools such as MCAM [22]. Concerning tallies, the mesh tally is a new feature depicted in the MCNP5 version, which will be used for this work. It is a track-length type estimator available using the *FMESH* card. This feature allows tallying over any desired region of the geometry with the use of a superimposed mesh. As a result, an output file (*meshtal*) will be generated with the estimates of the flux and their statistical errors.

Every MCNP run generates an output file in which the calculations are summarized. This file must be examined closely in order to ensure that a proper sampling has been done and all estimations converge. This is especially important when using variance reduction techniques, since they could be interfering with one another or simply not improving the efficiency. To address this problem, the figure of merit (FOM) in MCNP is an indicator of the calculations efficiency for a given tally. It can be defined as [18]:

$$FOM \equiv \frac{1}{R^2 T}$$

Eq. 2-15

where T is the time required to perform the simulation and R is the relative error of the tally (as described in section 2.3.2). To compare the efficiency in different runs, it is straightforward to see that a larger value in the FOM implies a more efficient calculation. Concerning tally reliability, the MCNP output provides a fluctuation chart in which the value of the FOM throughout the calculation is presented. Since R^2 is proportional to $1/N$, a well behaved tally must have an approximately constant FOM as N increases. Checking this behavior is useful when trying to properly sample less probable events. In this case, the FOM will abruptly decrease as a result of a rare path significantly affecting the tally, and the sampling must be examined since the confidence intervals may not be correct. The MCNP output files should carefully be inspected for this and other issues that may arise during the simulation process. If a simulation has correctly ended, the relative error of the selected tallies has to be checked. Results of at least 0.1 are considered reliable for all tallies except point detectors, which must have a relative error of 0.05 or less.

Weight windows (WW) is the variance reduction technique used in this work. Therefore, its implementation in the MCNP code is presented next. The Weight Windows Generator is an MCNP tool used to assist in the thresholds assigned to the windows, and is discussed in the following section.

2.4.1. Weight Windows in the MCNP code

In the MCNP code, the weight windows game can be played over the defined geometry cells or in the voxels of a superimposed mesh. The later procedure is the best choice when dealing with intricate geometries, as the voxels can be adjusted to the areas of interest following the user's judgment. In order to set mesh-based window thresholds,

MCNP requires an input file (*wwinp*) in which the mesh bounds are indicated (in cylindrical or Cartesian coordinates), the lower limits are specified, and, if applicable, the energy bounds. The windows upper limits as well as the survival weight for the rouletted histories are given in the *WWP* card as a multiple of the lower bound. In this card other settings, such as where the weight will be checked (at collisions, surfaces, or both) or the maximum number of weight windows splits per event, can also be indicated. Where the lower bounds are to be taken must also be specified here (external *wwinp* file, *WWINi* cards, or *IMP* cards).

The main advantage of using weight windows is diminishing the weight fluctuations within the phase-space. Additionally, the weight window bounds allow a large range of optimal values; and making them inversely proportional to the importance function is one of the most common choices. The Weight Windows Generator is an MCNP tool that can be used to assist in the window boundaries allocation; it is discussed in the following section.

2.4.2. The Weight Windows Generator

In the MCNP code, a Weight Windows Generator (WWG) is available in order to assist in defining the lower bounds assigned to weight windows. The technique followed by the WWG was developed by Booth and Hendricks in 1984 [23]. This generator defines the thresholds based on the importance obtained in a simulation, making them inversely proportional to the importances achieved in each cell or voxel (in case a superimposed mesh is used). The output obtained is a weight map that can be subsequently used as a weight windows input.

The WWG is associated with a specific tally. In the description card, a tally must be related to the generator in order to optimize scores; and importances will be obtained related to this tally estimating an average adjoint flux in a forward calculation, (with reference to particle transport, note that MCNP allows adjoint flux calculations, but it must be kept in mind that this is done only with a multigroup energy approach). The key point is that the WWG is locally oriented, and regions away from the targeted tally will be treated as such.

Importance in the WWG context must be discussed. For the splitting/roulette game, importance is set based on the user's judgment and knowledge of the geometry, so that the number of sampled particles in a region is proportional to its contribution to the tally of interest. Whereas for the WWG tool, it is quantified by MCNP from a previous simulation; where the importance of a particle in a point of the phase-space is set equal to the expected score that a unit weight history will generate. After dividing the system into a number of regions a cell's importance can be estimated as [18]:

$$Importance = \frac{total\ score, from\ particles\ and\ progeny, entering\ the\ cell}{total\ weight\ entering\ the\ cell}$$

Note that the total score cannot be known until the simulation is finished and the cell has properly been sampled. In Monte Carlo runs, an initial approximation is needed for the importance and, ideally, iterative procedures will subsequently lead to more precise results.

It must be mentioned that the size of the cells in a mesh-based weight map play an essential role when sampling in search of the importances. Big cells will not be

representative of the different regions for complex geometries, and excessively small ones will not be properly sampled unless a large number of histories are used. The user must be able to properly divide the geometry, according to each specific system, in order to get reliable results using weight windows.

A limitation of the WWG is that, since the importance is dependent on the score in each cell, some areas may not have been sampled properly creating unreliable results. Two main approaches can be taken to overcome this difficulty. One of them is to reduce the density of all the materials in the system to a fraction of their value. If the density is reduced to a fraction, the particles mean free path will be higher and longer distances can be travelled by them without interactions. This way, all regions of the phase-space should have enough history tracks to create an optimal weight map that may be used in a further run with the real density. The other approach is to make an iterating process. If an iteration process is started; several runs have to be made using the newly generated weight maps each time, until an optimal importance function is found. The first estimates of this process come from an analog run, whereas the next iterations will make use of the created weight maps until all particles are transported through the region of interest. Whether density is reduced or an iterating process is carried out, each approach has their advantages and disadvantages. Reducing the density will prevent iterations saving computer time but, for complex geometries with a large amount of cells, this can be a tedious task. On the other hand, iterations may take up a larger amount of computer time, but there is no need to change the rest of the input file.

One of the biggest issues that may arise from the use of weight windows is the appearance of large gradients within mesh cells. To warn the user of this situation, for a

cell-based weight windows game, MCNP flags cells that are more than a factor of 4 different from their adjacent regions [18]. The outcome of two contiguous windows with a significant difference in their boundaries is the occurrence of oversplitting histories. Due to MCNP banking histories until other tracks are terminated, this increases computer time to a point that may not be acceptable. Consequently, cautiousness is recommended when using the mesh-based generator.

3. Global variance reduction techniques

3.1. The necessity of a global variance reduction technique

Throughout the life of the future ITER reactor, maintenance and hands-on work in the facility must be carried out safely. For this reason, proper assessment of dose rates throughout the reactor building is one of the main targets concerning its design. The inclusion of penetrations in the shields to host electrical, diagnostics, or other systems, diminishes their full attenuation potential. In fact, streaming of particles through these gaps during operation will cause most of the radiation damage; and correctly characterizing these geometries, requires a thorough particle transport. Depending on the location, different SDR limits are settled at several times of interest; where personnel is expected to have access, assuring occupational safety regulated by the authorities to minimize the workers exposure to radiation (for the ITER reactor the limits to be accomplished are specified in [24]).

Radiation transport calculations with proper sampling are required for the correct evaluation of response functions such as prompt or delayed dose rate, decay heat, or activity, amongst others. Variance reduction techniques aid in this task by strategically sampling more often the histories that have a larger contribution to the desired tally. However, in systems where the desired response functions are not necessarily limited to a small region of the phase-space, tallying in several detectors, large regions, or even the entire reactor is needed. The implemented variance reduction techniques in MCNP are not useful for this purpose; since they are locally oriented. Additionally, tallying large

geometries (with highly absorbent materials and large regions of interest) make it extremely computationally expensive to populate all these regions of interest with enough neutrons to reach sufficient accuracy. Thus, optimizing transport, to obtain estimates through the entire phase-space or at multiple detectors, requires the use of global variance reduction (GVR) techniques to minimize computational effort and avoid prohibitive computing times.

In order to comply with the established dose limits after a nuclear reactor shutdown, identification of the SDR in large regions and throughout the entire system is needed. Two methodologies are commonly used to calculate the SDR in fusion facilities. The rigorous-two-step (R2S) methodology is a well-known procedure in which three calculations are coupled. First, neutrons from the source have to be transported to the region/s of interest. Second, activation of the materials by these neutrons creates gamma sources (which are responsible for the dose) that must be defined. Lastly, the decay gamma transport calculations are performed to calculate the desired response. The R2S tool couples a transport code to an activation code in order to activate materials and obtain a photon source. Further insight into the R2S methodology will be given in the chapter dedicated to SDR calculations (5.2). In contrast to the R2S technique, the Direct-One-Step (D1S) methodology calculates the SDR in one single Monte Carlo run [25]. The D1S method transports decay photons in the same transport calculation as the neutrons; to achieve this, nuclear data is modified and the decay gammas are included in the reactions in which they will be produced. An activation code is commonly used to determine correction factors regarding the irradiation scenario, cooling time, as well as the nuclide and reactions. The principal advantages of the D1S method over the R2S approach are the speed of calculations (due to the single Monte Carlo run needed) and the spatial and energetic

resolutions (since the decay gammas are produced at the same location and at the energy in which the neutrons interact). However, due to only taking into account direct production photons, the D1S approach will not be suitable for problems with intense neutron fluxes and long irradiation times [25].

Independently of the methodology used for calculations of the SDR, precise neutron transport is required to properly generate the gamma sources that are responsible for the dose. In the previous chapter an overview of the Monte Carlo method applied to particle transport was presented. For non-analog Monte Carlo games several variance reduction techniques were also introduced. In these techniques, optimization for defined response functions is obtained by favoring sampling through regions of interest that are more likely to contribute to the specified tally over regions of less importance. However, tallying over an entire geometry requires a GVR technique to efficiently transport particles through the complete model. In this chapter, an overview of the existing GVR techniques for MCNP is given, weak aspects of them are outlined, and, over an existing method, optimization and correcting of some of its issues is presented in order to improve neutron transport through a fusion reactor.

3.2. State of the art

In this section, existing GVR techniques are outlined. First, four hybrid methods are presented; which combine deterministic methods with Monte Carlo sampling. Next, two purely stochastic methods are shown.

3.2.1. Hybrid GVR methods

Hybrid GVR techniques rely on the complementarity of the Monte Carlo and Discrete Ordinate methods. As stated before, a Monte Carlo simulation has the advantage of addressing detailed complex geometries. However, it becomes computationally prohibitive when sampling large systems or deep penetration problems that require a large amount of source particles. On the other hand, Discrete Ordinates methods are faster, but their accuracy depends on the phase-space discretization resolution; which may also become too computationally expensive for an extensive resolution. The main idea behind hybrid GVR techniques is the coupling of both methods, to increase overall efficiency in particle transport. This is done by using deterministic codes to obtain information (e.g., create importance maps) and distribute particles effectively through the Monte Carlo phase space. The four GVR techniques presented next are the most well-known hybrid methods.

3.2.1.1. The Cooper and Larsen method

Making use of the MCNP WW feature to uniformly distribute particles through a system, Cooper and Larsen [26] made one of the first approaches to hybrid GVR. This was achieved by developing weight maps proportional to deterministically obtained forward flux estimates. In their procedure, the premise was that if the Monte Carlo particle density, $m(\vec{r})$, was set constant throughout the windows, the calculation would present uniform statistical errors for all the cell tallies. To keep the Monte Carlo particle density constant, weight windows should be proportional to the physical particle density. Monte Carlo particle density is related to the physical particle density, $n(\vec{r})$, by the average particle weight through: $n(\vec{r}) = \overline{w}(\vec{r}) \cdot m(\vec{r})$. On the other hand, considering the relation

between particle flux and physical particle density: $\Psi(\vec{r}) = n(\vec{r}) \cdot v(\vec{r})$, (where $v(\vec{r})$ is the particle velocity) and keeping in mind that the goal is to set Monte Carlo particle density constant:

For $m{\sim}constant \rightarrow n \propto \overline{w}\ and\ \Psi \propto \overline{w} \cdot\ v$

This space-only method sets the center of the weight windows proportional to $n(\vec{r})$ or the forward scalar flux, $\Psi(\vec{r})$, (which is proportional to $n(\vec{r})$): $\overline{w}(\vec{r}) = \Psi(\vec{r})/\max(\Psi(\vec{r}))$. Eventually, whenever the geometry of the system became more complex, this method was found to be insufficient and, later, two modifications that included energy-dependent flux were presented (see 3.2.1.3).

3.2.1.2. The CADIS and FW-CADIS methods

In 1998 Wagner and Haghighat created the Consistent Adjoint Driven Importance Sampling (CADIS) method [27]. Even though this is a local variance reduction technique, it will be discussed first to further understand the Forward Weighted CADIS (FW-CADIS) global method. The CADIS technique is based on the physical interpretation that the solution to the adjoint Boltzmann transport equation is a measure of the importance (i.e., expected contribution) of a particle to a response function. Therefore, it uses a previous adjoint calculation (usually using a Discrete Ordinates code) to bias the source and construct an importance map that will be used as a WW input for a Monte Carlo simulation. The biased source ensures source particles are started in proportion to their expected

contribution to the tally; whereas the WW bias the transport by splitting or rouletting particles according to the importance of regions in the phase-space.

These parameters (source biasing and importance maps) are obtained from the previous deterministic run. In this calculation, the adjoint source is defined as the detector response at some location (i.e., with similar space and energy distributions). Once the adjoint function is determined, $\Psi^{+}(P)$, in the phase-space P, source biasing for the Monte Carlo sampling is specified. The biased probability density function of the source ($\hat{q}(P)$) is defined as the ratio between the detector response from phase-space P and the total detector response [27]:

$$\hat{q}(P) \equiv \frac{Detector\ response\ from\ phase-space\ P}{Total\ detector\ response} = \frac{\Psi^{+}(P)q(P)}{\int_P \Psi^{+}(P)q(P)dP} = \frac{\Psi^{+}(P)q(P)}{R}$$

where $q(P)$ is the source of the forward calculation and R is the total detector response. This way, source particles are biased according to their contribution to the detector response. Note that this is a biased probability function and weight must be corrected according to Eq. 2-13, now having [27]:

$$w(P)\hat{q}(P) = w_0 q(P) \rightarrow w(P) = \frac{R}{\Psi^{+}(P)}$$

where $w(P)$ is the statistical corrected weight and $w_0(P)$ is the unbiased weight (which is set equal to 1). Regarding transport biasing via importance maps, the WW tool is used in the Monte Carlo simulation. In this case, the thresholds of the mesh cells are determined so that the statistical weights $w(P)$ are located at the center of the window. Therefore, using

the relation: $\beta = \frac{w_u}{w_l}$, between upper (w_u) and lower (w_l) thresholds of the windows; space- and energy-dependent WW lower bounds are given by [27]:

$$w_l(r, E) = \frac{w(P)}{\left(\frac{\beta + 1}{2}\right)}$$

In the CADIS method, source particles from the biased distribution will start within the WW limits. This consistency prevents source particles to be split or rouletted as soon as they are born, so no decrease of the computational efficiency occurs. The CADIS automated method has been implemented into the A^{3}MCNP, ADVANTAG, and MAVRVIC codes [28] [29] [30].

As stated previously, the CADIS method is locally oriented. In 2007 an extension of the CADIS technique was presented, considering large extensions in need of tallying. The Forward Weighted CADIS (FW-CADIS) was developed by Wagner, Blakeman, and Peplow; and has since become the reference method in GVR techniques for particle transport [31]. Its main goal is to achieve uniformly low statistical uncertainty by uniformly distributing Monte Carlo particles through the system. This is accomplished by modifying the local CADIS method to incorporate a forward flux estimate into the definition of the adjoint source.

In the FW-CADIS methodology, an initial forward deterministic calculation is performed and the results are used to define the adjoint source, which is weighted by the

inverse of the forward flux in the phase-space regions where tallies are desired. To do this, first consider the response function in terms of the forward flux [32]:

$$R = \int_P \Psi\,(P) f(P) dP$$

Eq. 3-1

Where $f(P)$ is an objective function that, in this case, needs to be defined as some function that converts flux to Monte Carlo particle density. Using again the relation between Monte Carlo particle density, $m(P)$, and the physical particle density: $n(P) = \overline{w}(P) \cdot m(P)$; and the relation between the particle flux with the real particle density: $\Psi(P) = n(P) \cdot v(P)$. We now have:

$$m(P) = \frac{n(P)}{\overline{w}(P)} = \frac{\Psi(P)}{\overline{w}(P) v(P)} = \Psi(P) f(P)$$

and the total response, given by Eq. 3-1, may be written as:

$$R = \int_P \Psi\,(P) \frac{1}{\overline{w}(P) v(P)} dP \rightarrow \left\{ \begin{array}{c} \text{Using Cooper and Larsen's} \\ \text{premise, that:} \\ \text{for } m \sim constant \rightarrow \\ n \propto \overline{w}\ and\ \Psi' \propto \overline{w} \cdot\ v \end{array} \right\} \rightarrow R = \int_P \Psi\,(P) \frac{1}{\Psi'(P)} dP$$

Eq. 3-2

where the adjoint source is defined as the objective function $f(P)$:

$$q^+(P) = \frac{1}{\Psi'(P)}$$

Note that this weights the adjoint source with the inverse of the forward flux; thus the adjoint source will be high where the forward flux is low; and, on the contrary, if the adjoint source is low, the forward flux will be high. For response functions other than the

particle flux, the adjoint source is weighted with the forward solution. For instance, if the desired response function is given by $\sigma_d(P) = \sigma_d(\vec{r}, E, \widehat{\Omega})$ (e.g., dose rate), the adjoint source is defined so the individual contributions of the total response function are uniform [32]:

$$q^+(\vec{r}, E, \widehat{\Omega}) = \frac{\sigma_d(\vec{r}, E, \widehat{\Omega})}{\int_E \int_{4\pi} \sigma_d(\vec{r}, E', \widehat{\Omega}')\Psi(\vec{r}, E', \widehat{\Omega}')dE'd\widehat{\Omega}'}$$

Once the adjoint source is defined, an adjoint deterministic simulation is performed to calculate the Monte Carlo source and transport biasing parameters using the standard CADIS approach [31] [32]. The FW-CADIS method is a reliable and efficient hybrid technique for GVR problems [33] [34] [35] and has been used, amongst others, in ITER calculations [36] [37] [38].

3.2.1.3. The Becker and Larsen method

Two premises for obtaining the global flux considering energy dependency, derived from Cooper's methodology, were presented by Becker and Larsen in 2009 [39]. The first approach, the global flux weight windows (GFWW), is a space-energy review of Cooper's version [26]; where the weight windows, $\overline{w}(\vec{r}, E)$, are also set proportional to the forward scalar flux: $\overline{w}(\vec{r}, E) \propto \Psi(\vec{r}, E)$. The second approach, the global response weight windows (GRWW), considers dose or other energy integrated responses are targeted throughout the entire phase-space. The weight windows limits are now set as:

$$\overline{w}(\vec{r}, E) \propto \frac{R(\vec{r})}{f(E)}$$

where $f(E)$ is the response function, and $R(\vec{r})$ is the energy integrated response (see Eq. 3-1). In [35] the GRWW method was compared to other GVR techniques and has been shown to perform fairly.

3.2.1.4. The Multi-Step CADIS method

Another modification over the CADIS methodology, the Multi-Step CADIS (MS-CADIS) technique, was introduced in 2013 by Ibrahim, Peplow, and Grove, and is aimed at accelerating Monte Carlo neutron transport calculations of the R2S. It uses an importance function representing the importance of the neutrons to the final SDR [40]. In this approach, the solution of the adjoint neutron problem is used to bias the Monte Carlo simulation according to the production rates of the radioisotopes with higher importance to the SDR, due to the location and their decay spectra. The MS-CADIS functionality has been tested using the ITER benchmark problem with promising results and is currently about to be implemented in the SCALE and ADVANTAG codes [41].

3.2.2. Purely stochastic GVR methods

Aside from the GVR hybrid methods previously described, two purely stochastic techniques will be introduced here. These methods have the advantage of not needing a deterministic code to define importance maps. However, creating these maps usually takes longer computational time than the hybrid techniques. Nonetheless, for systems that don't have major changes in the geometry, an importance weight map only has to be created once.

3.2.2.1. The MAGIC method

The Method of Automatic Generation of Importances by Calculation (MAGIC) was developed by Davis and Turner in 2011 [42] [43]. In this technique (also based on Cooper and Larsen's idea), the flux, population, or weight (from MCNP calculations) is used to generate weight windows (cell or mesh based) or a cell-based importance map. An analog simulation must be done first to start iterations that will consecutively lead to a more adjusted map. Multigroup data or energy truncations may also be used in order to accelerate transport simulation during the iteration process. Several approaches can be taken in this method: cell-based weight windows map (MWIC), mesh-based weight windows map (MWIM), or a cell-based importance map (PDIC).

Comparison of the MWIC, MWIM, and PDIC estimations against the FW-CADIS technique were made using an ITER model, proving that the MWIM method outperforms the rest in terms of FOM for the same computer time. However, the long history issue (oversplitting) still prevailed when weight windows was used. In 2013 this problem was solved by renormalizing a window every time a history with a weight over *M* times the threshold entered a cell or voxel [44]. Studies on a spherical test case showed that, with the long history mitigation, parallel efficiency improved considerably although for high values of M ($M \geq 10^5$) improvement of the efficiency reverted, as if the mitigation was not considered. On the other hand, for overly low values of *M*, statistical uncertainty increased. However, as with all variance reduction parameters, optimization is dependent on geometry and further studies in the A-lite model [45] are also shown. In this case, for $M \leq 10^4$ efficiency was poor, being 10^5-10^6 the most optimal value range for *M*. Nonetheless, as

with the FW-CADIS technique, the MAGIC method is also currently being used for ITER calculations [46] [47].

3.2.2.2. Van Wijk's method

Van Wijk, van den Eynde, and Hoogemboom proposed in 2011 a method, solely based on Monte Carlo calculations, to uniformly distribute particle density through large geometries [48]. The main approach of the procedure was based on Cooper and Larsen's idea of using the forward scalar flux to set weight windows limits [26]. Starting on the premise that particles will be born at locations with the highest flux and lower error, windows can be normalized to these values according to equations:

$$W_{th,Re_i} = \left(\frac{\beta+1}{2}\right)^{-1} \frac{Min(\overrightarrow{Re})}{Re_i}$$

Eq. 3-3

$$W_{th,\emptyset_i} = \left(\frac{\beta+1}{2}\right)^{-1} \frac{\emptyset_i}{Max(\vec{\emptyset})}$$

Eq. 3-4

where β is the ratio between the lower and upper thresholds in the windows ($\beta = w_U/w_L$), $\overrightarrow{Re}$ and $\vec{\emptyset}$ are the vectors with data of all the mesh voxels, and i represents the desired mesh cell location. An iterative procedure is necessary in order to adjust windows thresholds until the entire map is optimized. The first simulation is an analog Monte Carlo run, in which the *meshtal* (the generated MCNP output file with the flux estimates and their statistical errors, see 2.4) results are processed and a *wwinp* (the WW input file, see 2.4.1) file is created. This *wwinp* file will subsequently be used for a non-analog run that, in turn, returns a more thorough *meshtal*. Repeating this process until all the geometry is covered, will eventually result in an optimized weight map that can be used for a final simulation. Note that if the

forward flux is obtained via deterministic estimates (instead of Monte Carlo iterations) the flux-based method is the same as Cooper and Larsen's technique. The work in this dissertation is based on vanWijk's approach; therefore, a deeper insight of its application is given in the following sections.

3.3. Examination of van Wijk's methodology

In this section a more thorough view of van Wijk's technique is first described. Outcomes and issues showing up from its application are later discussed; with the first approaches that were taken to address them. Lastly, the modifications created to the algorithm that are applied in this dissertation are presented.

3.3.1. Detailed view of van Wijk's methodology

Before detailing the implementation of van Wijk's algorithms, the reasons to why this method was chosen in this work are pointed out. As explained in sections 1.4.3 and 1.4.4, the impact of neutrons released in fusion reactors has to be assessed during the design stages of the components. Due to the demanding specifications concerning radiation damage, calculations of accurate response functions through the large geometry of the reactors are extremely expensive computer-wise; and GVR techniques to improve particle transport are needed. Additionally, as it will be explained in the next section, oversplitting issues inherent to the system design (like highly absorbent materials and gaps that cause neutron streaming) must be addressed for each GVR technique applied.

Due to the outstanding results obtained by Turner and Davis to avoid long histories within the weight windows in their MAGIC method (see 3.2.2.1), the simplicity of the Cooper and Larsen algorithm calls for a deeper insight using only stochastic calculations. Taking as a starting point van Wijk's methodology, other approaches to minimize oversplitting and improving neutron transport will be reviewed and compared in section 3.3.3. The main reason for taking this perspective is, aside from the simplicity of the algorithm, the convenience of creating reliable weight maps without the need of a deterministic code. When no deterministic code is available (or if the user is not familiar with its application) optimized weight maps, with minimum input from the user, can be created using an external script.

The first step taken in this study was to replicate van Wijk's algorithm creating a script written in Python [49]. As described in the previous section, the methodology defines WW thresholds of voxels (on a mesh covering the geometry) normalized with the highest flux or lower relative error from prior runs. An outline of van Wijk's procedure is shown in Figure 3-1.

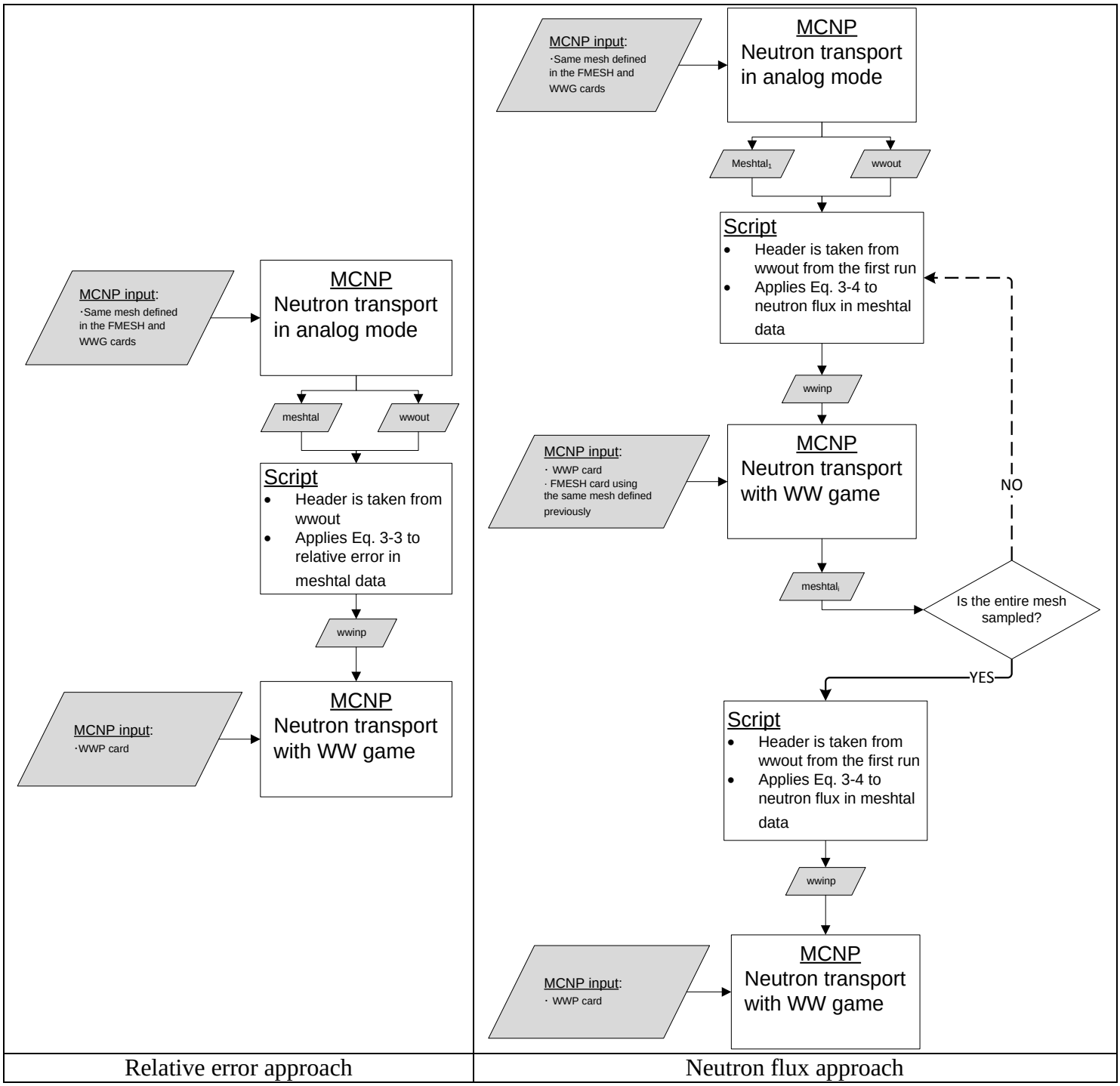

Figure 3-1 Algorithm for the van Wijk's GVR methodology

As seen in Figure 3-1, first, an analog with implicit capture simulation is run. In this simulation the WWG is set in order to obtain the *wwout* file that contains the header for the subsequent *wwinp* files that will be created (to include the windows lower thresholds of the mesh). Note that this header can also be defined manually if desired, or that this step can be done on its own, using only a few histories. A mesh tally, *FMESH* card (see 2.5), is also set using the same mesh coordinates as the ones included in the generator. This will provide the first flux or relative errors to be processed, using **Eq. 3-3** or **Eq. 3-4**, in the *meshtal* file. After applying the equations to obtain the *wwinp* weight map with the windows thresholds, a simulation using WW (with the *wwinp* file created) is run to obtain a more precise *meshtal* file. If using the flux based technique, iterations can be done in order to transport neutrons further into the geometry and to, in addition, improve the weight maps. Ultimately, a final simulation is run with a higher number of initial histories using the optimized weight map in the *wwinp* file.

By taking this approach, locations with a high flux (or lower relative error) will present windows with a higher threshold, thus increasing rouletting over the particles and reducing the number of histories by increasing weight; contrarily, the voxels presenting a lower flux (or higher relative error) will appear with a lower threshold that increases splitting, therefore increasing the particle density. The WW thresholds can be optimized through subsequent iteration until all the geometry, or large region of interest, is sampled. However, this is not the case when the map is built using the relative error approach **Eq. 3-3**. In this context, the relative error map created from the first run will not be improved by iterations; since the main goal, to equate all relative errors, is already accomplished after

the first adjustment. Results obtained by applying this technique are discussed in the next section.

3.3.2. Issues derived from applying van Wijk's methodology

In this section problems that show up using van Wijk's procedure are described and discussed as they would appear to a new user. As stated in the previous section, optimizing weight maps using the flux based method (using **Eq. 3-4**) is made through iterations, using a low number of initial histories, until all the geometry is covered.

To test the flux based approach, a simple geometry with a highly absorbent material was used. The system was defined as a 4 m long concrete block with a section of 1 m^2 with a directional plane source towards the concrete block. The source emits 14 MeV neutrons and is located at 0.5 m from the block; void was designated between the source and the concrete. WW was applied using a superimposed mesh that was defined over the system with 0.5 x 0.5 x 0.5 m^3 voxels.

Several cases were made using different initial histories for the iterations. In all the cases, the first issues appeared during transport in the iterative process, when approximately half of the concrete block was sampled. Specifically, after half of the voxels were sampled the computing time of next iteration increased by an order of magnitude. The reason of this sudden increase was the apparition of steep gradients within adjacent voxels inside the concrete. Namely, the iterative process transports neutrons inside the concrete block which rapidly absorbs them. At first, neutrons coming from the source penetrate into the block; and, even though the concrete is highly absorbent, the high number of neutrons reaching the block avoids steep gradients. However, as the neutrons reach further inside the concrete,

poorly sampled regions appear as a consequence of the attenuation of the neutron flux. Thus, low neutron flux cells result inside the material, close to higher flux regions. After processing the *meshtal*, to define the weight map containing the WW limits for the next iteration, the thresholds defined for mesh cells in the void and the regions closest to the source were several orders of magnitude higher than the limits defined inside the concrete, creating steep gradients within adjacent cells. The iteration performed using the resulting weight map, lead to long histories that increased computational time considerably. As van Wijk describes in his paper [48], one of the biggest problems regarding the flux based approach is the appearance of steep gradients within the cells thresholds that lead to long histories. Note that if instead of a mesh based WW game is played, and WW is defined over the cells in the MCNP geometry, the MCNP output flags the differences amongst adjacent cells limits when they happen to be over a factor of 4 (as explained in **2.4.2**). Therefore, if using WW with a superimposed mesh over a large system, localizing and renormalizing these problematic voxels "by hand" can be a complicated task.

The situation described above was tried to address by flagging voxels that passed from not having any statistics (particle flux and relative error equal to zero), to having a low sampling ("high relative error") from one iteration to the next, and readjusting their limits accordingly to the voxels with the higher flux surrounding them. First, what "high relative error" is considered to be has to be defined. In the test case run using the flux based approach, independently of the initial histories used, the highest average relative error for scoring voxels was found to be around 0.2; hence, as a reference, this value was doubled. In this modification to van Wijk's flux based technique, each *meshtal* was compared to the *meshtal* from the previous iteration. Voxels with a relative error over 0.4 which did not

score previously were flagged and groups of adjacent flagged voxels were created. The higher flux in the outer voxels belonging to each group would subsequently be compared to the higher flux found in their adjacent surrounding voxels. If the difference between the fluxes was found to be over a factor of 2, the entire group was assigned half of the higher flux found in the surrounding voxels. On the other hand, if no difference over a factor of 2 was found between the flux in the outer voxels of each group and the flux in surrounding voxels, the entire group was assigned the higher flux found within the outer voxels belonging to the group. In this approach, the flagged voxels are the ones containing highly absorbent materials that create the steep gradients, and renormalizing to the higher adjacent limits avoided oversplitting throughout the weight map creation process. Three observations where made after applying this modified procedure. First is that, in order to obtain the best optimization, once the entire geometry was sampled (i.e., all the voxels in the mesh had tallied), an additional iteration is necessary to properly adjust the thresholds assigned in the mesh. Second, an improvement (compared to the non-modified van Wijk's flux based method) in the total computational time invested in the creation of an optimized weight map was accomplished; this time was reduced by a factor of 4 or 5, depending on the initial histories used for the iterations. And lastly, it was observed that the total computer time needed to create a weight map was minimum using a lower number of initial histories (even though more iterations were needed). However, despite this approach worked well for deep penetration problems, the biggest issue did not arise from the map creation in simple shielding problems.

A larger problem shows up when small gaps are present in the geometry. When the modification previously described was tested using a more realistic geometry, oversplitting

issues reappeared. The procedure was tested using the ITER neutronics reference model (see 5.1.1). This model includes small gaps that create open paths from high to low flux regions (i.e., from the source to a region behind a shield). For this geometry, the main contribution in the hard to reach areas behind the gaps will come from particles streaming through the aperture, since these histories will have a significant higher weight than the rest which made it through the shield. During the process of creating the map, the probability of a particle entering the gap is relatively small (considering the low number of initial histories used to build the map), so at first oversplitting issues may not be evident. However, if a particle happens to enter the gap and the WW game is being played (in the iterative process or in the final run), this particle will undergo oversplitting as soon as it reaches a cell adjusted to low a flux (such as a region behind the shield). The steep gradient created by the high weight streaming particle reaching a low flux region is intrinsic to this type of geometry. Thus, in order to avoid long histories an overall (i.e., from the source to the further regions) smooth weight map has to be created.

The two approaches taken in this work to address the issues with long histories, for deep penetration problems and streaming particles, are described in the next section and analyzed in the next chapter.

3.3.3. Modifications to van Wijk's methodology

Two modifications, over van Wijk's technique, that create weight maps with minimum effort from the user's part are presented here. The first modification only addresses oversplitting issues in the flux based methodology; while the second modification, in addition to smoothing steep gradients for the flux based technique,

addresses the problem of particles not reaching the entire geometry if using the error based method.

The first approach taken in this dissertation avoids long histories that may arise by creating weight maps that show no steep gradients throughout the geometry. By taking the square or cubic root in **Eq. 3-4** weight maps created will be smoothed entirely from the source to the back of the geometry, avoiding the issues described in the previous section through map creation as well as with the final simulation. With this strategy, deep penetration problems while building the map through iterations are solved, since adjacent voxels will no longer show steep gradients in their thresholds. Streaming issues are also fixed for less frequent trajectories, because gradients that cause oversplitting in particles streaming through the gaps are also smoothed; hence, in the rare event a high weight particle reaches a far region of high density material, it will encounter a voxel with a limit showing less difference compared to their weight. However, there is a drawback to this procedure, since optimization is lost as the windows' limits differ from the real importance function. By taking roots over the estimated limits that enclose the average flux in each voxel, the windows are "pulled away" from this estimate in order to smooth the overall map. The less the windows differ from the appropriate value, the more optimized the map will be. Therefore taking square roots is more adequate than taking cubic roots. The algorithm followed by this approach is the same as van Wijk's described in Figure 3-1, but including a square root over **Eq. 3-4**.

The second approach is taken to avoid oversplitting in the flux based maps, but also taking into consideration the disadvantages of the relative error based maps. The biggest drawback using the van Wijk's error based technique is not having the availability of

improving through iterations; this leads to the necessity of sampling the entire model in the first run. When the geometry is sufficiently large, a high number of source histories will be necessary to obtain a thorough first sampling, and the computer time is increased accordingly. To overcome this issue, without having to start with a large number of source histories, densities of the materials can be reduced to a fraction of their value; thus avoiding heavy shielding materials from absorbing the particles before reaching all of the regions in the geometry. Note that this approach is also applicable to the flux based maps. By running the first simulation with material densities reduced, all the geometry can be sampled. Accordingly, the map created after applying **Eq. 3-3** or **Eq. 3-4** is thorough and sufficiently smooth to overcome issues that arise in deep penetration transport as well as with streaming. Oversplitting caused by streaming will still occur, since a gradient in the particle flux through the system will still prevail; however, it will not be as pronounced. The algorithm describing this procedure is outlined in Figure 3-2.

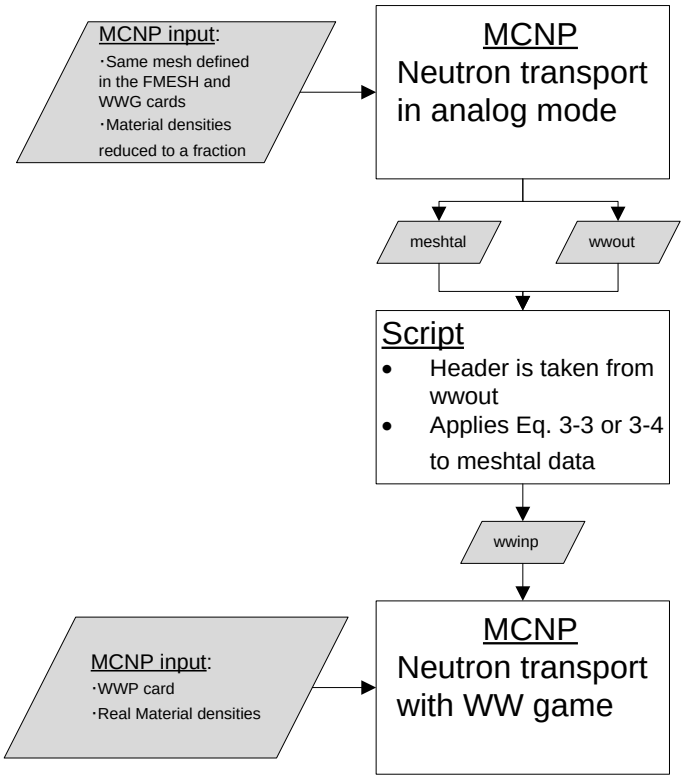

Figure 3-2 Algorithm for the density reduction GVR method

First, a simulation where density of the materials has been set to a fraction of its real value is run in analog (with default implicit capture mode). In the MCNP input, a mesh tally (*FMESH* card) is set and the WWG is turned on. Both of the described meshes in the generator and the mesh tally must have the same coordinates. As with van Wijk's method, the *wwout* file, produced by the generator, will provide the header for the created *wwinp* file. The *meshtal* file, resulting from the *FMESH* card, will be processed applying **Eq. 3-3** or **Eq. 3-4** to the relative errors or the particle flux, respectively, to define the thresholds for each voxel of the mesh, which are next written into their appropriate position in the *wwinp* file. Lastly, a final run can be performed, in which the materials densities are now set at their real value and in which the WW game is turned on using the defined thresholds in *wwinp*.

The only required input from the user, using either the square root or the reduced density approach, is the definition of the mesh and determining the initial histories for the iterations or the previous run with reduced density. The application of these methods is shown in the next chapters; where comparison of van Wijk's methodology amongst the root and density reducing strategies (to overcome long histories) are performed using two different geometries. The first geometry is the ITER SDR computational benchmark. This model, provided by the ITER Organization (IO) for verification studies, includes absorbent materials as well as small gaps. Due to the simplicity of the configuration, differences within variance reduction methods for problematic regions are more evident than using a complex geometry. Nonetheless, proper performance of the techniques is expected for large intricate models. For that purpose a second comparison using the ITER neutronics B-lite model is also shown afterwards.

4. Applications of GVR using the ITER Benchmark

In this chapter van Wijk's GVR technique is compared to the modifications in the algorithm previously described. The ITER computational benchmark is used to perform this comparison.

4.1. Geometry description and methodology

Precise neutron flux calculations are necessary as a first step for accurately determining the SDR. Due to the large and complex geometry of the ITER design, it is not wise to test and validate methodologies directly onto the model. For this purpose, the ITER SDR computational benchmark has been defined. This benchmark consists of a simplified model of an ITER element including several features that may cause issues during the neutron transport calculations; making it appropriate to use as a first case for this study.

The benchmark features dimensions, materials, shielding, and streaming characteristics that resemble an ITER equatorial port. Shielding materials and gaps are present at ITER's equatorial ports, and significant transport complications will emerge due to their presence. Therefore, the benchmark geometry was designed to include these features. A detailed arrangement of the benchmark can be seen in **Figure 4-1**.

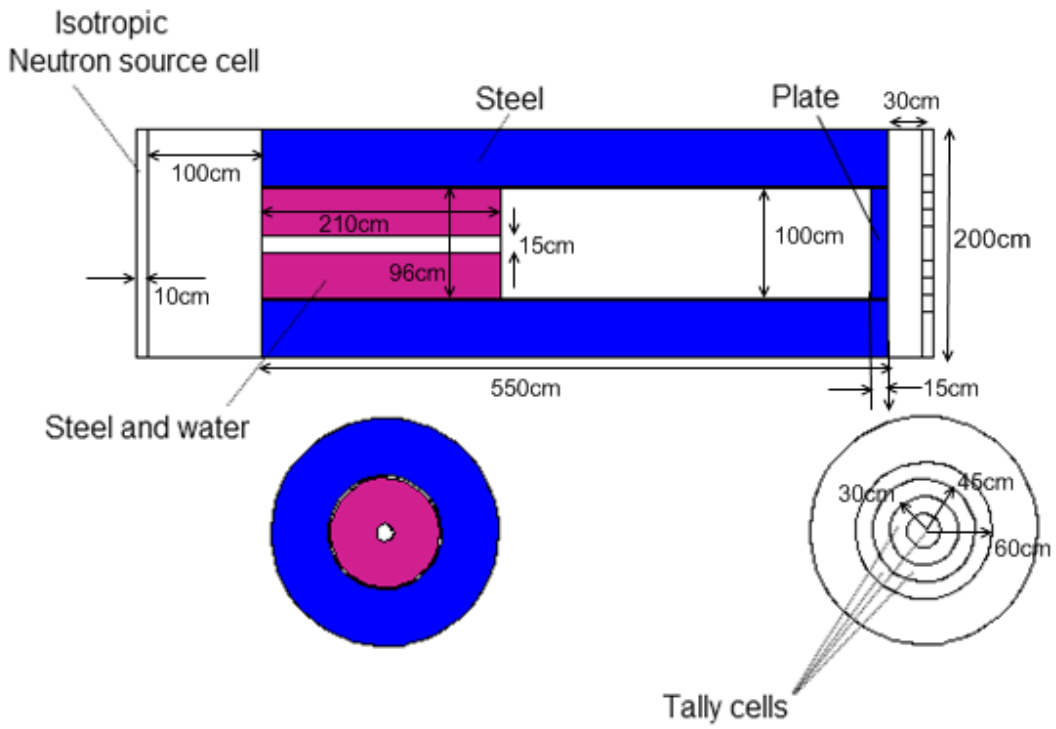

Figure 4-1 Detailed geometry of ITER computational benchmark

In this cylindrical configuration, a volumetric 14 MeV isotropic neutron source emits uniformly from the 10 cm source cell. After a 100 cm gap, the material section consists of two coaxial cylinders with a 2 cm gap between them. The outermost cylinder has a total length of 550 cm and is made of steel; its outer and inner radii are 100 cm and 50 cm respectively. In the rear part there is a 15 cm steel plate, also with a 2 cm gap separating the cylinder from the plate. The inner cylinder only expands for 210 cm and has an outer radius of 48 cm, it's made of steel (78%) and water (22%). Inside this cylinder there is a 15 cm diameter hole.

Using an analog simulation with implicit capture (**AWIC**) as a reference, the GVR techniques described in the previous section are compared:

- Van Wijk's flux based weight maps (**Eq. 3-4**): **vanWijk_F**
- Van Wijk's relative error based weight maps (**Eq. 3-3**): **vanWijk_Re**
- Van Wijk's flux based weight maps using the square root over **Eq. 3-4: SQRT_F**
- Density reduction of the materials in half, over flux based maps (**Eq. 3-4**): **HD_F**
- Density reduction of the materials in half, over relative error based maps (**Eq. 3-3**): **HD_Re**

Implicit capture will not be turned off for the comparison, due to the main goal of this study being the improvement of MCNP calculations. Likewise, being a default feature of the program that is also included in the GVR procedures to be compared, excluding implicit capture from the analog run would mislead the improved results of the techniques on their own. As for the density reduction in this case, the run used to create the weight maps is done with all the materials density set to a half of their real value; note that no iterations are needed and that in the final run densities are set to their real values. Lastly, all the global weight maps are created externally from MCNP. For this purpose, a script

written in Python is used to process the neutron flux and relative error data found in the *meshtal* file.

To comply with the ITER project nuclear analyses standards, neutron transport is performed with the MCNP5 v1.6 [50] radiation transport code using the FENDL-2.1 [51] evaluated nuclear data library for fusion applications. The transport using WW is done over a Cartesian mesh consisting of 4 x 4 x 4 cm^3 voxels; and the weight of particles is checked only at the collision sites. The geometric model is created in MCNP as a 90º section of the cylinder with reflecting sides; it is shown in Figure 4-2. A cross cut perpendicular to the *z*-axis at Z = 0 displays the steel and steel/water cylinders, and at Z = 542 the steel back plate with the outer cylinder can be seen (with and without the GVR mesh). The plane perpendicular to the *x*-axis at X = 0 is also shown, with and without the GVR mesh.

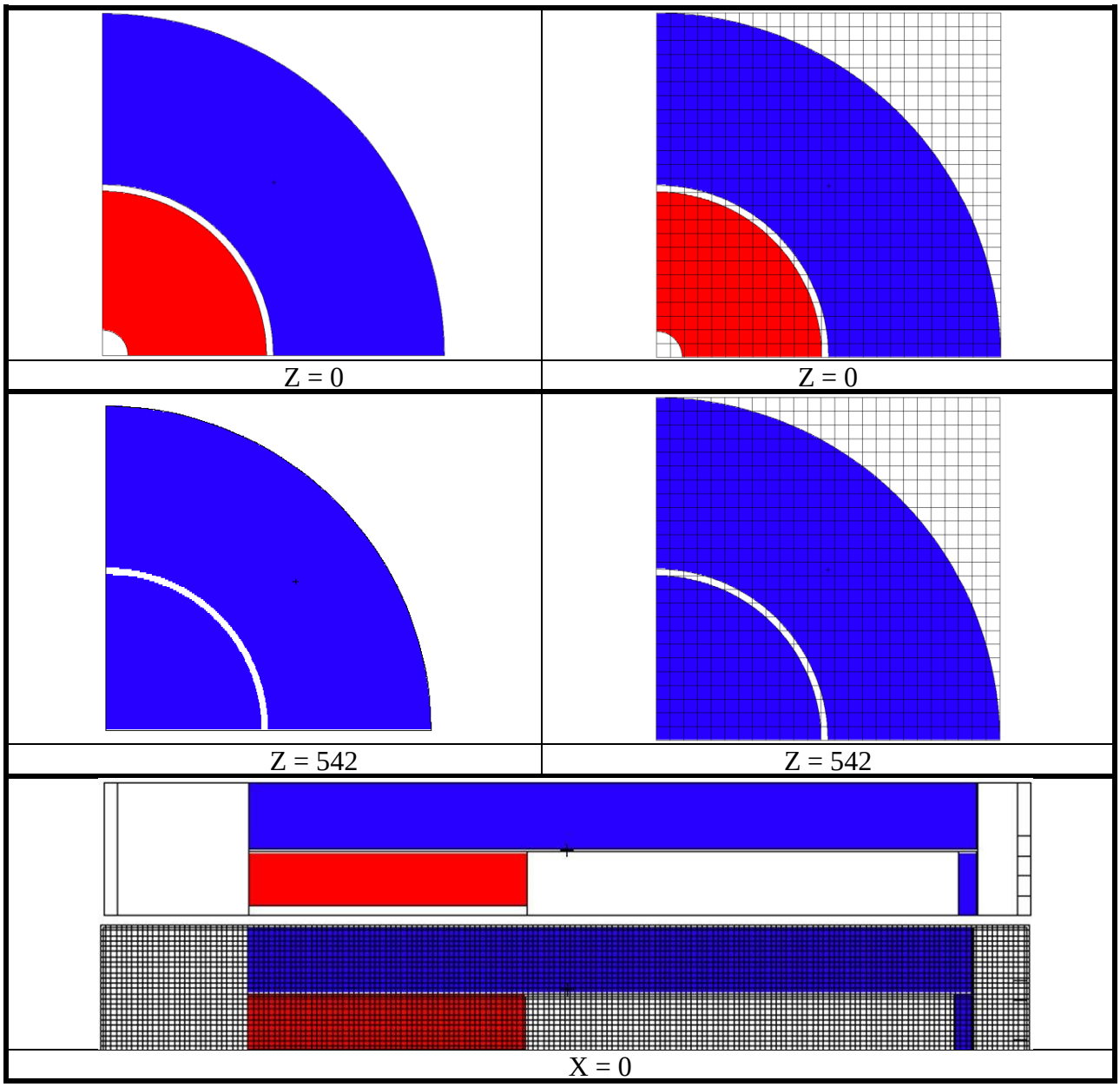

Figure 4-2 MCNP Benchmark model and mesh layout used for the comparison calculations

Note that these meshes are taken to create the weight maps; and size of the voxels must remain the same through this entire process. Once the weight map is created it will be used as a "part of the WW MCNP input", and any mesh tally of interest may be defined as an output for a final run, independently of the WW input mesh. In this case, the size of the voxels to create the weight map was taken only in terms of the comparison study and the

final run is done using the same mesh. Nonetheless, when tallying neutron flux for a subsequent SDR calculation, voxel size for the output mesh tally is recommended to be more precise in the regions where the materials activation is more likely to contribute to the dose (see 5.2).

Validation of the techniques will be done by comparing a tally defined in the rear section of the back plate (cell 201) shown in Figure 4-3.

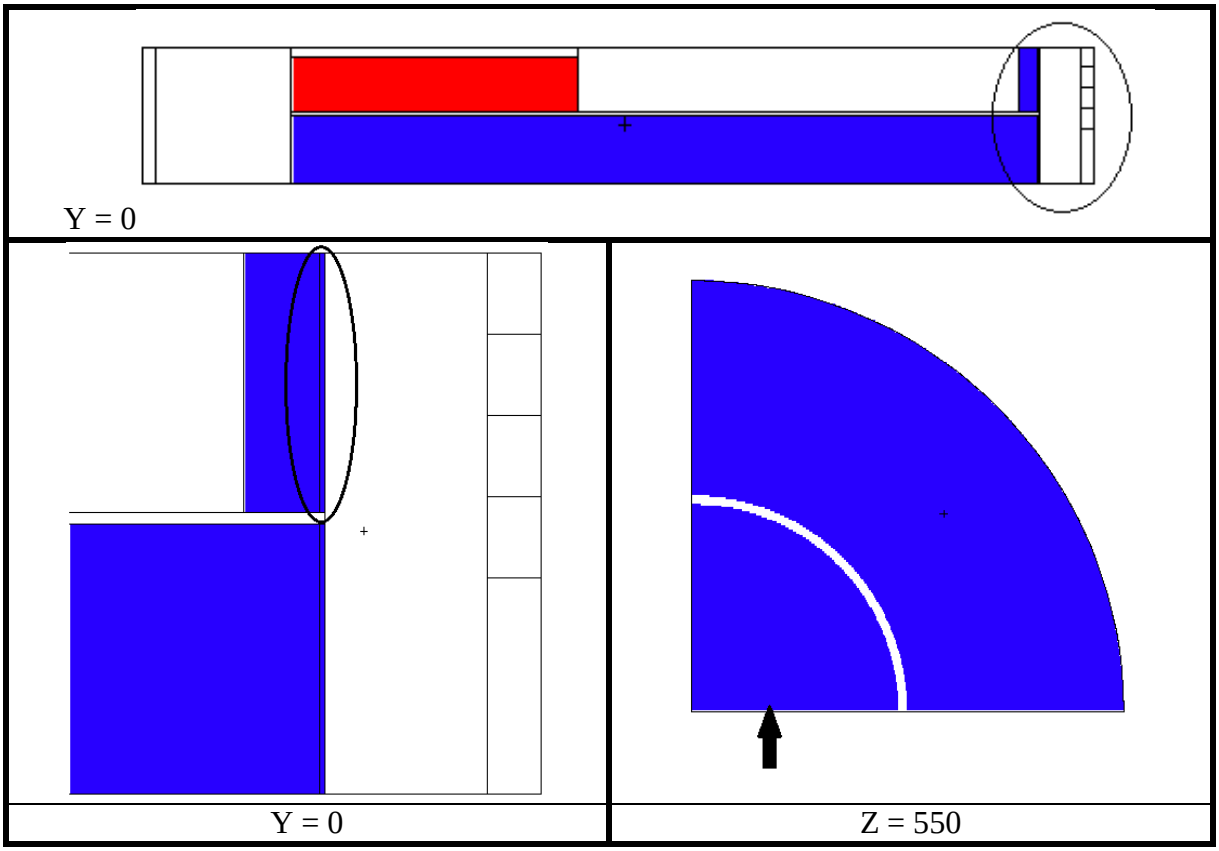

Figure 4-3 Location of cell 201 in the benchmark used for verification of the GVR methods

All the calculations presented were performed using the same number of processors and, for the final runs, similar CPU times were targeted in order to make the comparison.

Besides, since previous simulations are necessary, the total CPU time spent in the creation of the weight maps is also indicated as a reference.

The parameters that will be compared are the percentage of the voxels not scoring, the average error, and the FOM. In Figure 4-2 it can be seen that not all of the voxels are inside the geometry (see Z=0 and Z=542), and therefore will not tally. To exclude these voxels from the results, a previous void simulation showed that 19% will never score, and will consequently be taken out of the provided results. Lastly, effectiveness of the final simulations is evaluated using the FOM as defined in [42]:

$$FOM_{GVR} = \left(\sum_{i=1}^{N} \frac{Re_i^2}{N} T_{CPU}\right)^{-1}$$

Eq. 4-1

Where Re_i is the relative error in each voxel of the mesh, N is the total number of voxels, and T_{CPU} is the computational time, in minutes, of the simulation. For the calculation of the FOM, voxels within the geometry that do not score (i.e., have a zero relative error and no neutron flux) are counted as having a relative error value of 1.0.

Neutron flux tallies have a source normalization factor of $1.97 \cdot 10^{19}$ n/s in the ITER B-lite neutronic model (see 5.1.1); hence, in the calculations performed for the benchmark problem this factor is taken into account. Maps of the neutron flux and relative errors in the geometry are also shown. These were created using the Paraview data analysis and visualization application [52].

4.2. Results and discussion

In this section, results of the comparison for the GVR techniques are shown over the ITER benchmark. Before discussing the results, an overview of the weight maps creation is presented.

Of the five GVR methods compared, three of them: van Wijk's error based maps (**vanWijk_Re**), density reduction of the materials in half over flux based (**HD_F**), and density reduction over the error based (**HD_Re**) maps, are not improved by iterations and only one previous run is necessary. This prior simulation is an analog run including implicit capture, and is done with the same number of histories in all cases (10^9). In the simulation with density reduction based techniques (**HD_F** and **HD_Re**), most of the geometry is sampled and only 0.4% of the voxels do not score. Likewise, for the relative error based method (**vanWijk_Re**), a total of 1.8% of the geometry is left unsampled. Therefore, WW is turned off in these voxels since they do not show defined limits. On the other hand, van Wijk's flux based weight maps (**vanWijk_F)** and square roots taken over flux based maps (**SQRT_F**) needed an extra iteration (aside from the initial run) to cover all the geometry. These were all done with 10^8 initial histories. Total times for the map creation and the percentage of voxels not optimized are summarized in Table 4-1.

Table 4-1 Computer times for weight map creation and unsampled voxels for the benchmark geometry

	vanWijk_F	vanWijk_Re	SQRT_F	HD_F	HD_Re
CPU hours	442	61	15	59	59
% of voxels not sampled in final weight map	0	1.8	0	0.4	0.4
Previous runs/iterations	2	1	2	1	1

The large computer time needed for the **vanWijk_F** based map shows how oversplitting can cause the opposite effect as the one pursued. In fact, the MCNP output shows that due to WW for every source track, in **vanWijk_F** map creation, 100 additional tracks are formed through the splitting process in the iteration; opposed to the 0.25 extra tracks per source particle created in the **SQRT_F** iteration.

Final simulations are compared targeting a similar computer time. Quantification of the results for the mesh tallies are summarized in Table 4-2. It can be seen how the five GVR methods show similar average error, all under the required 5% to be considered reliable for an MCNP calculation. Therefore, an improvement over the analog with implicit capture (**AWIC)** simulation is achieved in all cases.

Table 4-2 Comparison of the GVR methods using the ITER benchmark

	AWIC	**vanWijk_F**	**vanWijk_Re**	**SQRT_F**	**HD_F**	**HD_Re**
NPS	6.7E+09	1.0E+08	3.7E+09	4.1E+09	3.0E+08	5.3E+10
CPU hours	340	339	337	330	333	340
Percentage of voxels not scoring (%)	0	0	0	0	0	0
Average error (%)	8.0	3.5	1.1	1.1	2.2	1.2
FOM	2.10E-03	1.72E-02	1.67E-01	1.95E-01	4.63E-02	1.25E-01
Extra tracks per source particle	-	21	0.2	0.2	5.8	0.07

The **SQRT_F** and **vanWijk_Re** techniques display similar results. These two methods also show the highest FOM, making them the most optimized techniques. Note that in the **vanWijk_Re** method most of the geometry is sampled in the run to create the weight map; for larger geometries this will not be the case, making the final run perform not as thoroughly as for this design.

Reducing the materials densities in the system lead to well optimized weight maps likewise. With the relative error based method (**HD_Re**) showing moderately better results than the flux based (**HD_F**). As stated previously this is due to oversplitting not being totally addressed in the flux based weight map, even though improvement over the **vanWijk_F** technique is achieved.

In order to visualize how oversplitting affects the calculations, neutron flux maps can be seen in Figure 4-4 and Figure 4-5.

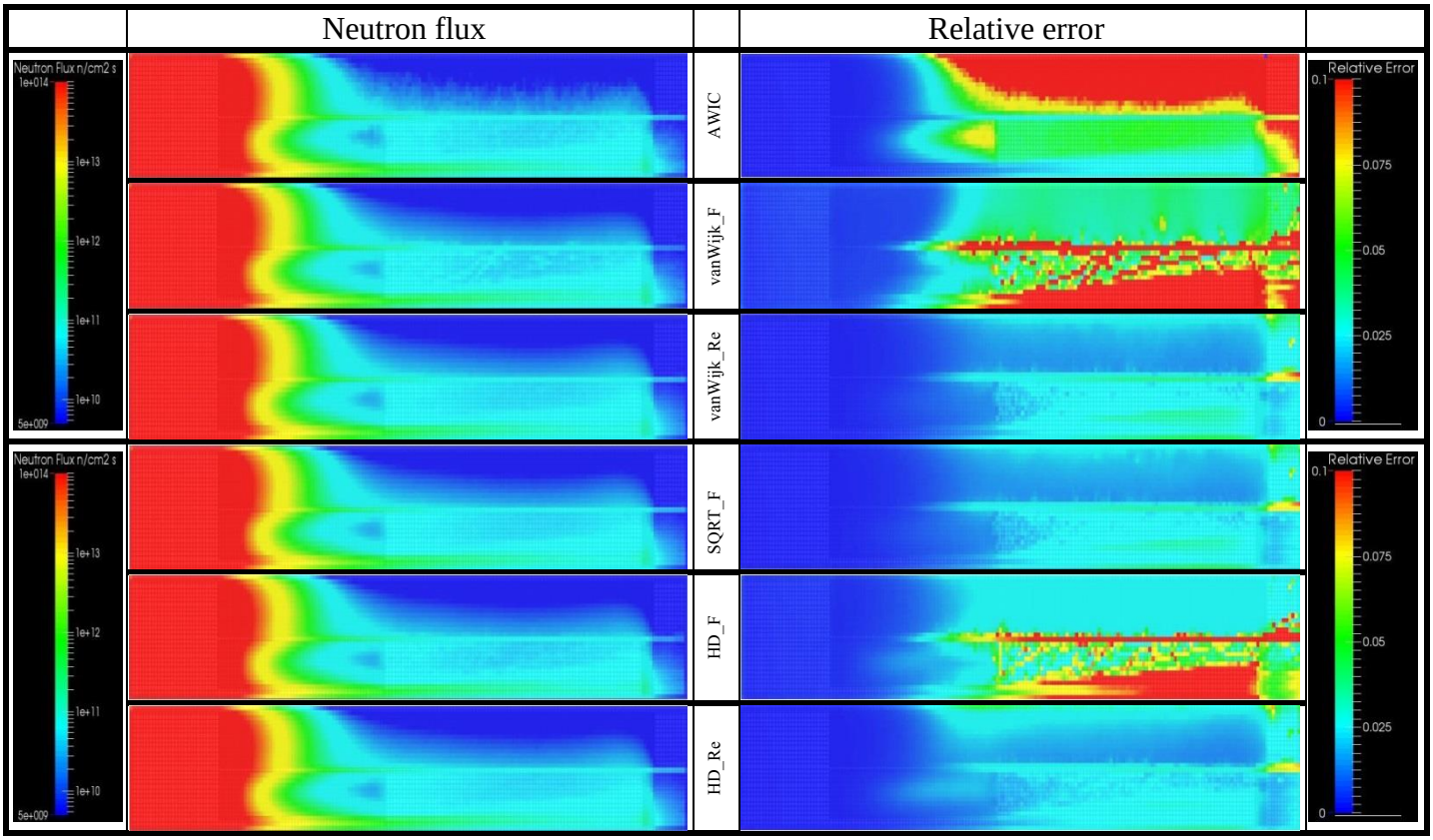

Figure 4-4 Neutron flux and relative error for the ITER benchmark at X=0 for the: AWIC, vanWijk_F, vanWijk_Re, SQRT_F, HD_F, and HD_Re weight maps, after the same computer times

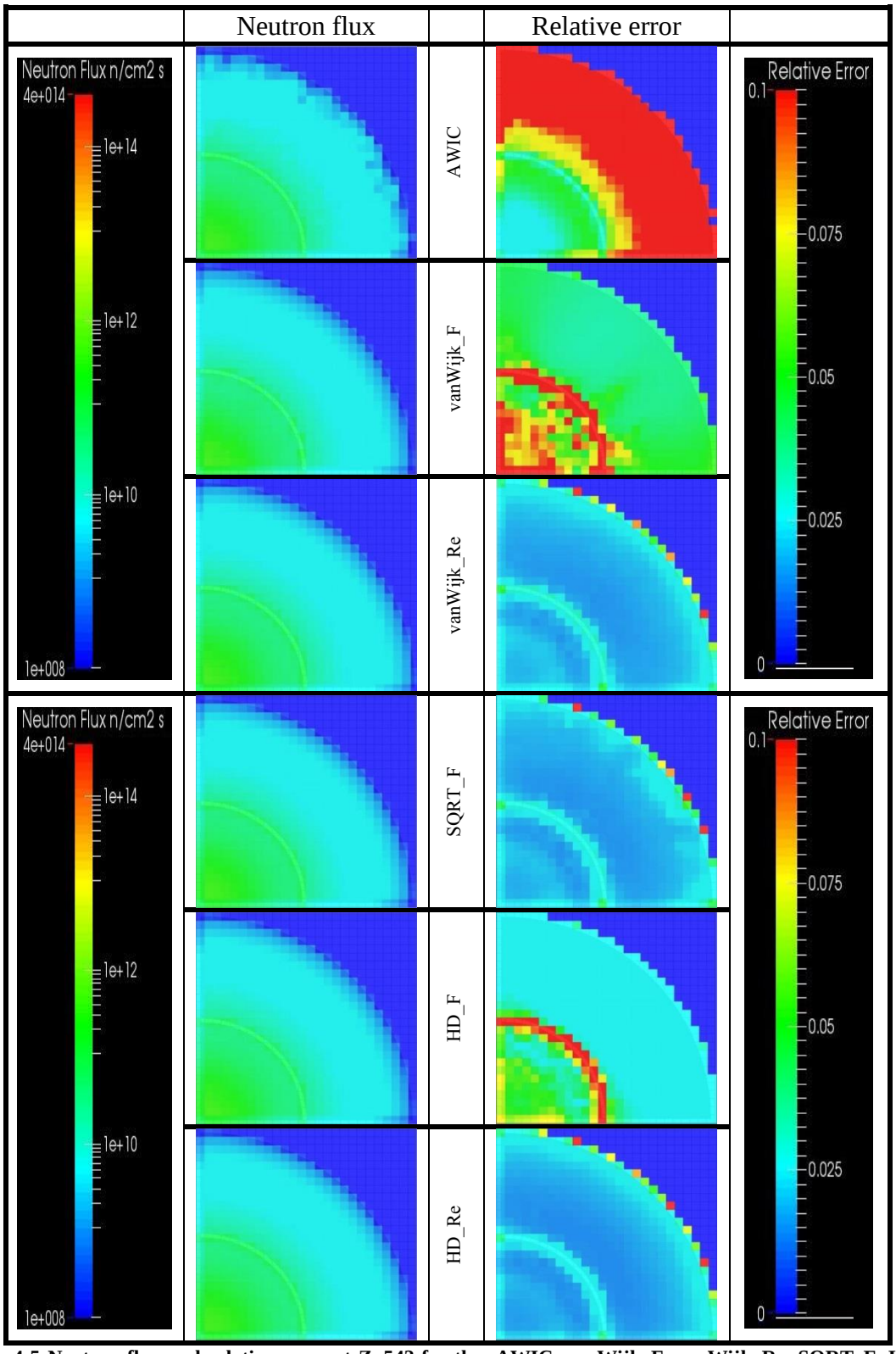

Figure 4-5 Neutron flux and relative error at Z=542 for the: AWIC, vanWijk_F, vanWijk_Re, SQRT_F, HD_F, and HD_Re weight maps, after the same computer times

In Figure 4-4 a cross cut is shown at X=0, placed at the center of the cylinder configuration. At the top of the maps is the solid steel cylinder container, and in the **AWIC** run it is clear that this is the region with less sampling (higher relative error). However, for the flux based maps, **vanWijk_F** and **HD_F**, the void region behind the inner cylinder appears to be undersampled, having most of the errors above 10%. This is due to the steel and water inner cylinder not being optimized enough. Taking a look at Figure 4-5, where a cut at Z=542 shows the back plate and the outer steel cylinder, it seems that poor sampling also occurs at the gaps. Another cross cut at the geometry showing only the relative error maps for all cases can be seen in Figure 4-6.

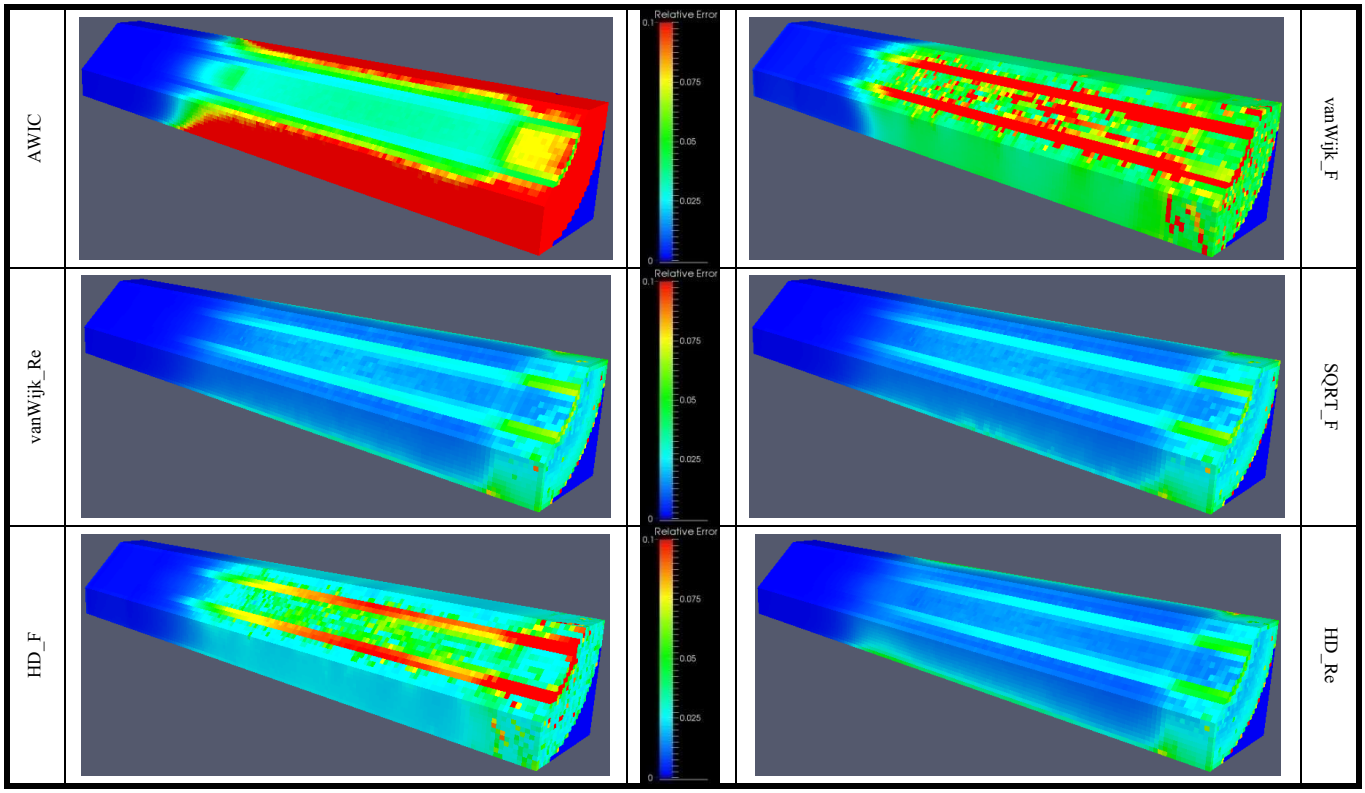

Figure 4-6 Cross cut at x+y=60 showing relative error map for the benchmark configuration, using the: AWIC, vanWijk_F, vanWijk_Re, SQRT_F, HD_F, and HD_Re weight maps

As stated before, streaming through small apertures is an infrequent event that can be clearly seen in Figure 4-6. Namely, using GVR techniques does not involve having different relative errors in the gaps with relation to the surrounding regions; if the errors happen to be higher, it indicates that only a few particles having high weight have entered the gaps. Furthermore, if long histories due to particle streaming through the gaps were present, the relative error in the gaps would be lower, because oversplitting causes additional oversampling. However the under sampling at the gaps is more noticeable in the simulations using flux based maps **vanWijk_F** and **HD_F**. This happens because for the same computer time, final runs using these techniques have around 10^8 initial histories; whereas for the other simulations they have at least 10^9 histories. A reduced number of source histories have been used for the **vanWijk_F** and **HD_F** based maps, to have a reasonable computing time (as a result of the increase of computing time due to the oversplitting issues through the highly absorbent materials). As a consequence of improper sampling for the streaming paths, tallying at the rear part of the geometry may not give accurate results and initial histories should be increased.

In addition, Figure 4-7 sums up all the relative error distributions. It shows how in all the GVR techniques voxels have relative errors under 0.2. Furthermore, even though the **SQRT_F** presents the best results, it can be seen how **vanWijk_Re** and **HD_Re** perform with comparable outcome.

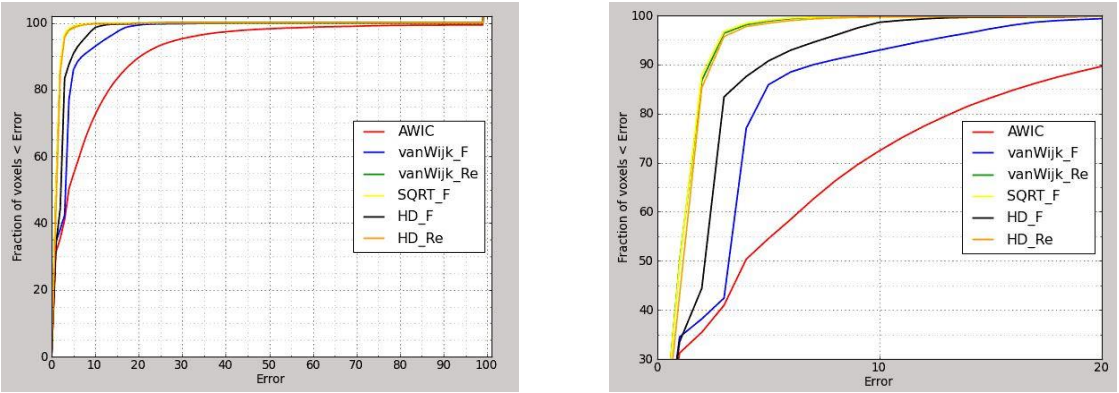

Figure 4-7 Relative error distributions of the flux mesh tallies for the ITER benchmark problem

Lastly, the reliability of each technique is validated. Table 4-3 shows the neutron flux and relative error obtained for each method at the same cell, located at the back plate. Comparison with the **AWIC** simulation shows all the results are within the margins of error. The **vanWijk_F** and **HD_F** techniques, which performed the worst in terms of FOM and average error in the global comparison, also achieved the worst relative error in this case.

Table 4-3 Neutron flux and relative errors at cell 201

	AWIC	**vanWijk_F**	**vanWijk_Re**	**SQRT_F**	**HD_F**	**HD_Re**
Neutron flux (n/cm2 s)	9.30E+09	9.45E+09	9.28E+09	9.33E+09	9.32E+09	9.32E+09
Relative error	0.009	0.037	0.006	0.006	0.022	0.005

4.3. Conclusions to the benchmark problem

All the GVR techniques tested showed consistency compared to the **AWIC** simulation when tallying the same cell. Additionally, all methods displayed significant improvement over the **AWIC** simulation in terms of FOM and average error. Best results were obtained by the **SQRT_F** approach, where the FOM shows an improvement of nearly two orders of magnitude over the **AWIC**. Additionally, this technique also features the lowest computer time for the weight map creation. But it must be kept in mind that only an extra iteration was needed due to the size of the geometry.

Results comparable to the **SQRT_F** technique are achieved with the **vanWijk_Re** and **HD_Re** methods. However, the fact that these techniques do not improve weight maps by means of iterating implies that most of the voxel sampling must be accomplished in the first run. This may be an issue for large geometries with highly absorbent materials (especially for the **vanWijk_Re** map). Since increasing the source histories to tally through all the mesh, without variance reduction techniques, could lead to extremely long simulations that may not be manageable.

Oversplitting issues through the materials cause the **vanWijk_F** and **HD_F** methods to perform the worst in a given time. Furthermore, gaps do not show proper sampling; whereas the other techniques do not display this problem.

Increasing the complexity and the size of the system is the next step for this comparison study. A more intricate model is therefore considered in the next chapter

5. Applications of GVR using the ITER B-lite model

After the preceding calculations, a more realistic model is used for the comparisons in this chapter. In the first part, the optimization of neutron transport is compared; where, aside from the approaches taken before, weight maps using cubic roots taken over the neutron flux are also included. In the second part, the two most optimized maps are used as an MCNP input to perform SDR calculations behind the equatorial port.

5.1. Comparison of GVR methods over the entire ITER reactor

5.1.1. Geometry description and methodology

In addition to the problematic regions featured in the benchmark, a GVR method must be able to properly transport particles to all areas of a large geometry. In order to test these GVR techniques, the ITER neutronics reference model is used. As with the computational benchmark, MCNP5 v1.6 transport code and FENDL-2.1 cross section library are used. Weight checks are done at collision sites only, and maps are also created using the WWG feature in MCNP. But this time, due to the large dimensions, a global Cartesian mesh of 20 x 20 x 20 cm^3 voxels is defined to create the weight maps and as the output mesh of the final run. Again this mesh size is taken only for the comparison study;

and for SDR calculations, final runs are encouraged to have more precise voxels in the regions where materials activation is more likely to contribute to the dose (see 5.2).

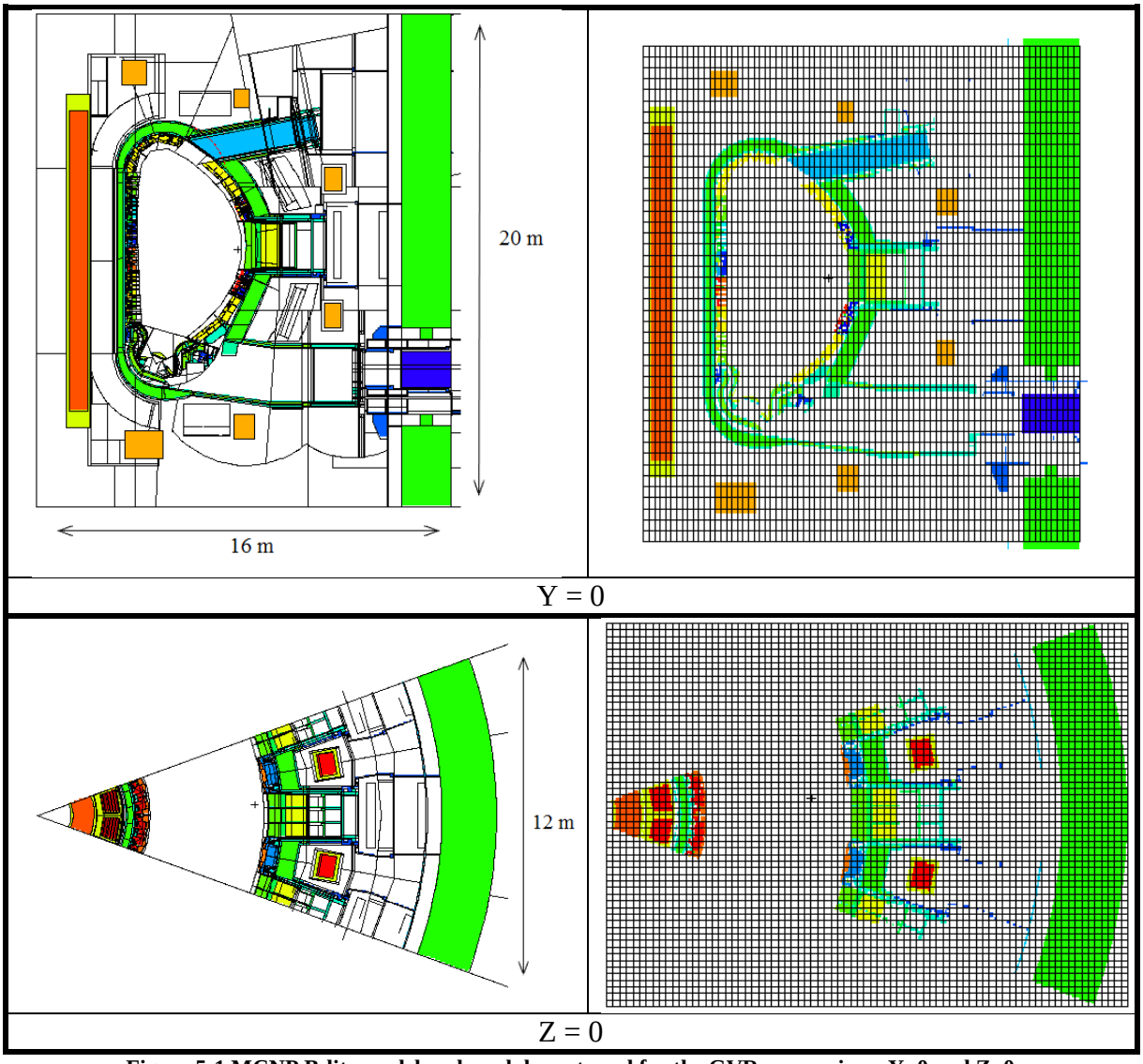

Figure 5-1 MCNP B-lite model and mesh layout used for the GVR comparison. Y=0 and Z=0

The MCNP geometry used is the ITER B-lite v3 configuration [53]. Large dimensions and several gaps in this model, make it an appropriate geometry to test the GVR approaches in terms of oversplitting issues. It consists of a 40º section of the ITER reactor with reflective sides as seen in Figure 5-1. A full equatorial port and two halves are

included, which present small gaps and highly absorbent materials, as recreated in the previous benchmark. The reactor expands for about 16 m horizontally (in the *x* direction), has a height of around 20 m (in the *z*-axis), and the widest part at the back is close to 12 m (in the *y*-axis). The isotropic neutron source is located in the vacuum vessel, and is defined as a Gaussian distribution with mean energy of 14.1 MeV. Taking into account 500 MW of fusion power, in this model flux tallies have a source normalization factor of $1.97 \cdot 10^{19}$ n/s that has been included in all calculations.

In this case, van Wijk's flux based method (**vanWijk_F)** could not be included in the comparison due to long histories blocking the simulations during the weight map creation. However, the cubic root over van Wijk's flux approach was included to determine its behavior. Therefore, the comparison against the analog with implicit capture (**AWIC)** case is made with the van Wijk's error based (**vanWijk_Re)**, square root over flux based (**SQRT_F)**, density reduction of the materials in half over flux based (**HD_F**) and error based (**HD_Re)**, and cubic root over flux based (**CBRT_F**, iterations using the cubic root over the flux in **Eq. 3-4**) techniques.

Figure 5-1 also shows the global mesh over the geometry for Y=0 and Z=0. In order to exclude voxels outside the geometry, a previous void simulation showed that 41% of them will never score. Again, these will be taken out of all the results.

The targeted CPU time for this comparison is $1.2 \cdot 10^3$ hours. All final simulations were run using the same number of processors and time for the weight maps creation is also discussed. The same Python script (as in the previous chapter) to create the maps is used, and parameters to quantify the results are also the same as with the benchmark: percentage

of voxels not scoring, average error, and FOM (**Eq. 4-1**). Lastly, neutron flux and relative error maps are created with the Paraview application.

5.1.2. Results and discussion

The weight maps presented for these results cover the entire geometry for the B-lite model. Yet, GVR techniques can also be applied to large components that do not encompass all the design. If this is the case, and only a region is of interest, total time invested in creating the map, and the final simulation, can be considerable shorter. Likewise, a weight map covering the entire model can also be used if only an area within it is of interest, making it a useful resource that must only be created once.

An overview of the weight map creation is now presented. Of the five maps, **SQRT_F** and **CBRT_F** based methods required three iterations, aside from the first analog with implicit capture run. These were all done with 10^9 initial source histories and the total time invested was of $7.5 \cdot 10^3$ and $5.7 \cdot 10^3$ CPU hours respectively. Since not all the voxels could be tallied an extra iteration was performed, but no improvement was shown compared to the third iteration. Instead of increasing source histories, the weight maps are left with these untallied voxels to be compared with the other procedures, which maps are also created with 10^9 histories. Nonetheless, the percentage of unsampled voxels is not as significant for the **SQRT_F** procedure (2.1%) compared to the **CBRT_F** (9.7%).

As expected, the **vanWijk_Re** weight map is the least thorough, and 21% of the voxels did not score, leaving the WW turned off for a fifth of the geometry. The time for creating this map ($1.2 \cdot 10^3$ CPU hours) is the same as the time invested in the **HD_F** and

HD_Re approaches, which only present 1.8% of the voxels not scoring. These previous calculations are summarized in Table 5-1.

Table 5-1 Computer times for weight map creation and unsampled voxels for the B-lite geometry

	vanWijk_Re	SQRT_F	CBRT_F	HD_F	HD_Re
CPU hours	1.2E+03	7.5E+03	5.7E+03	1.2E+03	1.2E+03
% of voxels not sampled in final weight map	21	2.1	9.7	1.8	1.8
Previous runs/iterations	1	4	4	1	1

Final simulation results are shown in Table 5-2. In opposition to the benchmark problem, best sampling now occurs with the **HD_F** technique; having in this case the higher FOM (an order of magnitude above the **AWIC** case), lowest average error (7.6%), and a more thorough sampling (only 0.1% of the voxels not scoring). It stands clear, that in different geometries GVR techniques will behave differently. Close to the **HD_F** approach, the **SQRT_F** method is the second best technique.

Table 5-2 Comparison of the GVR methods using the ITER B-lite model

	AWIC	vanWijk_Re	SQRT_F	CBRT_F	HD_F	HD_Re
NPS	2.0E+09	4.5E+08	6.4E+08	9.7E+08	2.5E+08	6.5E+08
CUP hours	1.28E+03	1.22E+03	1.23E+03	1.23E+03	1.19E+03	1.22E+03
Percentage of voxels not scoring (%)	20.1	6.1	1.2	8.6	0.1	8.6
Average error (%)	20.1	9.4	10.0	10.9	7.6	12.6
FOM	4.5E-05	1.2E-04	2.1E-04	9.7E-05	4.7E-04	8.9E-05
Extra tracks per source particle	-	3.4	2.3	0.7	5.7	1.5

Relative error distributions can be seen in Figure 5-2. An improvement over the **AWIC** case is shown through all the GVR techniques. In all the final runs, over 70% of the

voxels score with a relative error under 0.1, in contrast with the **AWIC** run with only 20% of the voxels under a 0.1 relative error. Worst optimization is achieved using the **HD_Re** and **CBRT_F** methods, which perform similarly. These two techniques happen to have the lowest number of tracks created per source history. In the previous benchmark problem, techniques with a small number of extra tracks (**vanWijk_Re** and **SQRT_F)** performed better than the rest, and the worst results were obtained for the map that created the most extra tracks (**vanWijk_Re**). However, in a large geometry the opposite seems to be true. This can be explained taking into consideration the complexity of the B-lite model. In this case, homogenization of the particle population density is better achieved with not so smooth weight maps, since differences in the materials are also sharper.

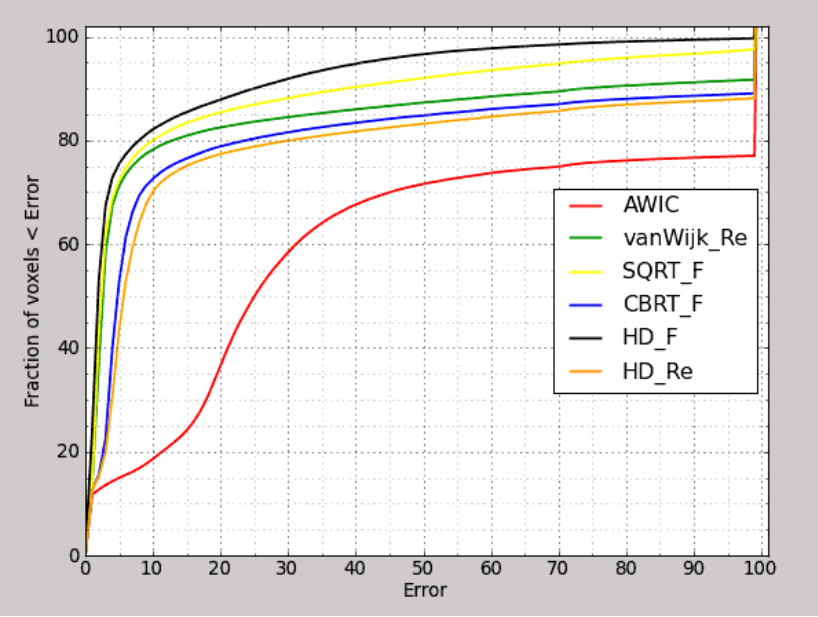

Figure 5-2 Relative error distributions of the flux mesh tallies for the ITER B-lite model

Figure 5-3 and Figure 5-4 feature the neutron flux and relative error maps at Y=0 and Z=0 respectively. Taking a look at these figures, it can be seen how the "problematic" areas, such as the equatorial and upper ports, are the worst sampled in all cases (aside from the bioshield and the inboard). Comparing the **HD_F** and **SQRT_F** simulations, the improvement of the **HD_F** case over the **SQRT_F** is mostly due to further sampling in the bioshield. On the other hand, note how the **vanWijk_RE** algorithm performs extremely well even though ~20% of the geometry has the weight windows game turned off. Figures show how this method behaves properly in the regions that could be reached in the previous simulation, while hard to reach areas remain unsampled.

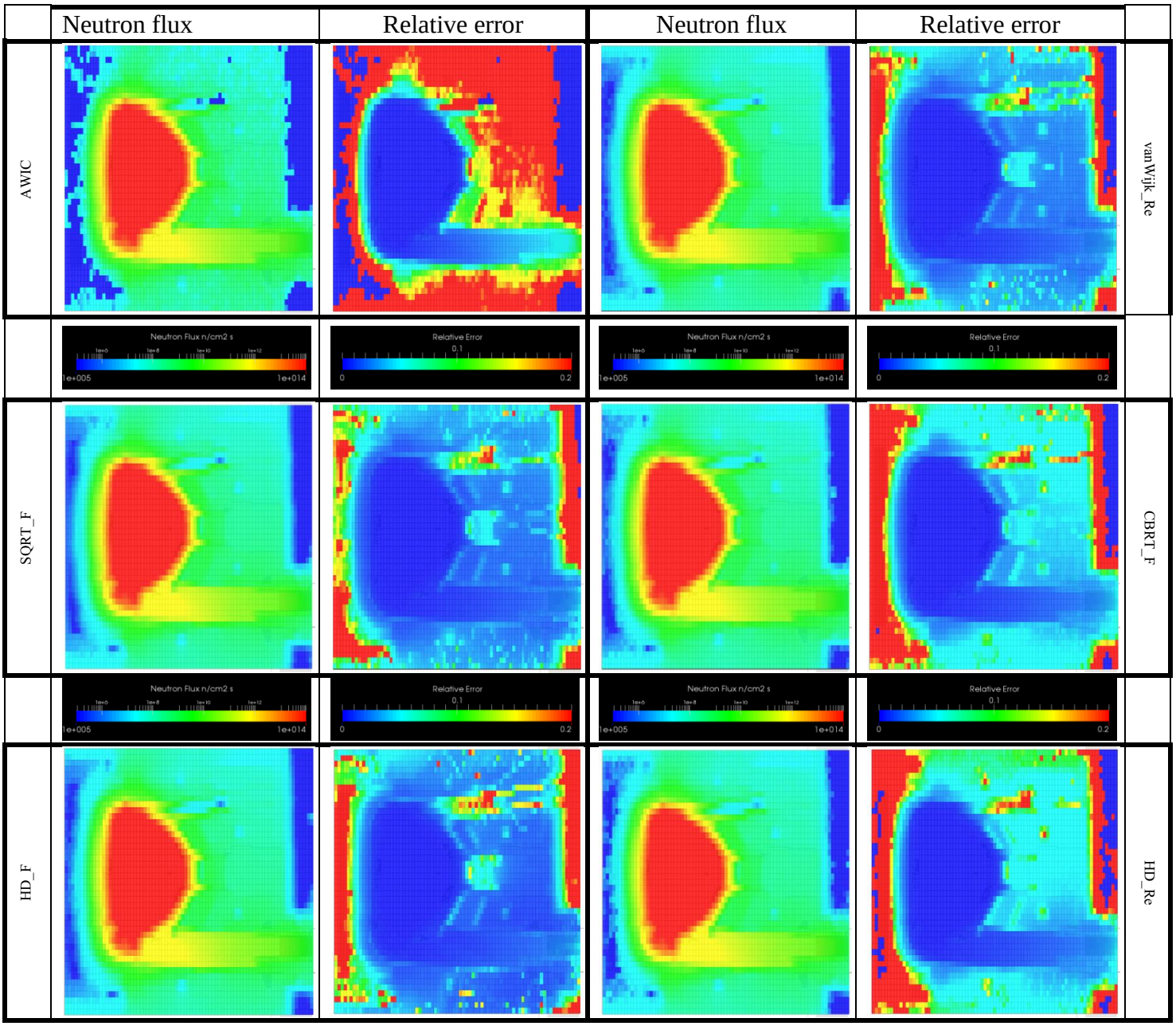

Figure 5-3 Neutron flux and relative error maps in a global mesh throughout the B-lite model at Y=0 for the: AWIC, vanWijk_Re, SQRT_F, CBRT_F, HD_F, and HD_Re weight maps, after the same CPU time

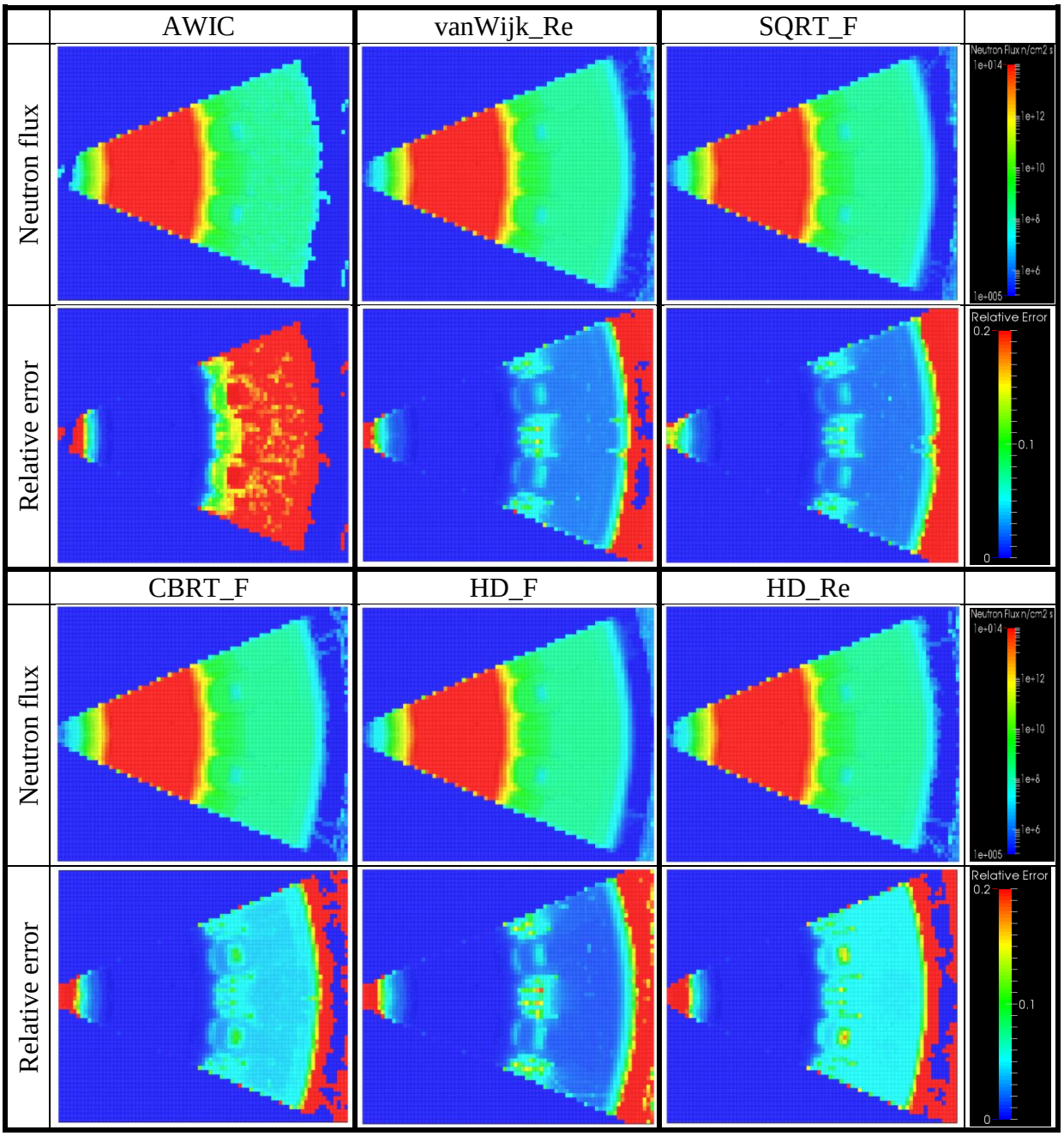

Figure 5-4 Neutron flux and relative error maps in a global mesh throughout the B-lite model at Z=0 for the: AWIC, vanWijk_Re, SQRT_F, CBRT_F, HD_F, and HD_Re weight maps, after the same CPU time

5.1.3. Conclusions to the B-lite geometry

As with the previous system, an improvement over the **AWIC** simulation is obtained with all the GVR approaches. Where relative errors under 0.1 are achieved in 20% of the geometry, runs using the GVR maps improve this percentage for over 70% of the voxels in all cases.

Contrarily to the benchmark problem, the **HD_F** approach outperforms the rest of the techniques, even though results are similar using the iterative **SQRT_F** method. The only significant difference amongst them occurs at the back of the bioshield. As expected, the performance of the **vanWijk_Re** method is also notable, but only in the regions sampled in the weight map creation run.

Worst global results are obtained by the over smoothed maps created by the **CBRT_F** and **HD_Re** techniques. These methods overly flatten the weight maps, thus not taking into account differences in the complex geometry, and therefore not distributing the population in an optimized way.

5.2. Calculation of SDR using GVR techniques at the equatorial port of ITER

5.2.1. Geometry description and methodology

Using the most optimized weight maps of the previous section to transport neutrons, in this section a SDR calculation is performed over a mesh covering the equatorial port of ITER. Before detailing the geometry and the methodology applied, a more detailed overview of the R2S tool is given.

As stated in 3.1, SDR calculations using the R2S methodology can be summarized into three steps: transport of neutrons to regions of interest, activation of the materials by the neutrons to define the decay gamma sources, and decay gamma transport. In order to perform SDR calculations, these steps are coupled with the R2S methodology. The first coupling process consists of delivering the neutron flux to an activation code. The neutron flux is evaluated in the first transport calculation; generally 175 energy groups are used to evaluate the neutron spectra. In the first coupling step, neutron flux, the initial materials, and the irradiation scenario are used as input for the activation code. Secondly, after activation calculations, the decay gamma source is obtained for a given cooling time. In this second coupling step, this decay gamma source is used as the source for the gamma transport simulation. This final transport simulation will provide the gamma spectra at the desired locations and SDR is obtained by multiplying the gamma flux by flux-to-dose conversion factors. Note that the R2S tool can be used for other response functions other

than the SDR (e.g., activity, decay heat, or contact dose). In these cases only the first coupling process is needed (from the radiation transport code to the activation code).

Two approaches can be taken to evaluate the neutron flux in the first step of an R2S calculation. This flux can be evaluated inside the cells present in the geometry or inside voxels using a superimposed mesh over the geometry. The cell based approach has the advantage of featuring only one material, although the neutron flux space resolution may not be suitable depending on the geometry; since the cells can be very large and only the averaged flux over the cell will be computed, in this case information on flux gradients inside the cell is lost. On the other hand, a mesh based approach can be adjusted to refine the spatial resolution, thus having the advantage of obtaining an adapted neutron flux resolution. However, inside a voxel of the superimposed mesh more than one material may be found. In this case, in which more than one material is found inside a voxel, the average neutron flux inside each voxel is typically taken. For this work, the R2S-UNED [54] code (which couples a modified version of MCNP with the ACAB [55] activation code) is used. The R2S-UNED tool includes the unique feature of separately calculating neutron fluxes (i.e., multiflux calculations) for every cell inside each voxel. For other features regarding the R2S-UNED tool see [54].

In this section, a comparison of SDR calculations using the GVR techniques previously applied is shown. Special emphasis must be made in the fact of obtaining a proper spatial resolution of the neutron flux, which must be as high as possible for the activation of the materials to be done precisely and obtain a reliable photon source. Since the main goal in this work is to optimize neutron transport calculations using GVR techniques, the two most optimized weight maps of the previous section are used as WW

inputs to perform the neutron transport. These are the square roots taken over van Wijk's flux based approach (**SQRT_F)** and the density reduction of the materials in half over the flux based maps (**HD_F**). The maps are optimized for the entire B-lite geometry; however, as mentioned in 5.1.2, a global weight map can be used to obtain response functions even if only an area within it is of interest.

The SDR is calculated behind the equatorial port, for which two different meshes have been used over this port: one to tally the neutron flux during the neutron transport and one to evaluate the SDR maps. The geometry and the mesh defined to obtain the neutron flux can be seen in Figure 5-5 and Figure 5-6. This mesh is defined with voxels of 10 x 10 cm^2 in the *y* and *z* directions. However, to refine neutron flux in the radial direction (*x*-axis) towards the tally of interest (to achieve a better resolution), for the first 280 cm in the *x* direction voxel size is taken as 10 cm, the next 35 cm voxels are 5 cm, and the size of voxels over the last 27 cm is taken as 3 cm.

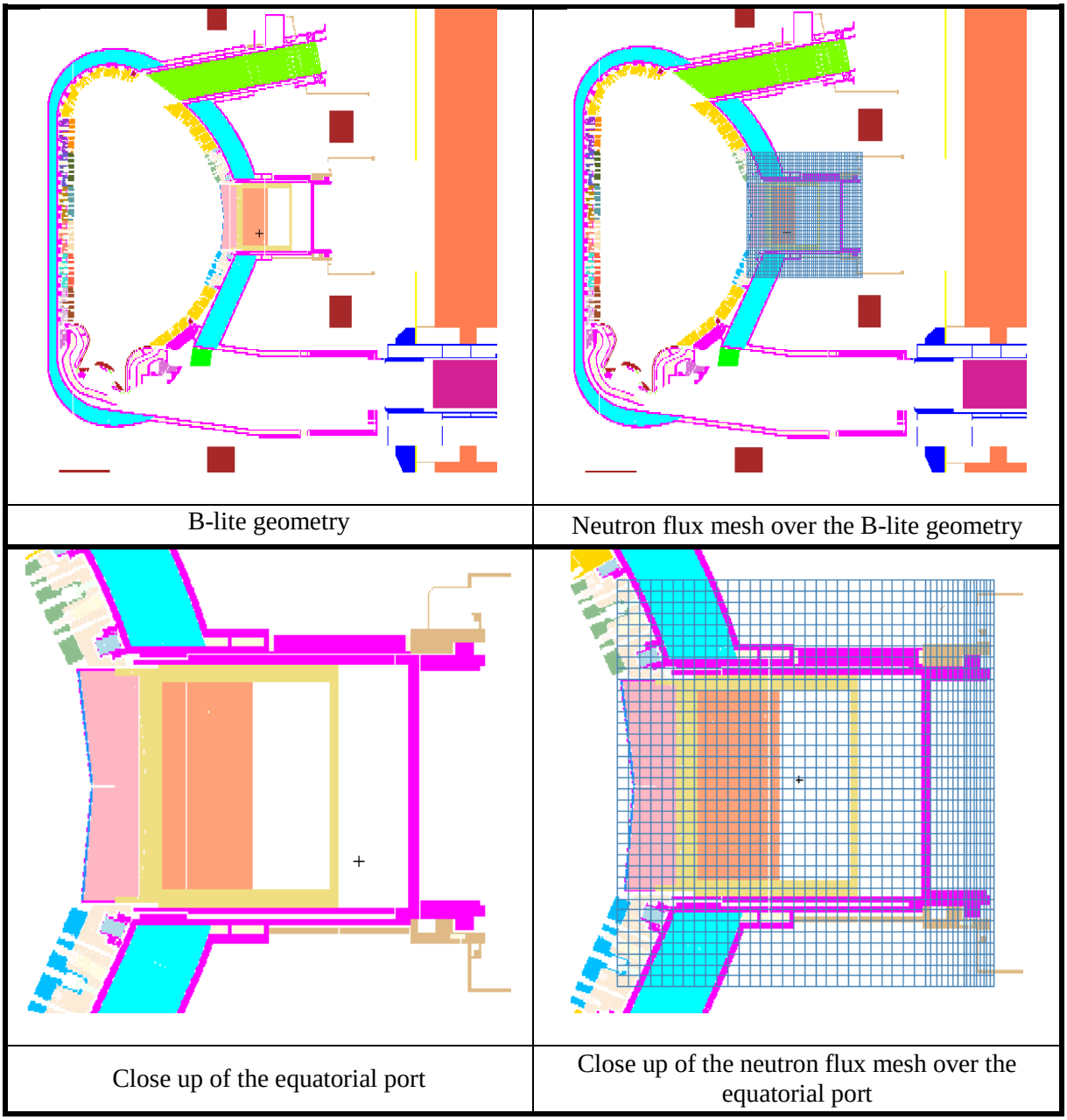

B-lite geometry	Neutron flux mesh over the B-lite geometry
Close up of the equatorial port	Close up of the neutron flux mesh over the equatorial port

Figure 5-5 Neutron transport mesh for the SDR calculations over the equatorial port of the ITER B-lite model, Y=0

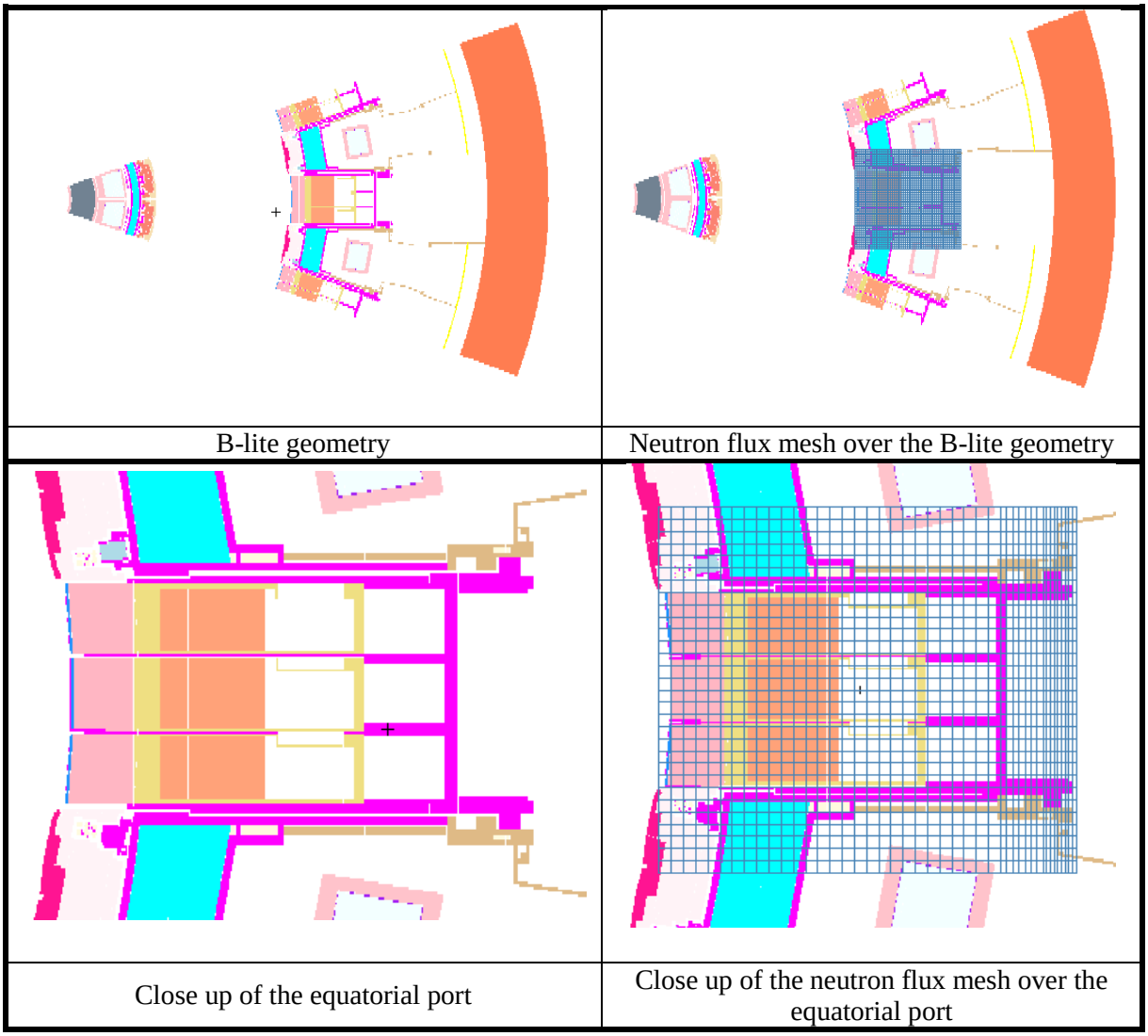

Figure 5-6 Neutron transport mesh for the SDR calculations over the equatorial port of the ITER B-lite model, Z=0

The decay gamma source was calculated for a cooling time of ~12 days (10^6 s) after the ITER SA-2 irradiation scenario [56], summarized in Table 5-3. The materials activated to obtain the source can be seen in Figure 5-7; indicating the regions inside the port (including the frame) and the bellows that are activated. A dummy port plug featuring a shield made of a stainless steel and water mixture is placed in the port (M70).

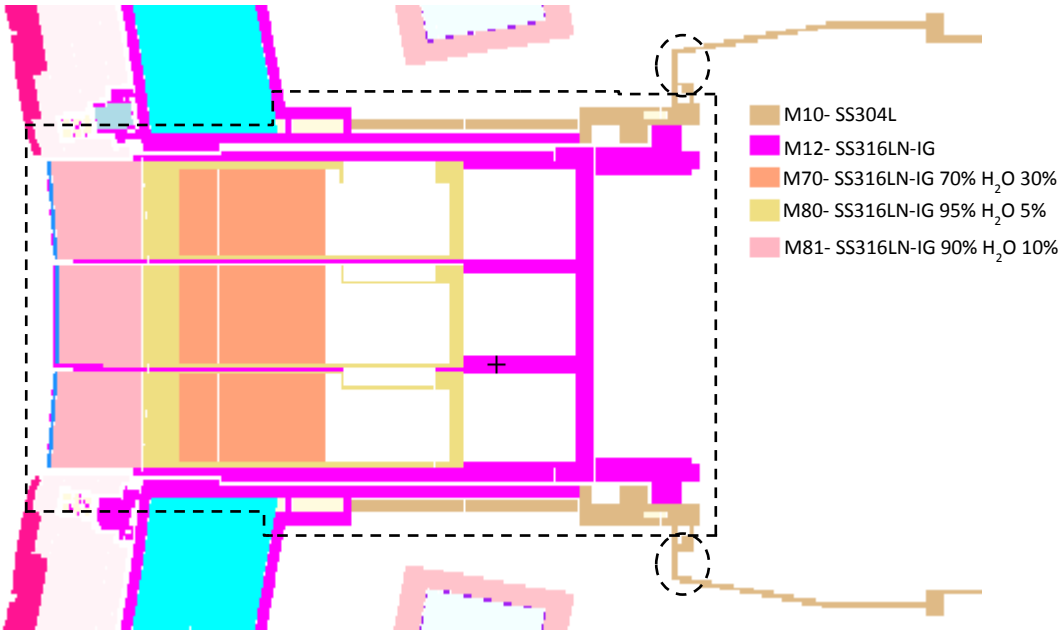

Figure 5-7 Materials and regions activated to obtain the photon source

Table 5-3 Definiton of the SA2 irradiation scenario

Fusion power (MW)	Duration	Repetitions
2.68	2 years	1
20.6	10 years	1
0	0.667 years	1
41.5	1.33 years	1
0	3920 seconds	17
500	400 seconds	
0	3920 seconds	4
700	400 seconds	

For the evaluation of the SDR map, a second 6 x 6 x 10 cm^3 mesh is defined over the port (Figure 5-8). The SDR has also been calculated defining an additional mesh tally (tally R1) in the Port Interspace (behind the port plug); it can be seen in Figure 5-9. This is a standard tally used for SDR calculations; it is defined as a single voxel with 30 x 240 x

272 cm^3. To calculate the dose, the flux-to dose conversion coefficient factors for biological dose rates recommended by ITER have been used [57].

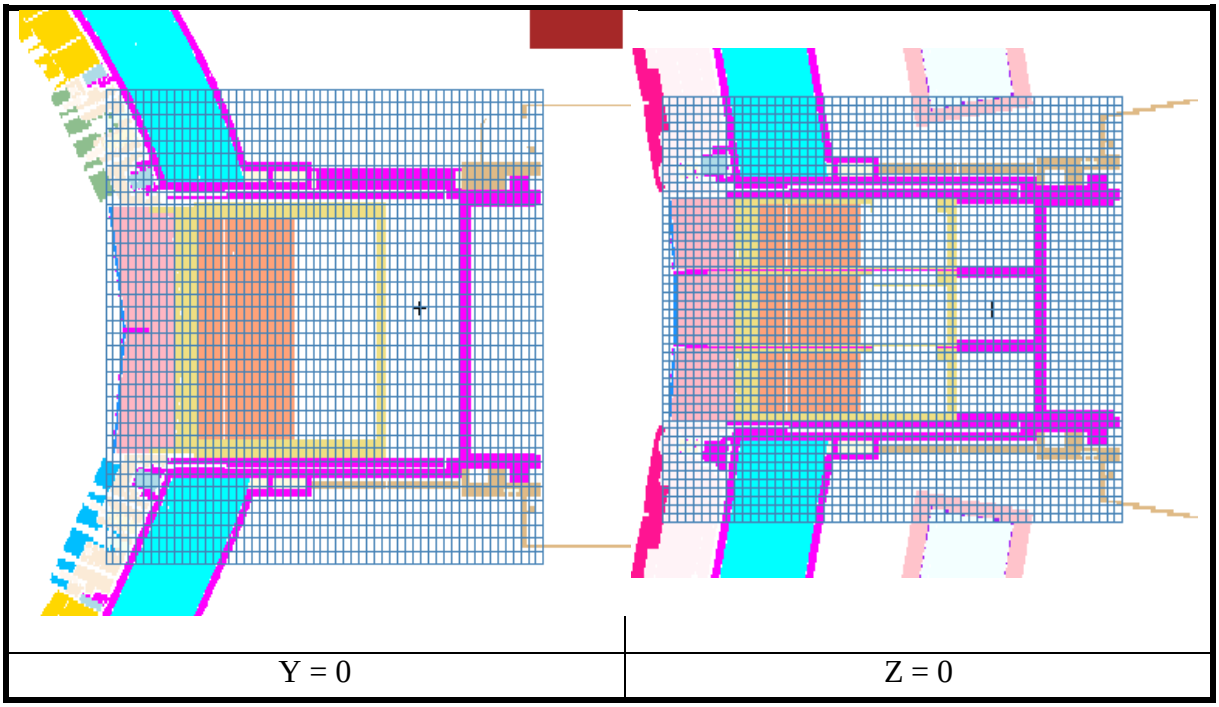

Figure 5-8 Mesh used for tallying the decay gamma in the SDR calculations over the equatorial port of the ITER B-lite model

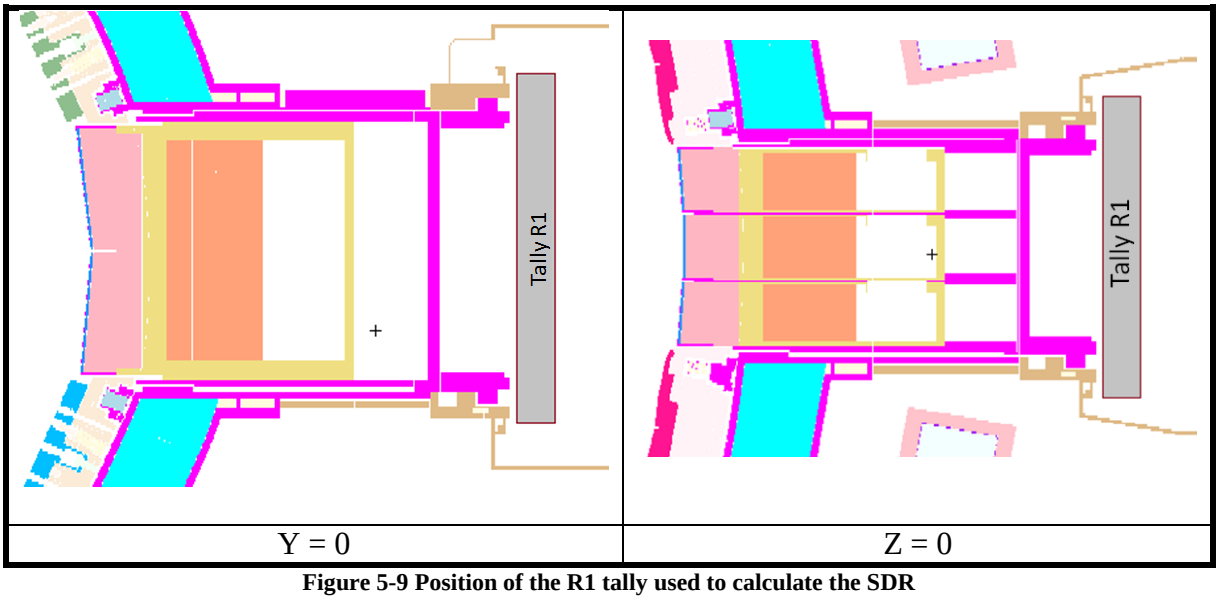

Figure 5-9 Position of the R1 tally used to calculate the SDR

As with the previous calculations, the neutron transport has been made using the R2S-UNED (based on the MCNP5 v1.6 transport code) and the FENDL-2.1 cross section library; in this case, to calculate the neutron spectra, the VITAMIN-J 175 energy structure is used. For the activation calculations the ACAB code was used with the EAF-2007 nuclear data library [58]. Lastly, for the photon transport the R2S-UNED code was used with the MCPLIB84 cross section library [50].

5.2.2. Results and discussion

In this case, the target CPU time was taken so that a reliable average error (under 5%) in the neutron flux could be obtained using, at least, one of the two maps. Approximately $5 \cdot 10^3$ CPU hours achieved this goal in both of the maps, hence this was the time settled for this step. Using the **HD_F** weight map required $8.6 \cdot 10^8$ source histories, whereas for the **SQRT_F** map $1.8 \cdot 10^9$ source histories were needed. Both techniques performed similarly in terms of FOM and average error as can be seen in Table 5-4. This comparable outcome is expected since the sum of the source particles and the total number of tracks created by WW is alike in both cases.

Table 5-4 Comparison of the neutron transport statistics in the ITER B-lite equatorial port using global GVR meshes

	NPS	CPU hours	Percentage of voxels not scoring (%)	Average error (%)	FOM	Total WW tracks
HD_F	8.6E+08	5.1E+03	0	2.5	2.4E-03	4.8E+09
SQRT	1.8E+09	5.4E+03	0	2.5	2.9E-03	4.1E+09

The relative error distributions are shown in Figure 5-10, it shows how not all of the voxels have relative error under 0.1. This happened despite having defined a mesh with

dimensions of 10 x 10 cm^2 in the *y* and *z* directions (to improve sampling through the voxels). To further observe which parts of the geometry have the worst statistics, neutron flux maps and their relative errors are shown at Z=0 in Figure 5-11.

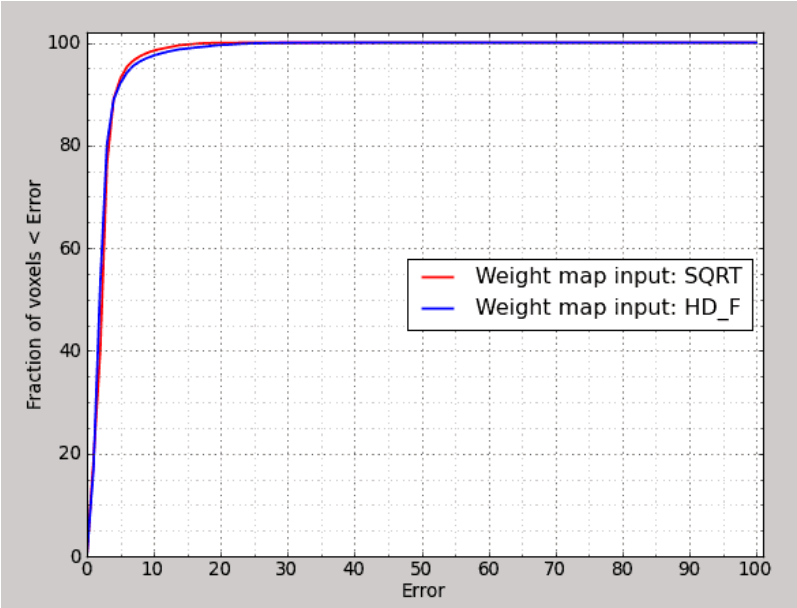

Figure 5-10 Relative error distribution of the neutron flux mesh tallies defined over the equatorial port in the ITER B-lite model

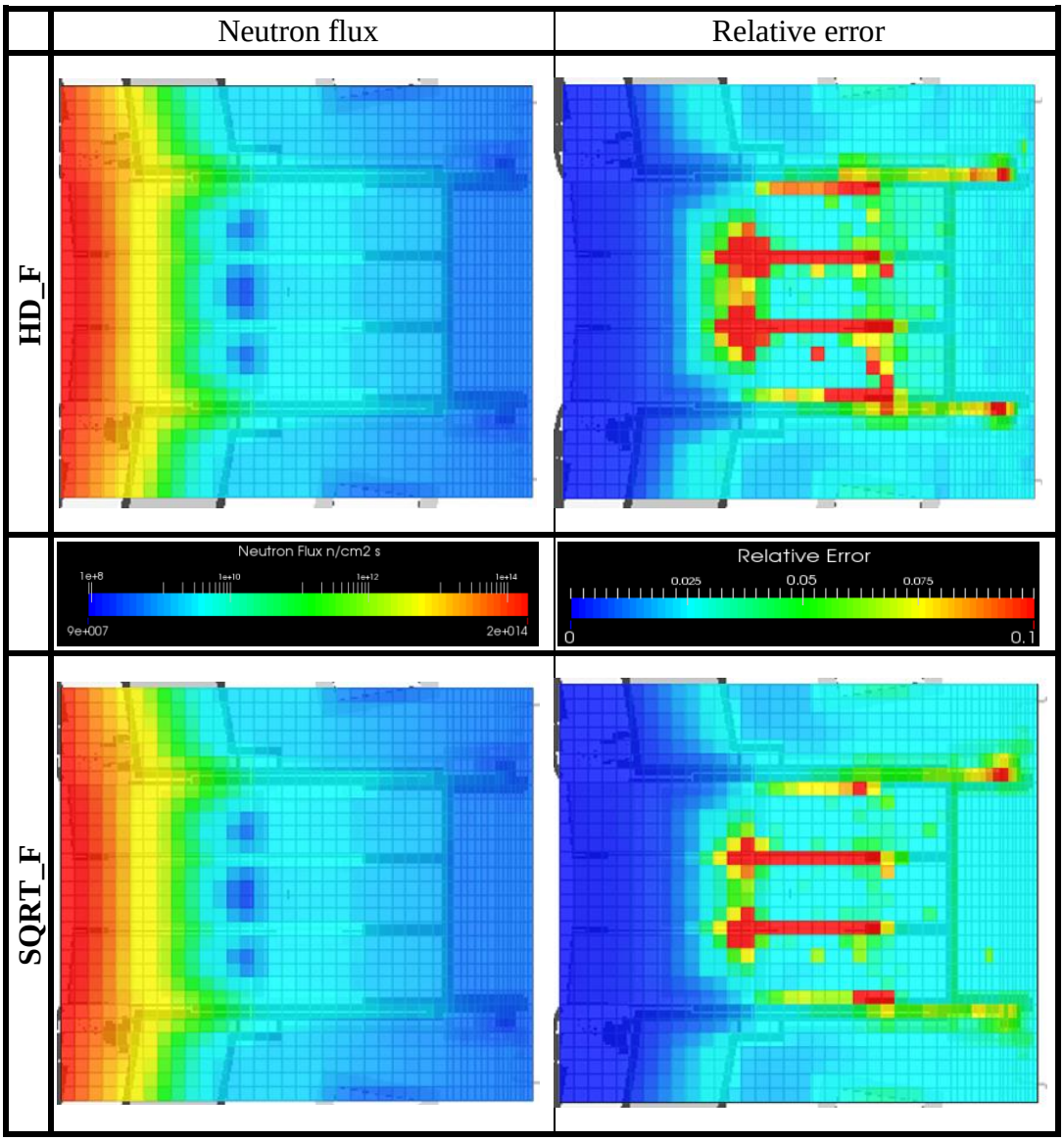

Figure 5-11 Neutron flux and relative error over the equatorial port of the ITER B-lite model using the HD_F (top) and SQRT_F (bottom) global weight maps, Z = 0

In Figure 5-11, it can be seen how relative errors over 0.1 appear at the gaps present in the frame. Slightly better sampling of the apertures occurred using the **SQRT_F** weight map; due to this map having over twice as much source histories, compared to the **HD_F** weight map. Figure 5-12 shows the neutron flux and relative errors through one of the gaps at Y=86. At the back of the port, where activation of the materials gives the most contribution to the SDR at the selected tally, the neutron flux shows relative errors over 0.1.

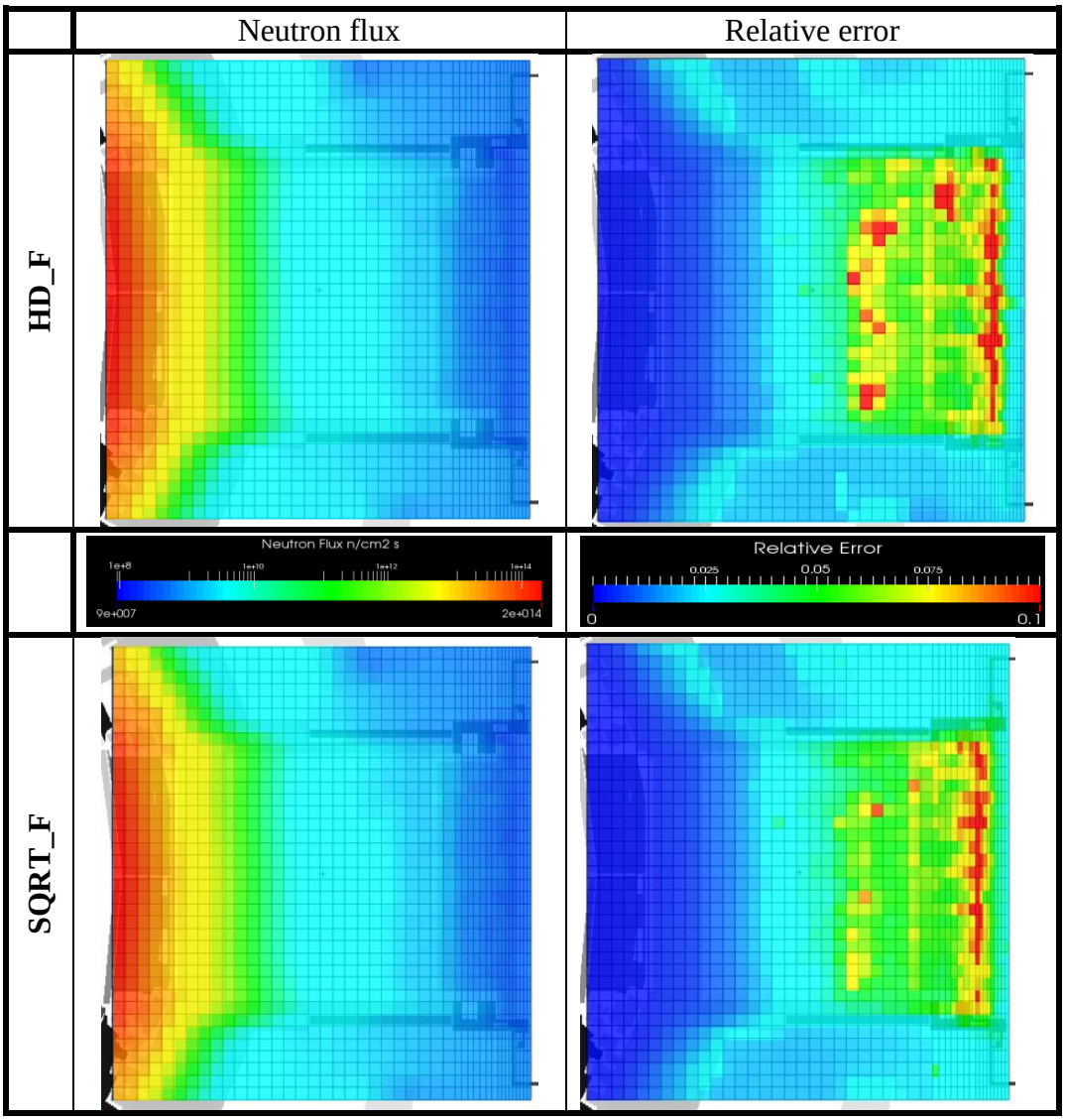

Figure 5-12 Neutron flux and relative error in the gap at Y=86 using the HD_F (top) and SQRT_F (bottom) weight maps

Located at X=1118 is the rear plate of the port, made of 316LN-IG stainless steel. A close up of the neutron flux and relative errors at this location is shown in Figure 5-13; where it can be seen that the worst results appear around the top and bottom gaps (with relative errors over 0.1).

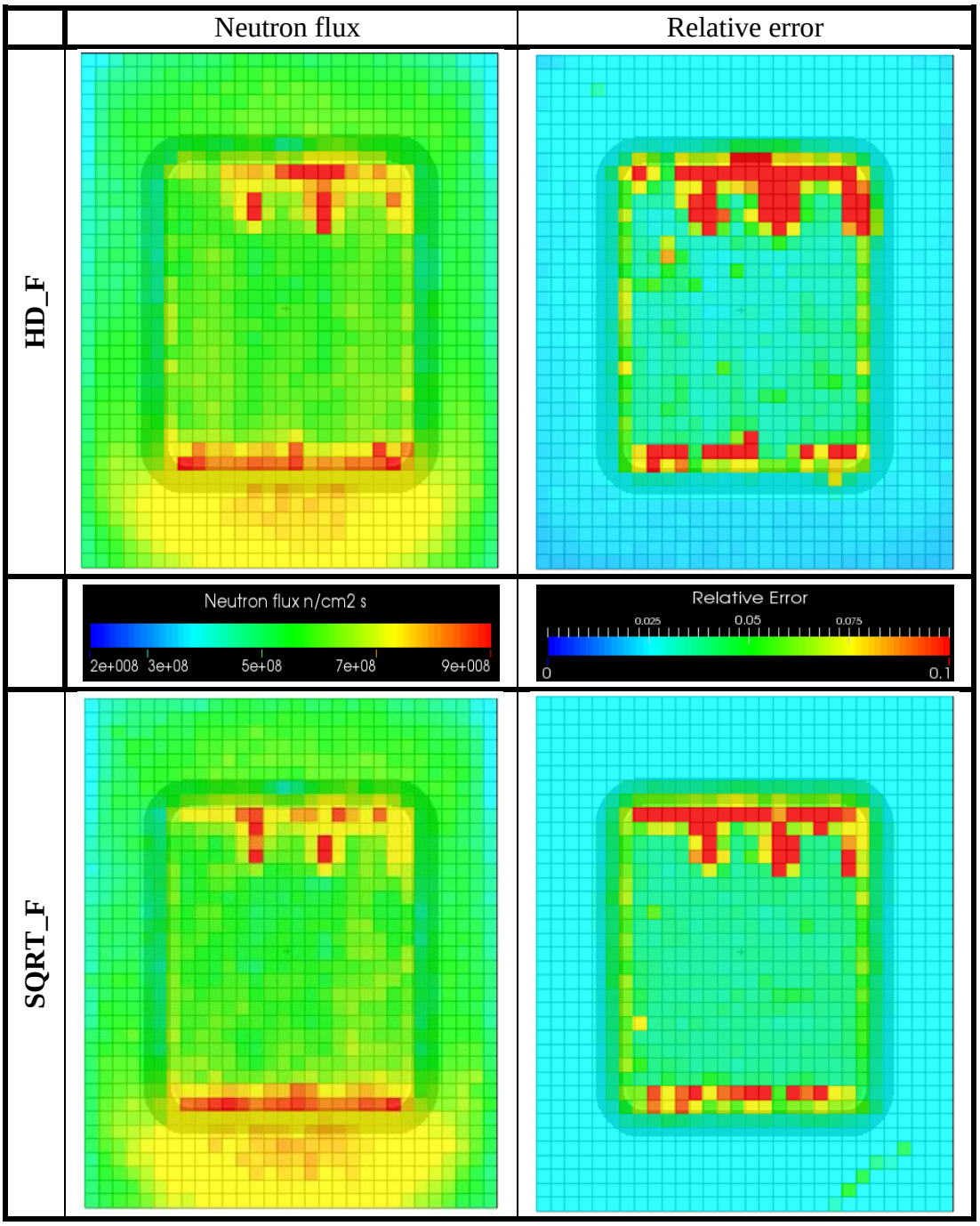

Figure 5-13 Neutron flux and relative error in the rear plate at X = 1118 using the HD_F (top) and SQRT_F (bottom) weight maps

Additionally, the neutron flux spectra at four voxels inside the mesh are compared. Figure 5-14 shows the location and coordinates of the center of the voxels: i) A is located in the center of the mesh, ii) B is on the back plate, iii) C is at the center but over the side frame, and iv) D is over the side frame at the back, close to the R1 tally. Figure 5-15,

Figure 5-16, Figure 5-17, and Figure 5-18 show the neutron flux spectrum at voxels A, B, C, and D, respectively.

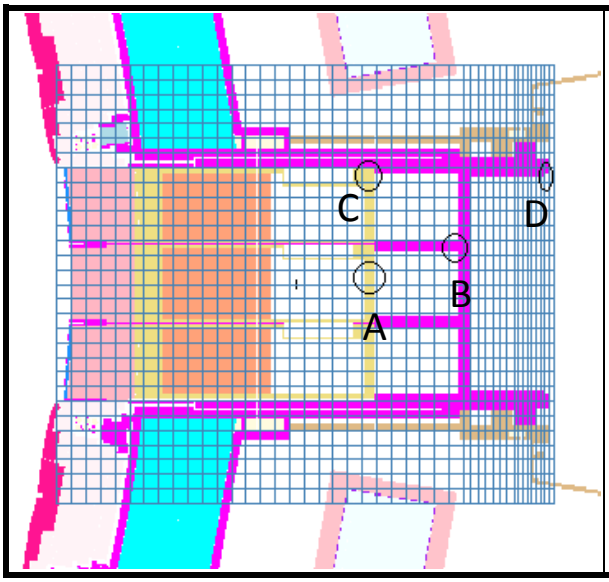

	x coord.	*y* coord.	*z* coord.
A	1050	5	5
B	1110	25	5
C	1050	75	5
D	1172.5	75	5

Figure 5-14 Location and coordinates of voxels A, B, C, and D

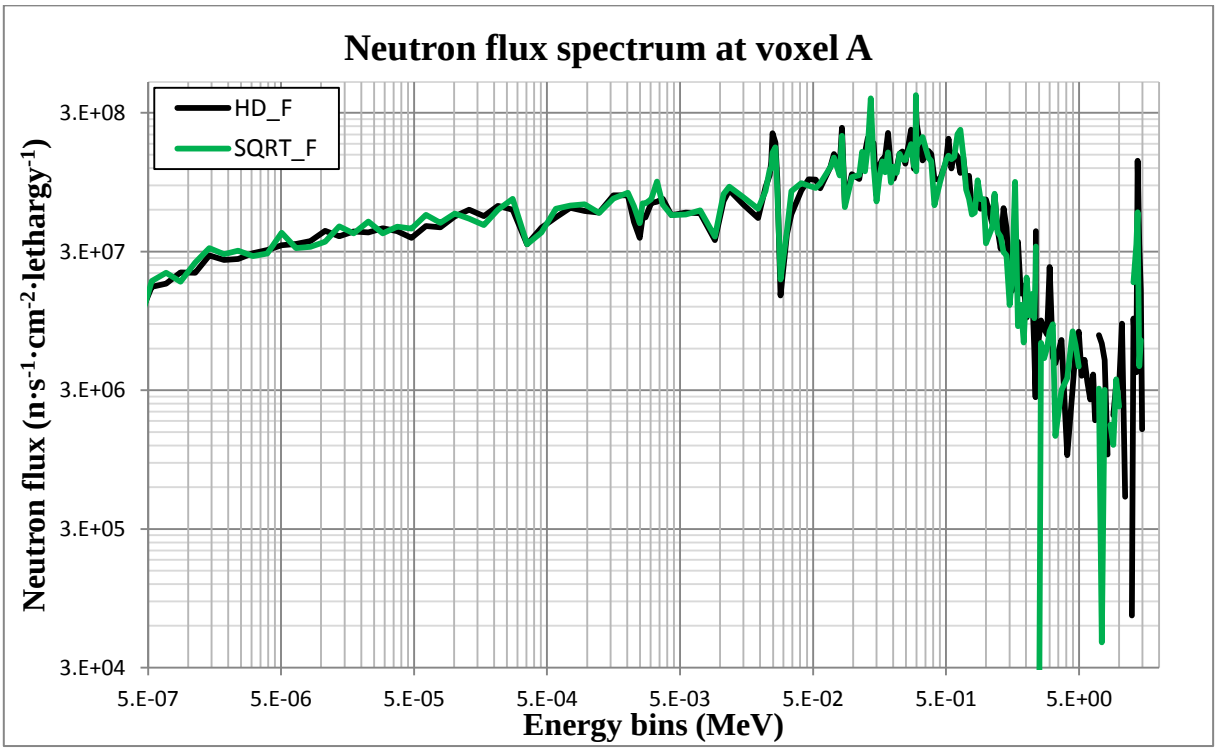

Figure 5-15 Neutron flux spectrum at voxel A

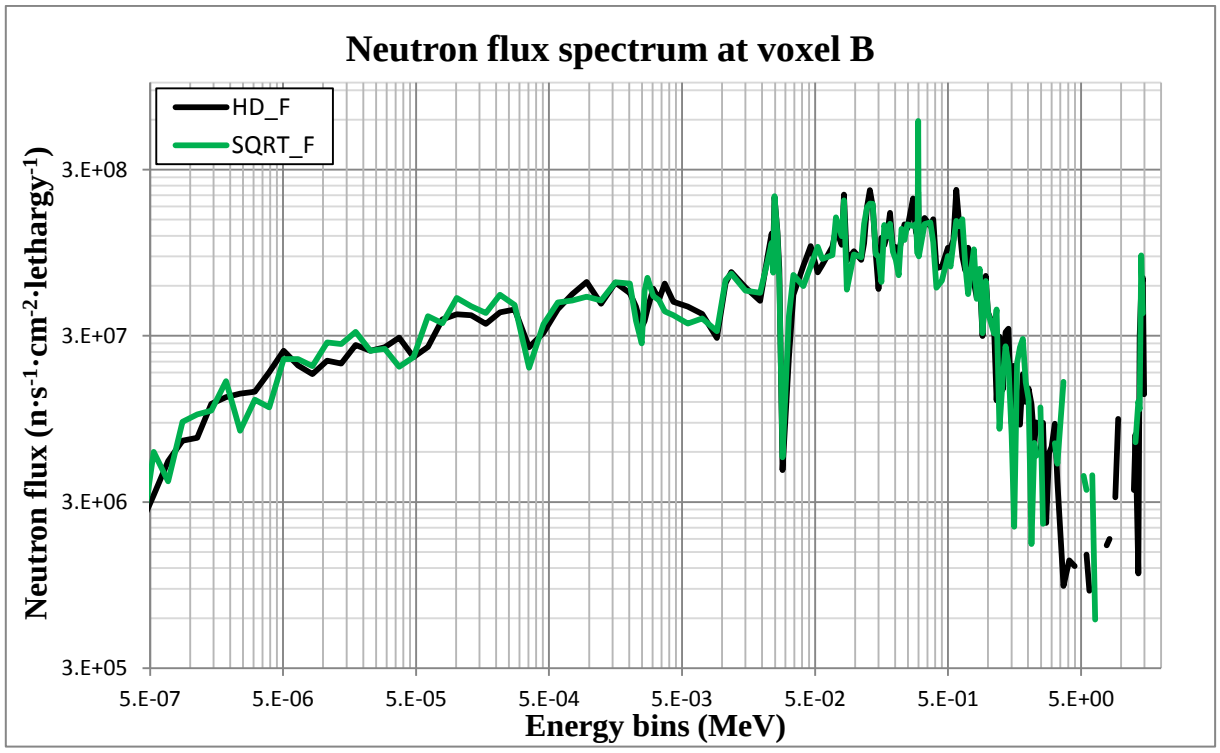

Figure 5-16 Neutron flux spectrum at voxel B

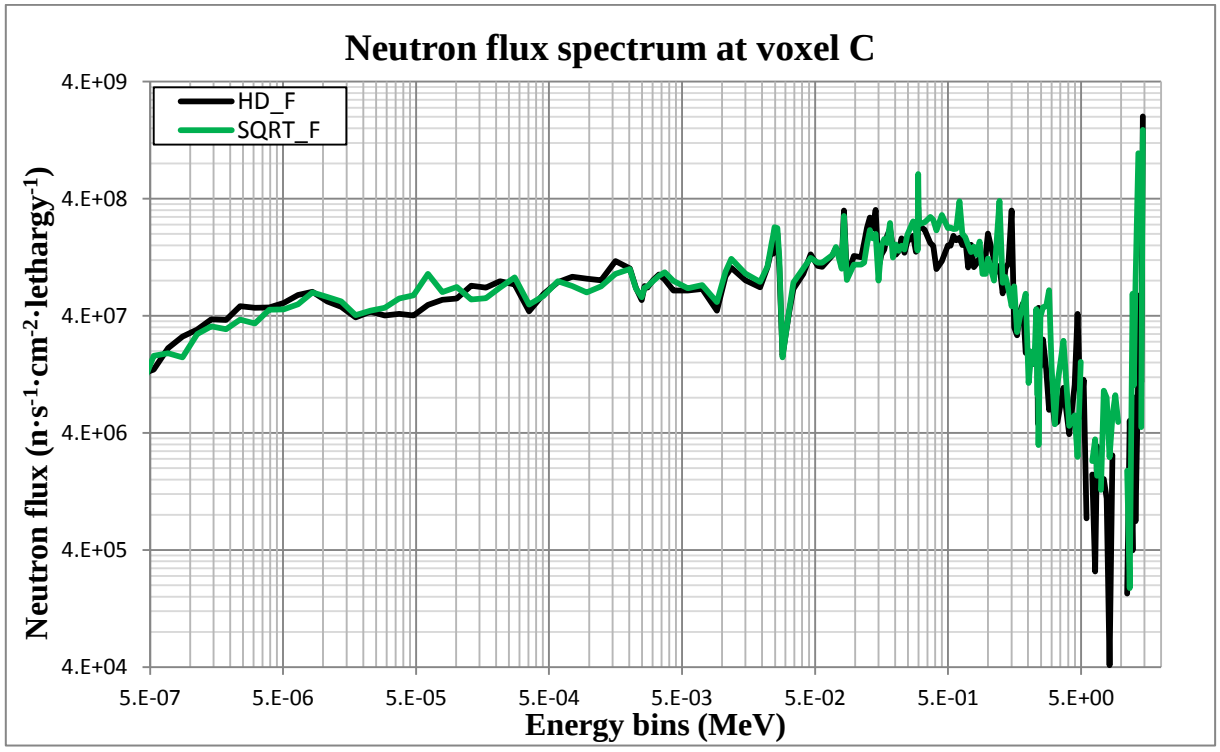

Figure 5-17 Neutron flux spectrum at voxel C

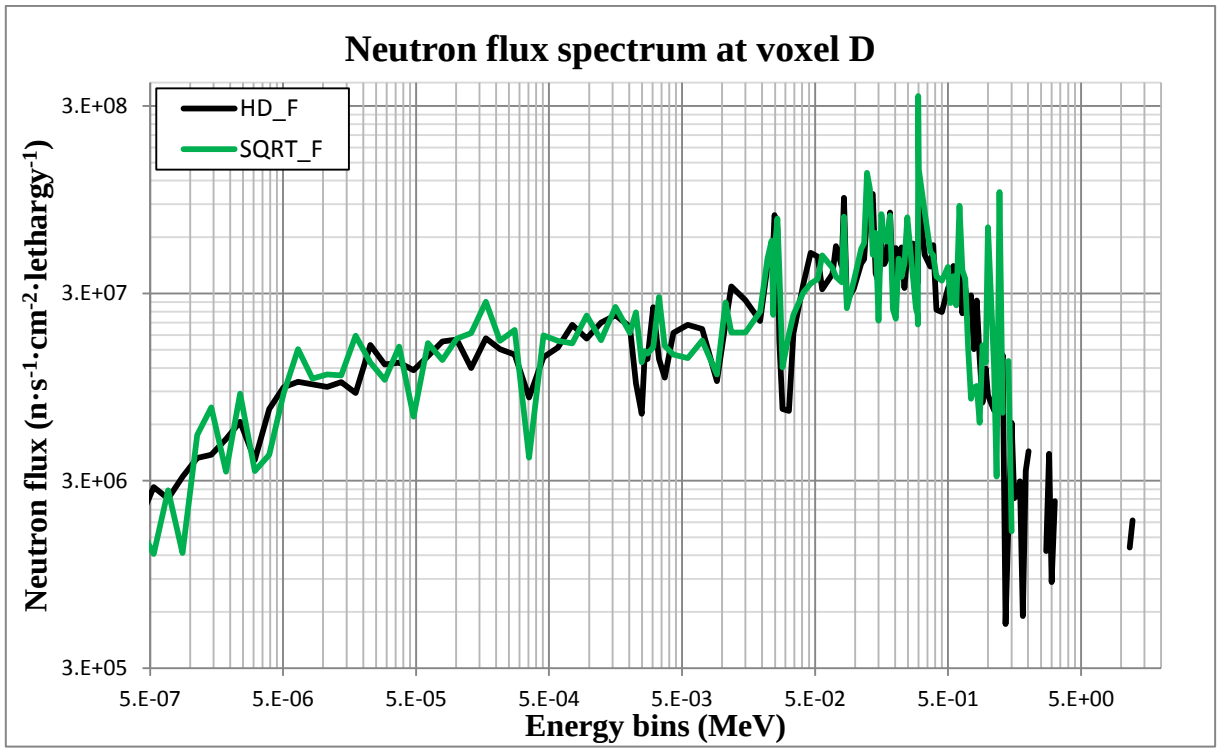

Figure 5-18 Neutron flux spectrum at voxel D

Voxel A, which is closer to the source, shows minimal differences between the spectra obtained using the **SQRT_F** weight map and the **HD_F** map. While in voxels B, C, and D some differences in the fluxes can be seen, although these differences are minimal and scattered (i.e., differences over a factor of 1.5 appear only at a few points).

Taking voxel C as a reference, further comparisons can be made. For this voxel, the total contact dose rate 10^6 s after shutdown and the five isotopes contributing the most are given in Table 5-5.

Table 5-5 Comparison of the total contact dose and principal isotopes contributors after 10^6 s shutdown

HD_F	Contact dose rate (Sv/h)	SQRT_F	Contact dose rate (Sv/h)
TOTAL	5.72E-01	**TOTAL**	6.16E-01
CO 60	3.72E-01	**CO 60**	3.99E-01
TA182	1.36E-01	**TA182**	1.63E-01
FE 59	2.41E-02	**FE 59**	2.53E-02
CO 58	2.33E-02	**CO 58**	1.56E-02
MN 54	7.65E-03	**CR 51**	6.05E-03

In Table 5-5, it can be seen how a difference of ~7% in the total contact dose is found. The major contributors to this dose are Co60 and Ta182, which account ~65% and ~25% respectively. Using the **SQRT_F** weight map, the Co60 contact dose is ~6% higher than the contact dose obtained using the **HD_F** map for the same isotope. However, this difference is even bigger for the Ta182, which contact dose is over 16% using the **SQRT_F** weight map compared to the **HD_F** map. In

Table 5-6, the concentration of these isotopes is given 10^6 s after shutdown, with the fluxes from both maps; in which the differences of concentrations for Co60 and Ta182 is of ~6% and ~12%, respectively.

Table 5-6 Comparison of the concentrations of the principal isotopes contributing to the contact dose after 10^6 s shutdown

HD_F	Concentration (g/cc)	SQRT_F	Concentration (g/cc)
CO 60	1.21E-02	**CO 60**	1.29E-02
TA182	1.80E-03	**TA182**	2.05E-03
FE 59	4.00E-05	**FE 59**	4.15E-05
CO 58	7.12E-05	**CO 58**	5.15E-05
MN 54	9.81E-05	**MN 54**	6.16E-05
CR 51	2.46E-04	**CR 51**	2.69E-04

To better understand the scope of these differences in the neutron flux, the next steps towards obtaining the SDR are analyzed. The spatial distribution of the photon sources at 10^6 s after shutdown is shown at Y = 0 in Figure 5-19.

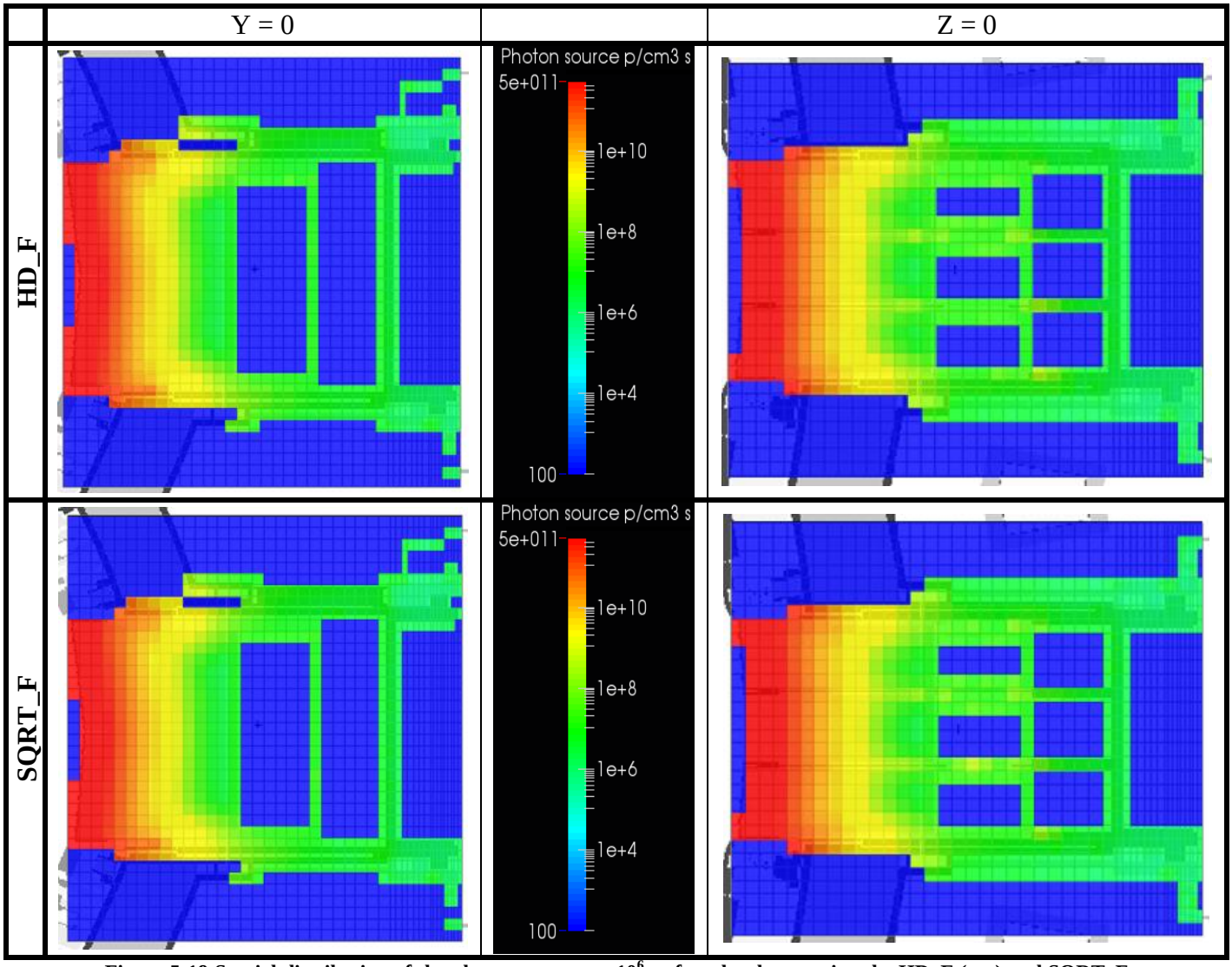

Figure 5-19 Spatial distribution of the photon sources at 10^6 s after shutdown, using the HD_F (top) and SQRT_F (botton) weight maps for the neutron transport, at Y=0 and Z=0

To obtain a better comparison, the differences of the spectrum in the photon source after 10^6 s shutdown at the four A, B, C, and D voxels are shown in Figure 5-20, Figure 5-21, Figure 5-22, and Figure 5-23.

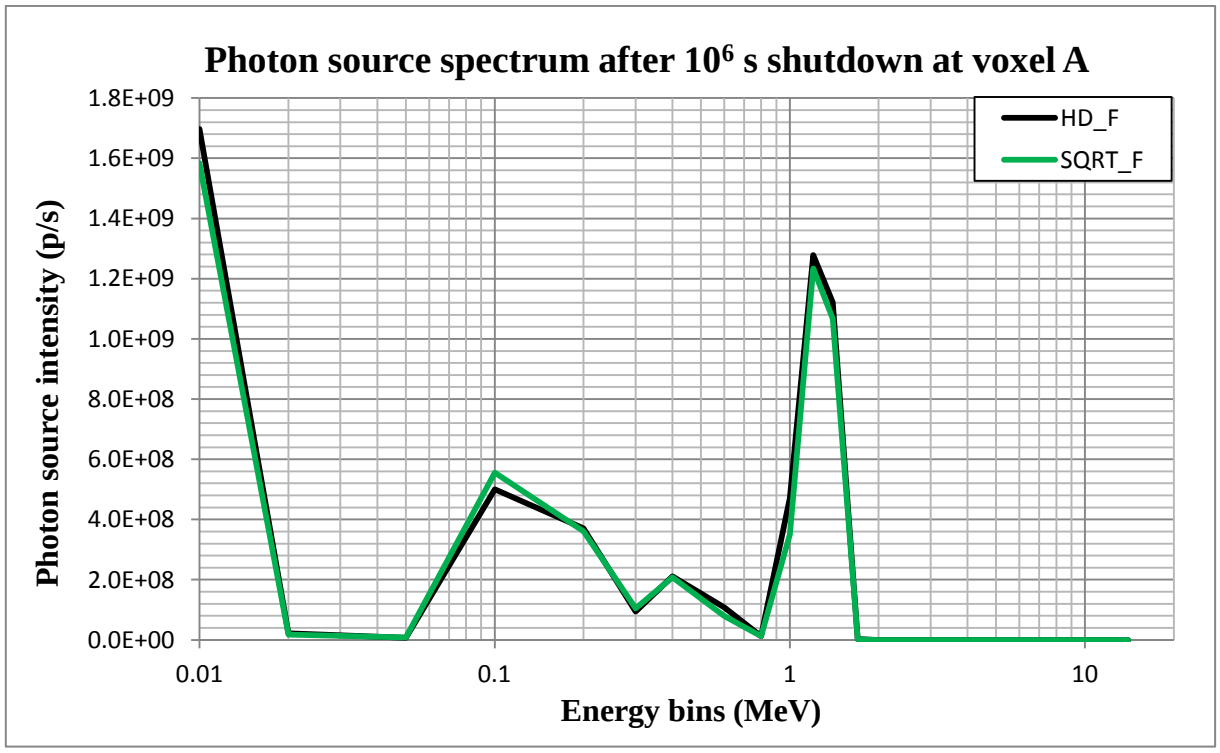

Figure 5-20 Photon source spectrum after 10^6 s shutdown at voxel A

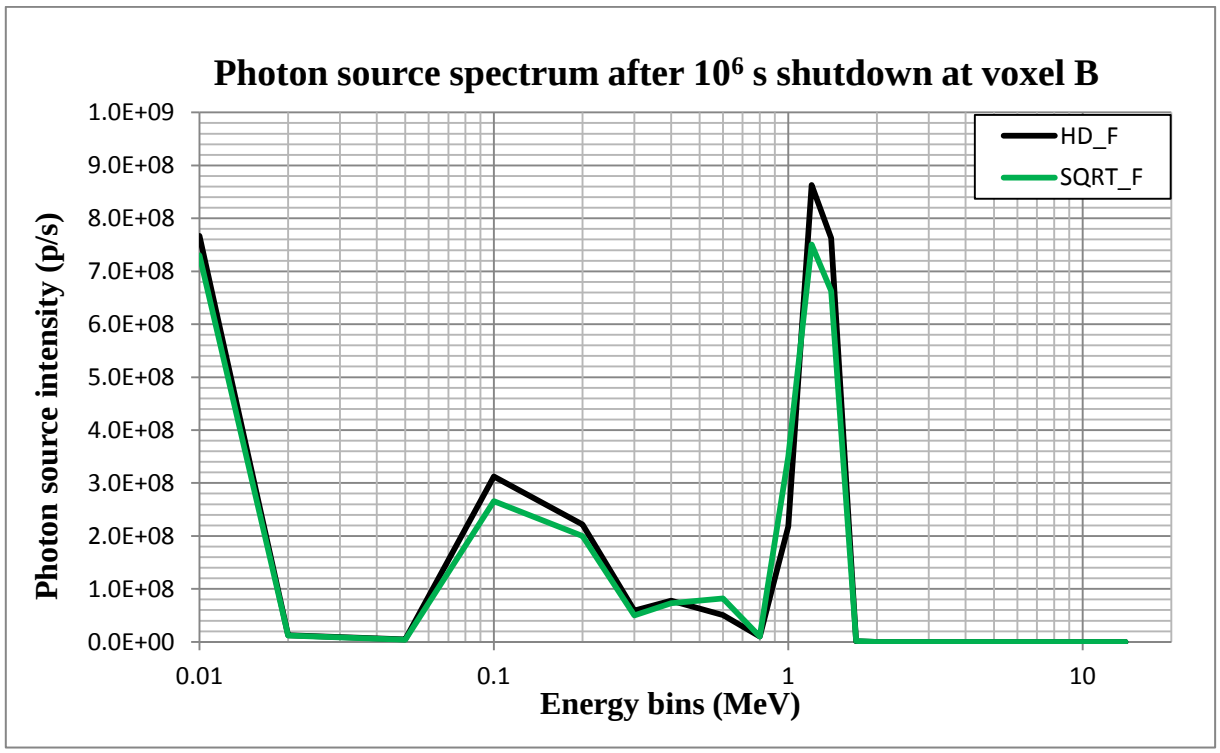

Figure 5-21 Photon source spectrum after 106 s shutdown at voxel B

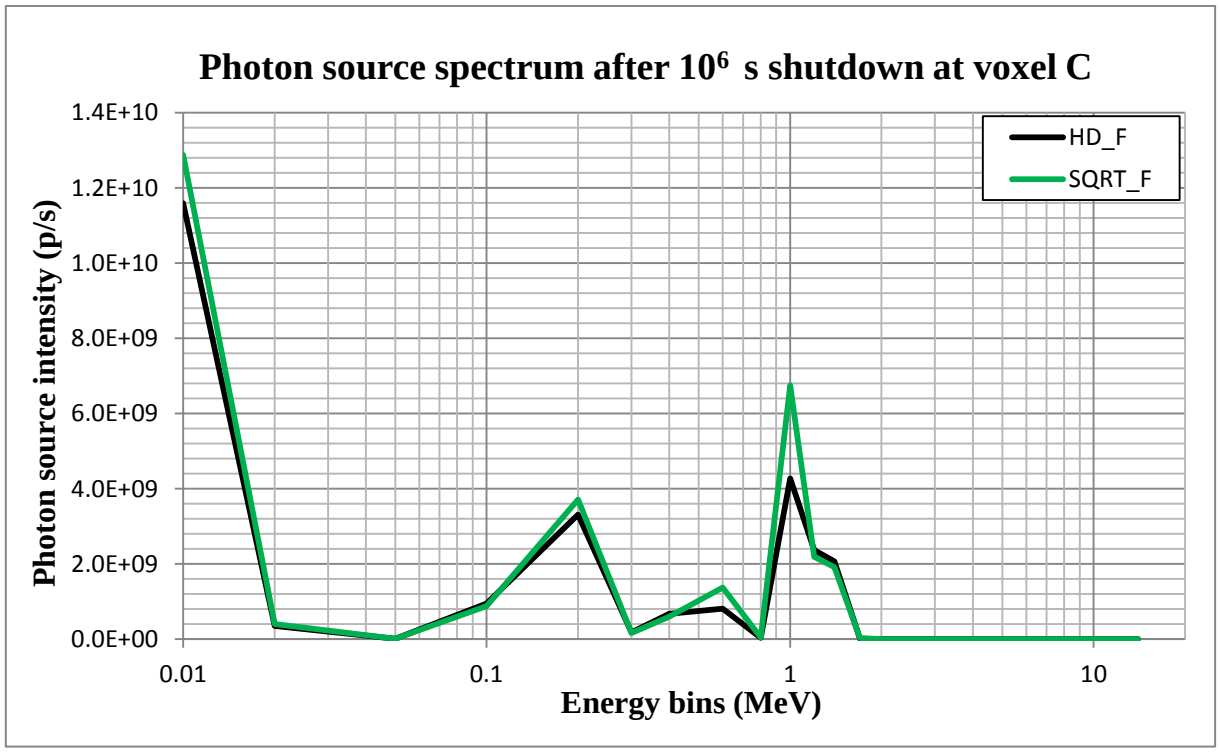

Figure 5-22 Photon source spectrum after 10^6 s shutdown at voxel C

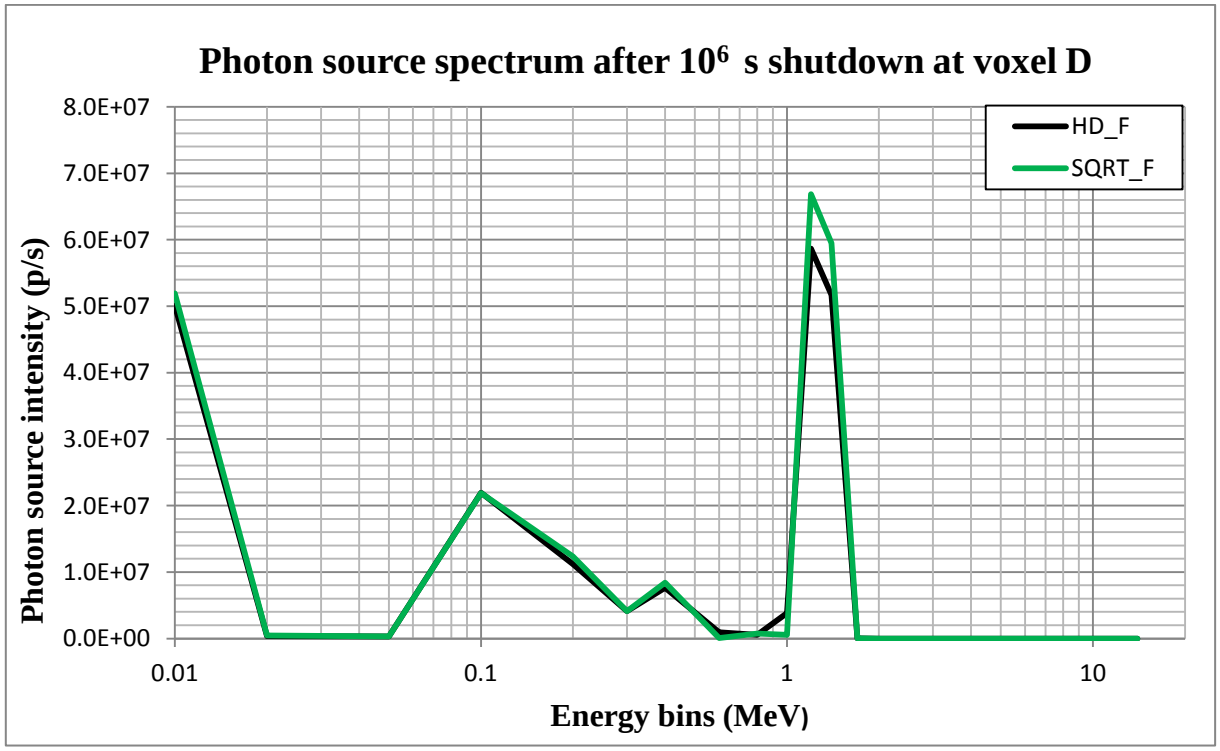

Figure 5-23 Photon source spectrum after 10^6 s shutdown at voxel D

The graphs show how the intensity of the photon source is higher for the neutron flux obtained with the **SQRT_F** weight maps at voxels over the side frame, C and D, in which slightly better sampling of the gaps was observed at Figure 5-12. This difference is as high as ~30% in point C for ~1 MeV gammas, but it lowers to ~12% at point D (in the rear part of the frame, due to the doglegs present in the geometry). However, in voxel B, located at the back plate, source intensity is 13% higher for the **HD_F** approach in the same energy range of 1 MeV.

The photon transport was done using 10^9 source histories, and running time was $1.5 \cdot 10^2$ CPU hours for both cases. The decay gamma flux is shown at the port at Y=0 and Z=0 in Figure 5-24 and Figure 5-25. Contour lines indicating the SDR for 10^4 and 10^5 μSv/h are also shown. Additionally, the difference of the SDR maps (i.e., $\frac{2 \cdot |SDR_{HD\_F} - SDR_{SQRT\_F}|}{(SDR_{HD\_F} + SDR_{SQRT\_F}}$) is shown in Figure 5-26 where the higher relative errors can be seen through the gaps and at the end of them.

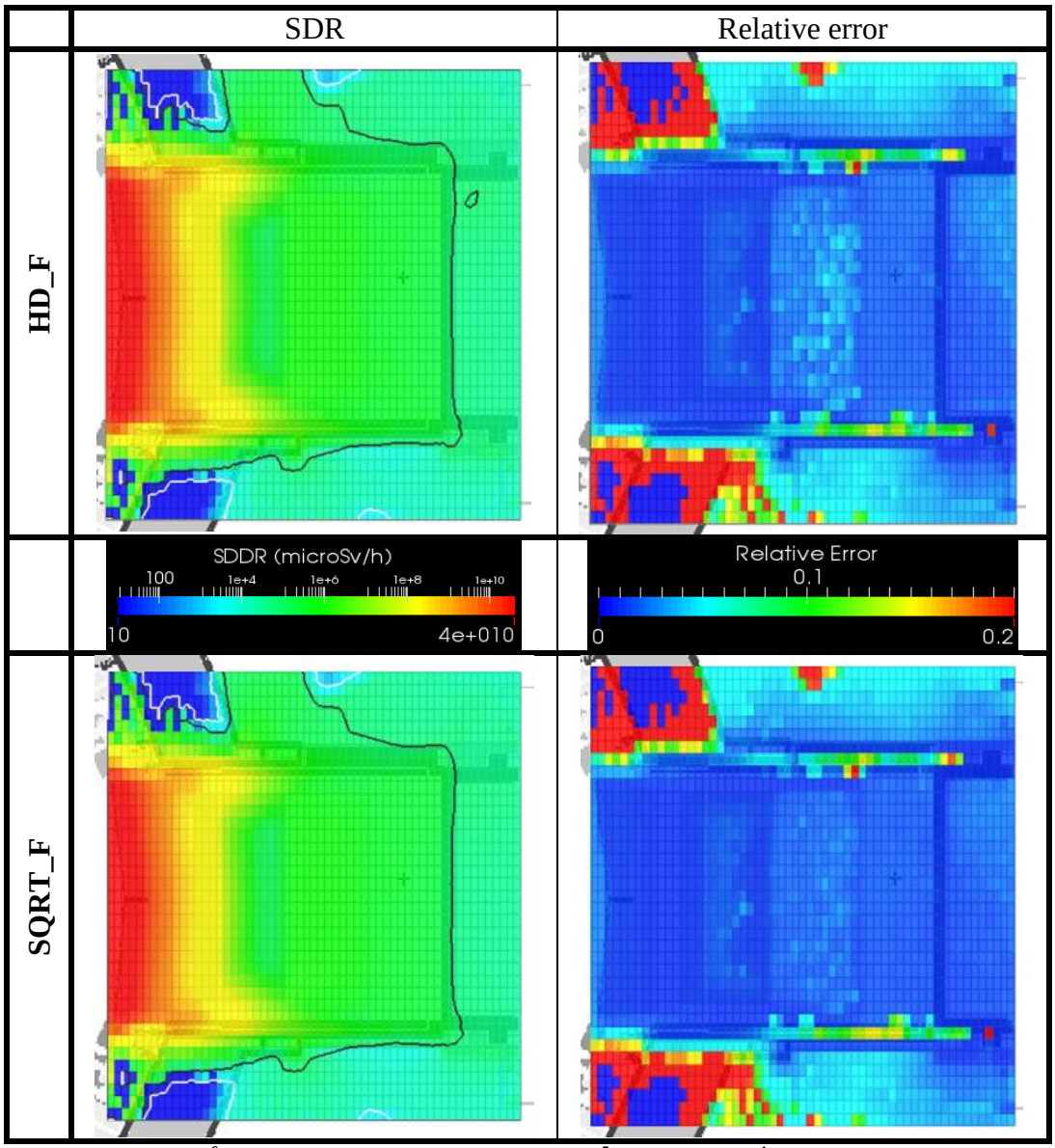

Figure 5-24 SDR after 10^6 s shutdown, showing contours over 10^5 (black) and 10^4 (white) μSv/h, and relative error maps; Y=0

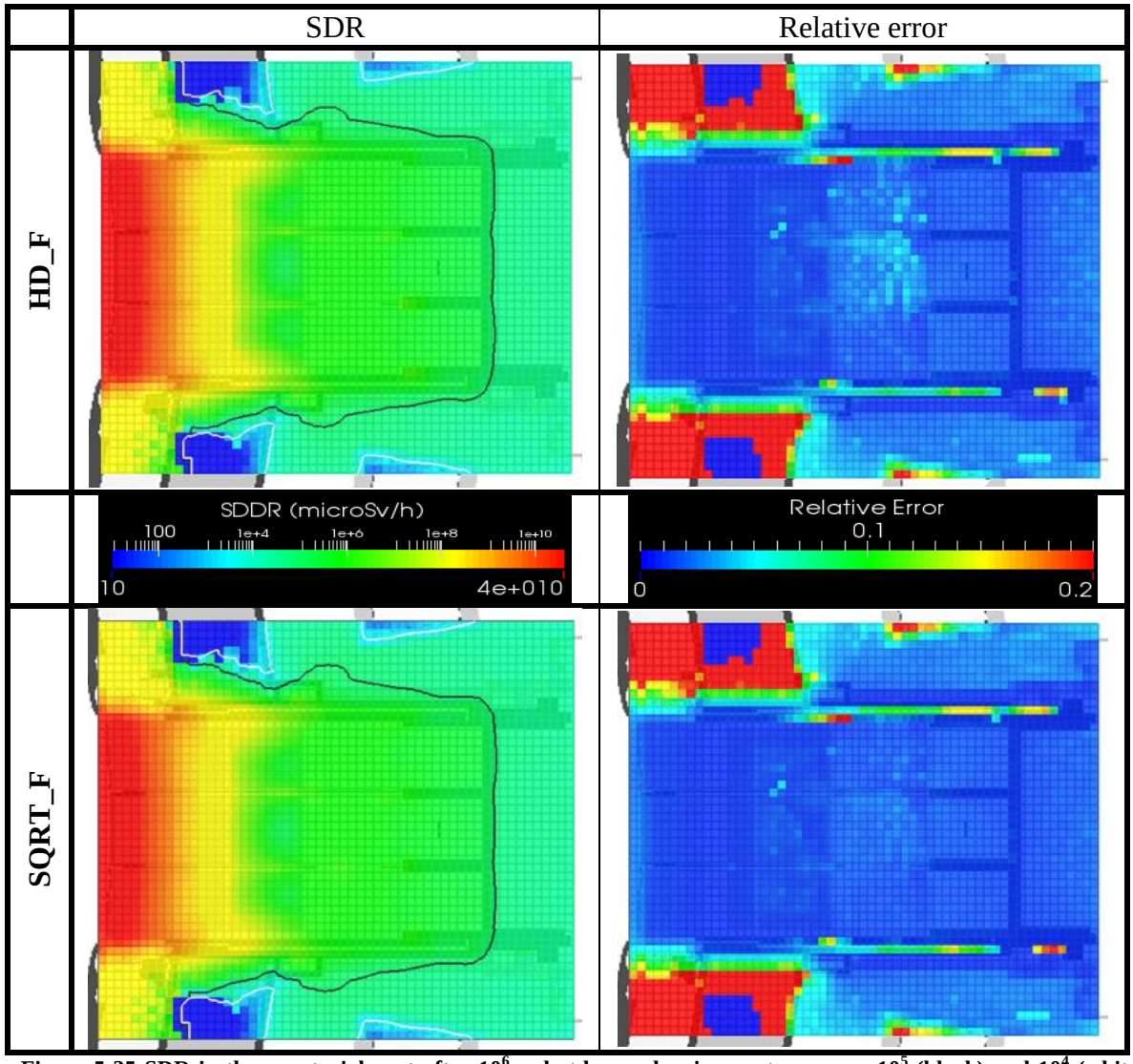

Figure 5-25 SDR in the equatorial port after 10^6 s shutdown, showing contours over 10^5 (black) and 10^4 (white) μSv/h, and relative error maps; Z=0

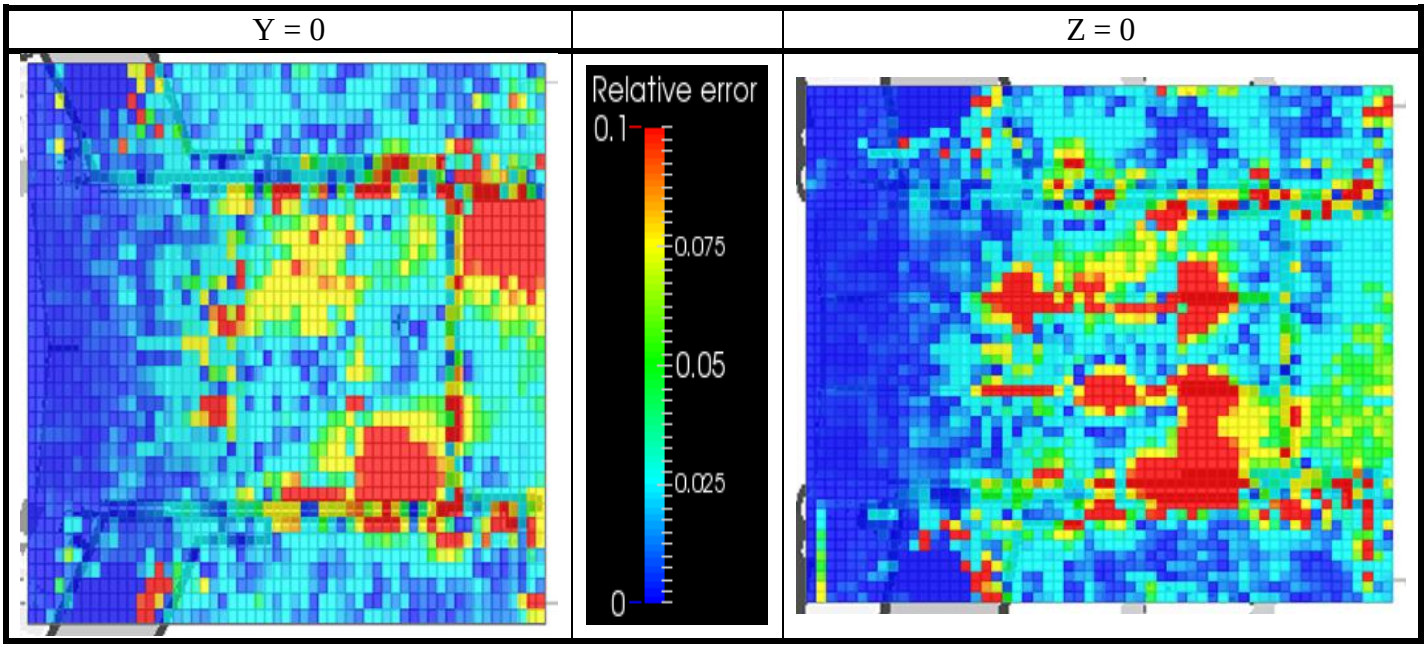

Figure 5-26 Relative error distribution between the SDR maps, at Y=0 and Z=0

The results calculated in the tally R1 are summarized in Table 5-7. It shows that the difference obtained between the tallies is approximately 3.5%, indicating similar performances when both GVR techniques for the neutron transport phase are used.

Table 5-7 SDR measured at tally R1

	μSv/h	**Relative Error**
HD_F	3.19E+04	0.00085
SQRT_F	3.08E+04	0.00074

Lastly, it is worth noting that the targeted SDR limit at the ITER reactor in the port interspace region (where the tally R1 is located), is under 100 μSv/h. In this study, in which a dummy port plug is used and only the interior of the port was activated, the dose in the port interspace is 2 orders of magnitude larger than specification limits; which shows the importance of proper shielding. To get a better idea of the dose obtained through the reactor due to the activation of the port, a global mesh showing also the SDR 10^6 s after shutdown

is presented in Figure 5-27; three contour lines now indicate doses of 10^4, 10^5, and 10^6 μSv/h.

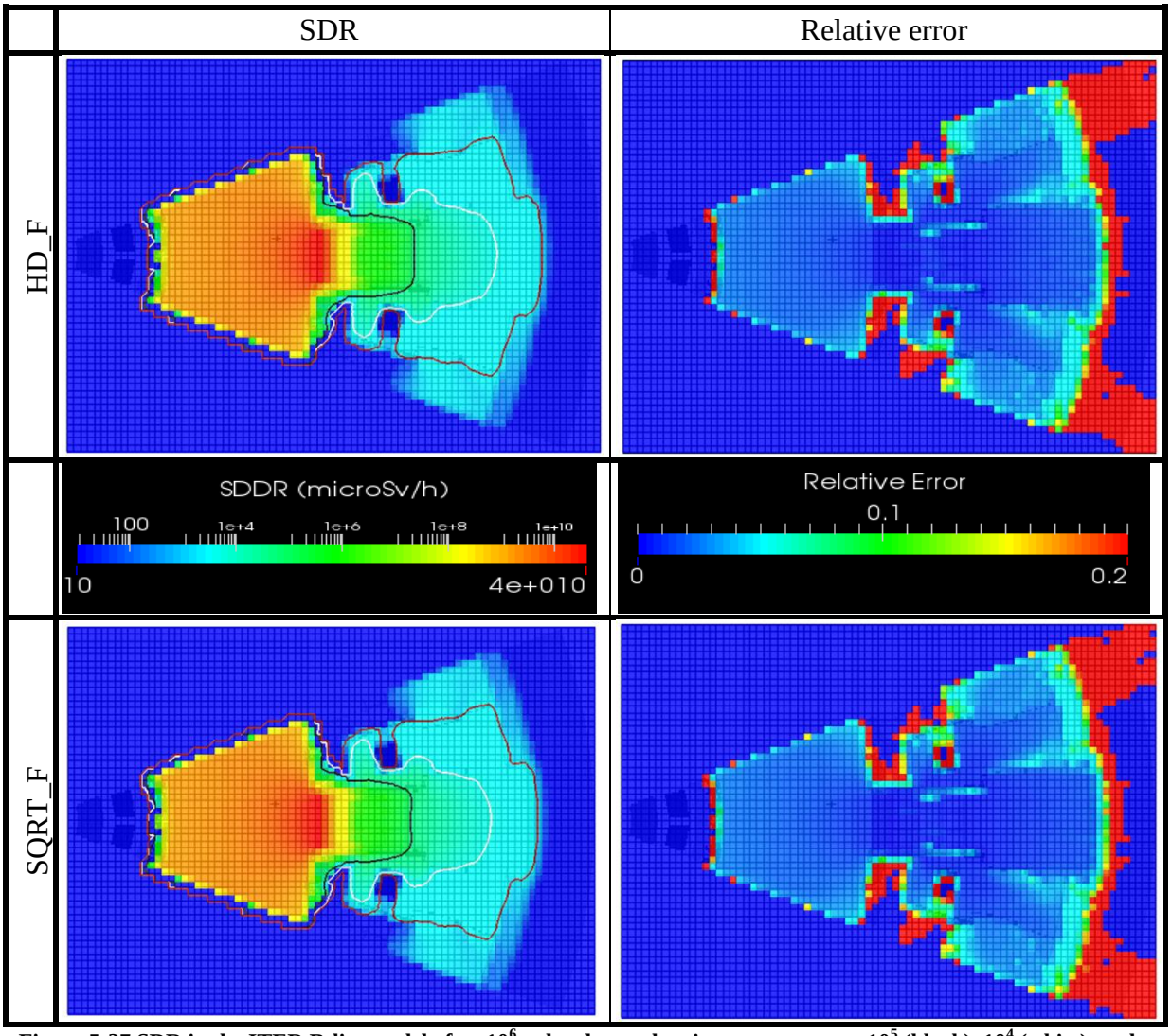

Figure 5-27 SDR in the ITER B-lite model after 10^6 s shutdown, showing contours over 10^5 (black), 10^4 (white), and 10^3 (red) μSv/h, and relative error maps; Z=0

5.2.3. Conclusions to the SDR calculations over the B-lite geometry

Comparison of results obtained for the neutron transport over a mesh covering the equatorial port of the ITER B-lite model, showed how both of the **HD_F** and **SQRT_F** global weight maps performed similarly at first sight. For the same computing time, equal average error and similar FOM was obtained. However, the **SQRT_F** weight map showed slightly better relative error for the neutron flux in the side gap regions.

Comparison of more detailed results over four different voxels inside the geometry, showed differences in regions close to streaming paths present in the frame. In particular, the neutron flux presents differences of up to an order of magnitude; which leads to differences in the contact dose rate of approximately 7% in this point.

The defined photon source was also compared in the four voxels of the geometry, showing differences in the points located over the frame, close to the side gaps. This difference is higher towards the center region of the port (~36%) for 1 MeV gammas, and diminishes towards the end of the gap.

Photon transport achieved comparable results for the same source histories and CPU time. The SDR after 10^6 s shutdown at the defined R1 tally, located at the back of the mesh, showed a difference of ~3.5%, indicating consistency of the results using either the **SQRT_F** or **HD_F** weight maps for the neutron transport.

6. Conclusions and future work

In this last chapter, the most relevant aspects of this work are reviewed. First the results obtained of the applications are summarized. Recommendations for future work are given next.

6.1. Conclusions

The main purpose of this work was to implement a purely stochastic GVR methodology, suitable for the large and complex geometry of a fusion reactor. The unavailability of open access existing codes and search of independency from deterministic calculations have been the principal motivations.

As a starting point, van Wijk's algorithms were used. These techniques create weight maps, which are proportional to the forward scalar flux or the relative errors, setting the Monte Carlo particle density constant through the geometry to obtain uniform statistical errors through the system. However, issues arise from applications to certain geometries. One of them occurs making use of the flux based approach. Application of this method causes the apparition of steep gradients in the WW mesh that create long histories, which take up most of the computing time. In the geometry of a fusion reactor, high density materials and particle streaming through gaps (that lead high weight histories to a low flux region) are typical features of the geometry that create the WW gradients. To avoid long histories, a first approach was taken to create overall smooth weight maps (i.e., from the source to the further regions) by taking the square root of the flux normalization.

In addition, relative error based weight maps do not present long histories, but have the inconvenience of not improving through iterations, creating the necessity of a thorough sampling in the previous run. The second approach taken in this dissertation improves sampling for the relative error weight maps and also addresses long histories for flux based weight maps. In this approach, the density of the materials present in the geometry is reduced in the previous analog run. Weight maps created from this run are thorough and sufficiently smooth to overcome most of the oversplitting issues.

The first application presented in this work has been done to verify the performance of these modifications, using an MCNP analog with implicit capture run (**AWIC**) as a reference, and to compare their efficiency with van Wijk's original algorithms. The geometry used for this case study is ITER's computational benchmark, which features highly absorbent materials as well as gaps reaching from the source to less populated regions in the radial direction. GVR methods compared in this geometry are: van Wijk's flux and error based weight maps (**vanWijk_F** and **vanWijk_Re**), square roots taken over van Wijk's flux based maps (**SQRT_F**), and reducing the materials densities to create flux and relative error based weight maps (**HD_F** and **HD_Re**). All of the GVR techniques showed consistency compared to the **AWIC** run when tallying the same cell in the geometry, thus verifying a reliable performance. In terms of efficiency, all of the GVR methods displayed significant improvement of the FOM and average error compared to the **AWIC** run. Specifically, the **SQRT_F** approach obtained the best FOM, where an improvement of almost two orders of magnitude appears compared to the **AWIC** case. Comparable to the **SQRT_F** technique, results obtained with the **vanWijk_Re** and **HD_Re** methods showed the lowest average errors 1.1% (from 8% with the **AWIC** map) and an

improvement in the FOM of a factor over 60. Lastly for these calculations, the **vanWijk_F** and **HD_F** displayed the worst results in terms of thorough sampling for a given time; due to oversplitting occurring at the highly absorbent materials of the geometry.

A more realistic case was then studied, in which the ITER B-lite neutronics model was used. For this geometry the **vanWijk_F** approach could not be used due to the long histories blocking simulations during the weight map creation. In its place, the cubic root over the flux based map (**CBRT_F**) was introduced to determine its behavior. In opposition to the benchmark problem (in which the **HD_F** approach displayed bad optimization), the **HD_F** method outperformed the rest over the B-lite model. Compared to the **AWIC** simulation in which 79.9% of the voxels were sampled with an average error of 20.1%, the **HD_F** map sampled 99.9% of the voxels with 7.6% average error, and FOM improved by an order of magnitude. **SQRT_F** performed slightly worse than the **HD_F**, but with comparable results. The **vanWijk_Re** weight map also obtained satisfying results, but only in the regions that were sampled in the weight map creation run. Weight maps, being over smoothed, by the **CBRT_F** and **HD_Re** approaches displayed the worst results; however, improvement over the **AWIC** simulation was accomplished in all cases.

The differences in the results obtained from the benchmark problem and the B-lite model, provide a good example of the importance of choosing a variance reduction technique depending on the geometry that will be sampled. For the benchmark system, which features only two materials and is not as large as the B-lite model, the best optimization is obtained for GVR methods in which the WW game created the less number of extra tracks per source particle (i.e., **vanWijk_Re**, **SQRT_F**, and **HD_Re**). However, the smoothness of these weight maps will not take into account sharp differences within a

more complex geometry with a larger number of different materials, such as the B-lite model. In this case, the map with the higher number of extra tracks per source particle (**HD_F**) showed the best results. Nonetheless, even though the **SQRT_F** procedure showed less extra tracks per source particle, it displayed similar results in terms of FOM and only slightly worse in terms of average error (where **HD_F** obtained 7.6% and **SQRT_F** 10.0%). As it was explained in 3.3.3, the **HD_F** approach will not smooth gradients from the source to further regions as much as the **SQRT_F** method does; and the B-lite study provided a good example of the importance of making a compromise between smoothing gradients and taking into account differences for the geometry resolution for sampling large and complex geometries.

Lastly, the two most optimized global weight maps obtained over the B-lite geometry (**SQRT_F** and **HD_F**) were used as an input for a SDR calculation over the equatorial port (in the port interspace). This was done to compare their performance for a response function which results rely on proper neutron flux sampling. The SDR calculations have been made 10^6 s after shutdown and both techniques displayed analogous results; with a difference between them, of only 3.5% in the dose calculated over a given tally.

All the GVR techniques compared in this dissertation showed significant improvement over an MCNP analog with implicit capture simulation. Additionally, oversplitting issues inherent to the system design of a fusion reactor (such as highly absorbent materials and gaps that cause neutron streaming) have been addressed. Weight maps that encompass all the design have been created; providing optimization in the neutron transport and avoiding prohibitive computing times.

As a final note, it is worth mentioning that the optimization of the GVR techniques shown in this work have been applied to the following ITER projects:

- "Design of TBM sets and analyses in view of the ITER-IO Conceptual Design Review", Fusion for Energy, EURATOM, EU. Contract: F4E-OMF-331 Lot 1, Task order No. 1 (2013-ongoing) [59] [60]
- "Shielding study to reduce radiation cross-talk from LP to EP of ITER", Fusion for Energy, EURATOM, EU. Contract: F4E-OPE-0511 (2013-2014) [61]
- FRAMEWORK CONTRACT: Neutronics analysis of ITER diagnostics components. Task Order 32. Reference: ITER/IO/15/TR/11453/JTR (2015-ongoing)
- FRAMEWORK CONTRACT: Neutronics analysis support. Consortium UNED/IDOM. Reference: IO/13/6000000141 (2014-ongoing)

6.2. Future work

Three recommendations for future work are given in this section; regarding improvement of the methodology, applications, and further comparisons.

- All the procedures described in this work are energy independent. Energy dependence approaches are encouraged.
- Applications to different geometries are also suggested; in order to identify issues that may have been overlooked.

- The comparisons of the GVR procedures presented in this work have been made taking van Wijk's original algorithm as a reference point. Comparison of these approaches with other reliable hybrid techniques (such as the FW-CADIS) is recommended to further assess their optimization.

REFERENCES

[1] IEA, "World Energy Outlook," OECD/IEA, Paris, France, 2015.

[2] IEA, "Energy and Climate Change- World Energy Outlook Special Report," OECD/IEA, Paris, France, 2015.

[3] J.K. Shultis, R. E. Faw, *Fundamentals of Nuclear Science and Engineering*. New York, USA: Marcel Dekker, 2002.

[4] S. Glasstone, R. Lovberg, *Controlled Thermonuclear Reactions. An Introduction to Theory and Experiment*. Huntington, New York: Robert E. Publishing Company, 1960.

[5] J.D. Huba, "NRL Plasma Formulary," Naval Research Laboratory, Washington, DC, 2013.

[6] J. D. Lawson, "Some Criteria for a Power Producing Thermonuclear Reacto," *Proceedings of the Physical Society. Section B, 70(1):6*, 1957.

[7] EUROfusion. [Online]. www.euro-fusion.org

[8] E. Rebhan, G. van Oost, "Thermonuclear Burn Criteria," *Fusion Science and Technology*, vol. 45, 2004.

[9] Lawrence Livermore National Laboratory. National Ignition Facility & Photon Science. [Online]. https://lasers.llnl.gov/science/ignition/fast-ignition

[10] P. Ball. (2014) Nature. [Online]. http://dx.doi.org/10.1038/nature.2014.14710

[11] J. C. Glowienka, "Fusion Energy: International Science and Globalized Information," U.S Department of Energy; Office of Science, Presentation 2012.

[12] F. Wagner, "Physics of Magnetic Confinement Fusion," EDP Sciences, EPJ Web Conferences DOI: 10.1051/epjconf/20135401007, 2013.

[13] ITER. [Online]. https://www.iter.org/

[14] Princeton Plasma Physics Laboratory. [Online]. http://www.pppl.gov/

[15] A. Edward Profio, *Radiation Shielding and Dosimetry*. New York: John Wiley & Sons, Inc, 1979.

[16] G.I. Bell, S. Glasstone, *Nuclear Reactor Theory*. New York: Van Nostrand and Reinhold, 1970.

[17] E.E. Lewis, W.F. Miller, *Computational Methods of Neutron Transport*. New York: John Wiley & Sons, 1984.

[18] Team, X-5 Monte Carlo, "MCNP- A General Monte Carlo N-Particle Transport Code, Version 5. Volume I: Overview and Thoery," Los Alamos National Laboratory, LA-UR-03-1987 April 2003.

[19] I. Lux, L. Koblinger, *Monte Carlo Particle Transport Methods: Neutron and Photon Calculations*. Boca Raton, FL: CRC Press, 1990.

[20] A. Haghighat, J.C. Wagner, "Monte Carlo Variance Reduction with Deterministic Importance Functions," *Progress in Nuclear Energy*, vol. 42, no. 1, 2003.

[21] Booth, T.E., "Common misconceptions in Monte Carlo particle transport," *Applied Radiation and Isotopes*, no. 70, 2012.

[22] Wu, Y., "CAD-based Interface Programs for Fusion Neutron Transport Simulation FDS Team," *Fusion Engineering and Design*, vol. 84, 2009.

[23] T. Booth, J. Hendricks, "Importance Estimation in Forward Monte Carlo Calculations," *Nuclear Technology/fusion*, vol. 5, no. 1, 1984.

[24] How, J., "Plant Description," ITER IO, Report ITER_D_2X6K67_v1.1, October 2009.

[25] L. Petrizzi, H. Iida, D. Valenza, P. Batistoni, "Improvement and benchmarking of the new shut-down dose estimation method by Monte Carlo code," in *Proceedings of the MC 2000 conference; Lisboa, October 23-26, 2000, Springer, Berlin (2001)* , pp. 865–870.

[26] M.A. Cooper, E.W. Larsen, "Automated Weight Windows for Global Monte Carlo Particle Transport Calculations," *Nuclear Science and Engineer*, no. 137, 2001.

[27] J.C. Wagner, A. Haghighat, "Automated Variance Reduction Of Monte Carlo Shielding Calculations Using the Discrete Ordinates Adjoint Function," *Nuclear Science and Engineering*, no. 128, 1998.

[28] A. Haghighat, H. Hiruta, B. Petrovic, J.C. Wagner, "Performance of the Automated

Adjoint Accelerated MCNP (A3MCNP) for simulation of a BWR core shroud problem," in *Proceeding of International Conference on Mathematics and Computation in Reactor Physics,and Environmental Analysis in Nuclear Applications*, Madrid, Spain, 1999.

[29] S. Mosher, T. Miller, T. Evans, J.C. Wagner, "Automated weight-window generation for threat detection applications using ADVANTG," in *Proceeding of the 2009 Internationals Conference on Advances in Mathematics, Computational Methods, and Reactor Physics,* Saratoga Springs, NY, 2009.

[30] D. Peplow, S. Bowman, E. Horwedel, J.C. Wagner, "Monaco/MAVRIC: Computational Resources for Radiation Protection and Shielding in SCALE," *Transaction American Nuclear Society*, no. 95, 2006.

[31] J.C. Wagner, E.D. Blakeman, D.E. Peplow, "Forward-Weighted CADIS Method for Global Variance Reduction," *Transactions of the American Nuclear Society*, no. 97, 2007.

[32] J.C. Wagner, E.D. Blakeman, D.E. Peplow, "Forward-Weighted CADIS Method for Variance Reduction of Monte Carlo Calculations of Distributions and Multiple Localized Quantities," *International Conference on Mathematics, Computational Methods & Reactor Physics (M&C 2009),* American Nuclear Society, 2009.

[33] J.C. Wagner, D.E. Peplow, S.W. Mosher, "FW-CADIS Method for Global and Regional Variance Reduction of Monte Carlo Radiation Transport Calculations,"

Nuclear Science and Engineering, vol. 176, 2014.

[34] J.C. Wagner, D.E. Peplow, W. Mosher, T.E. Evans, "Review of Hybrid (Deterministic/Monte Carlo) Radiation Transport Methods, Codes, and Applications at Oak Ridge National Laboratory," *Progress in Nuclear Science and Technology*, vol. 2, 2011.

[35] Peplow, D.E., "Comparison of Hybrid Methods for Global Variance Reduction in Shielding Calculations," in *International Conference on Mathematics and Computational Methods Applied to Nuclear Science & Engineering (M&C 2013)*, Sun Valley, Idaho, 2013.

[36] A. M. Ibrahim, M. E. Sawan, S. W. Mosher, T. M. Evans, D. E. Peplow, P. P. Wilson, J. C. Wagner, "Global Evaluation of Prompt Dose Rates in ITER Using Hybrid Monte Carlo/Deterministic Technique," *Fusion Science and Technology*, vol. 60, August 2011.

[37] R. Pampin, A. Davis, J. Izquierdo, D. Leichtle, M.J. Loughlin, J. Sanz, A. Turner, R. Villari, P.P.H. Wilson, "Developments and needs in nuclear analysis of fusion technology," *Fusion Engineering and Design*, vol. 88, 2013.

[38] A.M. Ibrahim, P.P. Wilson, M.E. Sawan, S.W. Mosher, D.E. Peplow, R.E. Grove, "Assessment of Fusion Facility Dose Rate Map Using Mesh Adaptivity Enhancements of Hybrid Monte Carlo/Deterministic Techniques," *Fusion Engineering and Design*, vol. 89, 2014.

[39] T.L. Becker, E.W. Larsen, "The Application of Weight Windows to “Global” Monte Carlo Problems," in *International Conference on Mathematics, Computational Methods & Reactor Physics (M&C 2009)*, Saratoga Springs, NY, 2009.

[40] A. M. Ibrahim, D.E. Peplow, R. E. Grove, "Novel Hybrid Monte Carlo/Deterministic Technique for Shutdown Dose Rate Calculations," in *Transactions of the American Nuclear Society*, Atlanta, Georgia, 2013.

[41] A. M. Ibrahim, D. E. Peplow, J. L. Peterson, R. E. Grove, "Analysis of Shutdown Dose Rate in Fusion Energy Systems Using Hybrid Monte Carlo/Deterministic Techniques," in *18th Topical Meeting of the Radiation Protection & Shielding Division of ANS*, Knoxville, TN, 2014.

[42] A. Davis, A.Turner, "Comparison of Global Variance Reduction methods for Monte Carlo Radiation Transport Simulations of ITER," *Fusion Engineering and Design*, vol. 86, 2011.

[43] A. Davis, A. Turner, "Applications of Novel Global Variance Reduction Methods to Fusion Radiation Transport Problems," in *International Conference on Mathematics and Computational Methods Applied to Nuclear Science and Engineering (M&C 2011)*, Rio de Janeiro, 2011.

[44] A. Turner, A. Davis, "Improving Computational Efficiency of Monte-Carlo Simulations with Variance Reduction," in *International Conference on Mathematics and Computational Methods Applied to Nuclear Science & Engineering (M&C 2013)*,

Sun Valley, Idaho, 2013.

[45] M.J. Loughlin et al., "ITER Nuclear Analysis Strategy and Requirements," *Fusion Science and Technology*, vol. 56, 2009.

[46] A. Turner, D. Leichtle, P. Lamalle, B. Levesy, L. Meunier, E. Polunovskiy, R. Sartori, M. Shannon, "Shielding Optimisation of the ITER ICH&CD Antenna for Shutdown Dose Rate," *Fusion Engineering and Design*, vol. in press, 2015.

[47] Z. Ghani, A. Turner, S. Mangham, J. Naish, M. Lis, L. Packer, M. Loughlin, "Radiation Levels in the ITER Tokamak Complex During and After Plasma Operation," *Fusion Engineering and Design*, vol. in press, 2015.

[48] A.J. van Wijk, G. Van den Eynde, J.E. Hoogenboom, "An Easy to implement Global Variance Reduction procedure for MCNP," *Annals of Nuclear Energy*, vol. 38, 2011.

[49] www.python.org.

[50] X-5 Monte Carlo Team, "MCNP - A General Monte Carlo N-Particle Transport Code Version 5," Los Alamos National Laboratory, LA-CP-03-0245, 2005.

[51] D. Lopez Al-dama, A. Trokv, "FENDL-2.1: Update of an Evaluated Nuclear Data Library for Fusion Applications," IAEA, Vienna, INDC (NDS)-46, 2004.

[52] http://www.paraview.org.

[53] B-lite v3 R121217 (ITER_D_9KKVQR).

[54] P. Sauvan, J.P. Catalan, F. Ogando, R. Juarez, J. Sanz, "Development of the R2SUNED Code System for Shutdown Dose Rate Calculations," *IEEE TRANSACTIONS ON NUCLEAR SCIENCE*, vol. 63, no. 1, February 2016.

[55] J. Sanz, O. Cabellos, N. Garcia-Herranz, "ACAB Inventory Code for Nuclear Applications," UNED, Madrid, Users Manual NEA-1839, December 2008.

[56] M. Loughlin, N. Taylor, "Recommendation on Plasma scenarios," (ITER_D_2V3V8G),.

[57] "Recommendations on Computation of Dose from Flux Estimates ," (ITER_D_29PJCT v1.0),.

[58] R.A. Forrest, "EAF 2007 neutron-induced cross section library," UKAEA FUS 535, March 2007.

[59] "Design of TBM sets and analyses in view of the ITER-IO Conceptual Design Review," F4E-OMF-331 Lot1 - TO #01,.

[60] R. Juarez, P. Sauvan, L. Perez, D. Panayotov, J. Vallory, M. Zmitko, Y. Poitevin, J. Sanz, "Shutdown Dose Rate analysis of the European Test Blanket Modules shields in ITER Equatorial Port #16," *Fusion Engineering and Design*, no. doi:10.1016/j.fusengdes.2015.11.023, 2015.

[61] "Shielding proposal to reduce the neutron cross-talk between EP and LP of ITER," F4E-OPE-511,.